A Lagrangian, Discontinuous-Galerkin Material Response Solver for the Analysis of Ablative Thermal Protection Systems

by

Christopher Quinn

B.S., Texas A&M University, 2017

Submitted to the Center for Computational Science and Engineering
in partial fulfillment of the requirements for the degree of

MASTER OF SCIENCE

at the

MASSACHUSETTS INSTITUTE OF TECHNOLOGY

September 2023

Authored by:	Christopher Quinn Center for Computational Science and Engineering May 17, 2023
Certified by:	Raúl Radovitzky Professor of Aeronautics and Astronautics, Thesis Supervisor
Accepted by:	Youssef Marzouk and Nicolas Hadjiconstantinou Co-Directors, Center for Computational Science and Engineering

A Lagrangian, Discontinuous-Galerkin Material Response Solver for the Analysis of Ablative Thermal Protection Systems

by

Christopher Quinn

Submitted to the Center for Computational Science and Engineering
on May 17, 2023 in partial fulfillment of the requirements for the degree of

MASTER OF SCIENCE

ABSTRACT

Thermal protection systems (TPS) play a vital role in safeguarding aerospace vehicles from the intense aerodynamic heating encountered during hypersonic flight. One category of TPS materials manages extreme heat through pyrolysis, a process in which the elevated temperatures trigger an endothermic reaction that decomposes the material into char and gases, and through thermochemical ablation, in which char and pyrolysis gases blow away from the surface. Their use is common in high-velocity hypersonic missions through dense atmospheres, in contrast to other materials such as reusable TPS, which are often used in lower heat flux scenarios. Analysis of ablative TPS materials is challenging due to their complex material response which involves a combination of thermal, chemical, and mechanical phenomena.

A major concern in hypersonic vehicle design is the catastrophic failure of the TPS. It is necessary to anticipate scenarios in which excessive ablation, inelastic deformation, or fracturing of the TPS occurs. A successful TPS design should account for these failure modes while balancing concerns about cost, weight, and vehicle performance.

Computational modeling has emerged as an important tool in TPS design, and in predicting the behavior of TPS materials including failure. Existing codes are capable of modeling the thermo-chemical response of ablative TPS and predicting some modes of failure, but they are often limited in their ability to model mechanical deformation and damage.

This thesis proposes a new computational framework for modeling the thermo-chemo-mechanical behavior of ablative TPS materials to address this gap. The modeling approach is based on a Lagrangian, Discontinuous-Galerkin finite element formulation of the coupled multiphysics problem, which includes models of finite elastic and inelastic deformation as well as damage, pyrolysis reactions, heat, and mass transfer. The numerical solution employs a semi-implicit time integration scheme for the nonlinear heat and mass transfer problems, while the solid mechanics is addressed using dynamic relaxation. Importantly, a mesh recession algorithm is implemented to explicitly account for changes in geometry due to material ablation. A staggered iteration scheme is used to couple the multiphysics problem.

Several numerical examples demonstrating the correctness and versatility of the proposed method are presented. These include verification against several analytical solutions to the heat equation and benchmark problems utilized in the ablation modeling community. The mesh recession algorithm is also verified through a series of numerical tests known as patch tests. Finally, a demonstration of an arc-jet experiment of phenolic-impregnated carbon

ablator (PICA) is presented to illustrate the computational framework's ability to model thermo-chemically induced deformation, stresses, and surface recession in pyrolyzing TPS materials.

Thesis supervisor: Raúl Radovitzky
Title: Professor of Aeronautics and Astronautics

Acknowledgments

First and foremost, I would like to extend my deepest gratitude to my advisor, Professor Raúl Radovitzky, for the opportunity to perform research under his guidance. His unwavering support has been invaluable in my development as a researcher. Raúl, thank you for believing in my potential, helping me thrive in this challenging environment, and for inspiring me to set and achieve ambitious life and research goals.

This work would not have been possible without the financial and technical support of Lincoln Laboratory. In particular, I would like to thank Nathan Falkiewicz for the opportunity to collaborate with him, and have technical discussions about ablative thermal protection systems.

Next, I would also like to thank the past and current members of the Radovitzky Research Group including Professor Bianca Giovanardi, Daniel Pickard, Giulia Pozzi, Michelle Xu, Zhiyi Wang, Theo Rulko, Aaditya Rau, and Zahra Soltani. Collectively and individually, they have contributed to a collaborative and enjoyable environment. I want to express particular appreciation to Aaditya Rau and Theo Rulko for many insightful suggestions for this thesis, as well as their enduring friendship. Equally, I would like to acknowledge Daniel Pickard for the numerous helpful discussions we've had, our effective teamwork on various projects, and his valued friendship.

I would also like to express my gratitude towards fellow CSE graduate students, including Sebastian Gallo, Erkin Verbeek, Corwin Stites, Manideep, and numerous others, for their enduring friendship and unwavering support. Their presence has been invaluable, and I am fortunate to have discovered a strong sense of community within the Center for Computation Science and Engineering at MIT. Furthermore, I extend my appreciation to fellow MIT students, such as Michael Espinal, Spencer Taylor, Zain Karsen, Kyle Jiang, and several more, for their friendship and support.

Finally, heartfelt thanks go to my brother, Alex, and my exceptional parents. Their encouragement, steadfast support, and unconditional love have been vital throughout. I remain deeply indebted to them; without their presence, this journey would not have been possible, and for that, I am eternally grateful.

Contents

List of Figures

List of Tables

Chapter 1

Introduction

Aerospace vehicles in hypersonic regimes, characterized by Mach numbers greater than 5, face significant challenges. Examples of hypersonic flight include planetary entry and high-speed, high-density atmospheric flight. Such flight is characterized by extreme aerothermodynamic conditions, including high temperatures, pressures, and shear stresses. Given the extreme nature of this environment, a thermal protection system (TPS) is required to protect the vehicle's structure and payload. Careful design and development of a TPS extends from material selection up to trajectory planning and mission design. Fundamentally, it must balance competing concerns of lightweight design, cost, effective thermal protection, structural integrity, and longevity. The necessity for informed TPS design has motivated extensive research into their performance under extreme conditions.

Thermal protection systems can be classified based on the method of protection, including passive, semi-passive, and active [1]. Passive methods involve stationary components such as heat sinks, hot structures, or insulated surfaces. Semi-passive methods utilize heat pipes and ablative surfaces. Finally, active methods include convective cooling, film cooling, and transpiration cooling. TPS can also be categorized by their reusability; semi-passive ablative TPS are not reusable, whereas other TPS are typically reusable. The choice of TPS depends on the mission requirements and the specific physical environments encountered.

The aerothermal environment surrounding a TPS may be envisioned as made up of distinct regions including a boundary layer, an inviscid flow region, and a wake region [2] (see Figure 1.1). These regions involve complex interactions between viscous and inviscid flows, separated flows, and chemical reactions, intertwined with other intricate physical and chemical processes [3]. In the boundary layer, the TPS material is exposed to intense heat fluxes arising from aerodynamic heating, coupled with pressure and shear distributions stemming from the aerodynamic forces and moments within the flow field. Concurrently, interactions of the TPS material with the surrounding gas instigate surface chemical reactions. As the material transfers heat from the surface to the interior, several physical and chemical processes may occur in the bulk material. These include thermal energy transport, bulk chemical reactions, solid-to-gas phase changes, chemical species transport, and mechanical deformation. Beyond this, these processes may change the material properties of the TPS including its mass density, mechanical strength and stiffness, thermal conductivity, heat capacity, chemical reactivity, permeability, and/or chemical species diffusivity. These processes also depend

on the composition and state of the atmosphere, the trajectory and velocity of the vehicle, and the shape of the vehicle which may change over the course of its mission.

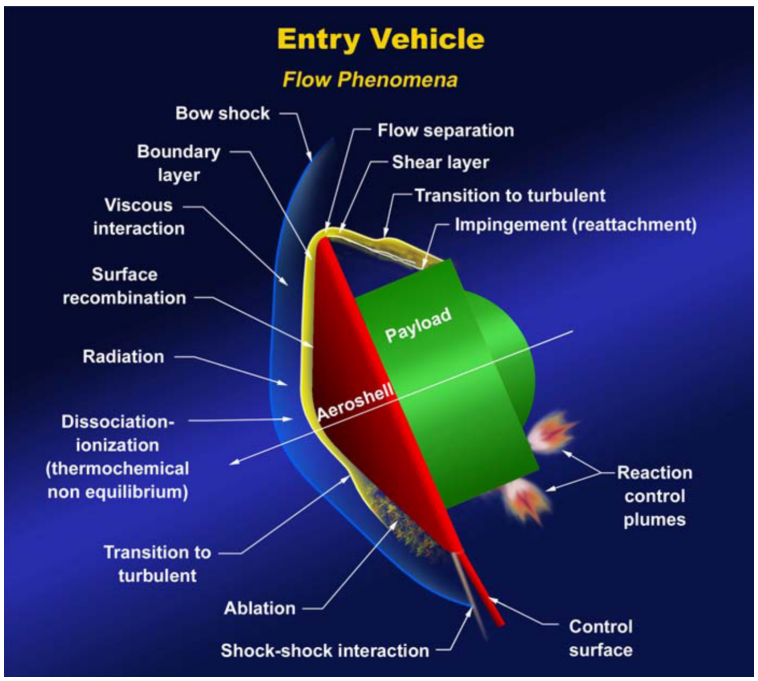

Figure 1.1: Schematic of the aerothermal environment around a typical aerospace vehicle during re-entry. Taken from [4].

The complex and coupled phenomena in the TPS material environment may ultimately lead to catastrophic failure of the TPS. Thermal expansion effects, high pressures, and shear forces may cause the TPS to fracture, spall, or otherwise deform. The TPS may also fail due to excessive ablation by chemical means, phase changes, or mechanical erosion. In general, TPS that undergo ablation can be classified as in-depth ablators or surface ablators [5]. Surface ablators, which exhibit mass loss exclusively at the surface, are usually governed by mechanisms such as sublimation, melting, oxidation, or surface chemical erosion [5]. Notable examples of surface ablators include graphite, camphor, and carbon-carbon materials. In contrast, in-depth ablators experience mass loss throughout the material due to chemical processes such as oxidization, pyrolysis, or other thermochemical degradation mechanisms. Examples of in-depth ablators include carbon/phenolic ablators, cork-based ablators, and other carbon-based ablators [5].

The design and analysis of TPS materials is a complex endeavor that requires a multi-disciplinary approach. An accurate representation of the physics and chemistry of the flow environment is required to accurately model material response. This has motivated extensive research into TPS materials and their performance under extreme conditions, going back to the 1950s.

1.1 History of Thermal Protection Systems

The origin of thermal protection systems can be traced back to the development of ballistic systems during World War II [1], followed by defense programs in the United States, USSR, and Europe [5]. Some early examples of thermal protection systems include the Inconel X hot structure passive TPS used on the X-15 research plane, which was capable of withstanding temperatures up to approximately 900 K [1]. During this period, H. Julian Allen and A. J. Eggers Jr. introduced a significant design concept for effective heat shield performance in their 1958 publication, in which they demonstrated that the heat load experienced during reentry is inversely proportional to the drag coefficient, which can be reduced by increasing the vehicle's surface area [6]. The use of a blunt shape for the vehicle helps redirect the shock wave away from the surface, effectively shielding it from most of the hot gases. This blunt body concept was used in the GE Mk I re-entry vehicle and later in the MK II warhead, which also employed a metallic heat sink as a passive thermal protection system [1]. Soon, however, new ablative thermal protection systems were researched by the U.S. Army that allowed for the development of longer-range ballistic missiles.

By the late 1950s and early 1960s, thermal protection systems became essential components of aerospace vehicles engaged in human spaceflight and exploration, ensuring the safe return of astronauts and spacecraft during reentry to Earth. An important program designed to accelerate human space exploration was Project Mercury, which aimed to explore human capabilities in space, launch humans into orbit around the Earth, and ensure the safe retrieval of astronauts and spacecraft. Project Mercury implemented a series of flights to systematically evaluate capabilities and technologies in preparation for future missions. Extensive design and development efforts were undertaken to create a reliable and effective thermal protection system for the Mercury spacecraft, with the first design using a combination of a beryllium heat sink and a blunt shape [7]. Despite concerns about its toxicity and weight, the beryllium heat shield was utilized in the Freedom 7 capsule during the Mercury-Redstone 3 mission by Alan B. Shepard on May 5, 1961, and in the Liberty Bell 7 capsule during the Mercury-Redstone 4 mission by Virgil I. Grissom on July 21, 1961 [7]. These particular missions were suborbital flights in which a Redstone Launch vehicle, a descendant of the German V-2, would carry the spacecraft into space and then separate. The capsule would then reenter the atmosphere and land in the ocean, where it would be retrieved by a ship. Although the heat shield successfully protected the spacecraft during reentry, it was deemed unsuitable for future use [7].

To address the limitations of the original heat shield design, a new ablative heat shield was developed for the Mercury Capsule which was inspired by a Jupiter missile nose cone [7]. In order to assess the thermal performance of the new ablative heat shield concept for human spaceflight trajectories, a test flight named Big Joe 1 was launched on September 9, 1959. This flight involved instrumentation on the heat shield to gather temperature and char penetration history data [7]. Although there were some malfunctions which prevented the planned trajectory from being achieved, the flight was successful in demonstrating the feasibility of the new ablative heat shield concept. With the success of the Big Joe 1 flight, the ablative heat shield was used in the Mercury-Atlas 2 suborbital flight, the Mercury-Atlas 4 orbital flight, the Mercury-Atlas 5 orbital flight of Enos the Chimp, and the Mercury-Atlas

6 orbital flight of John H. Glenn Jr. on February 20, 1962 [7]. Project Mercury ended with the flight of astronaut Gordon Cooper in the Mercury-Atlas 9 orbital flight on May 15, 1963 [1].

Following the success of the ablative thermal protection system in Project Mercury, ablative heat shields were subsequently utilized in many NASA missions, including Project Gemini, Project Apollo, and the Viking Lander program to Mars. The Apollo missions used AVCOAT 5026, an epoxy novolac resin with special additives embedded in a fiber-glass honeycomb matrix [8]. It is worth noting that this material is still utilized in present-day missions, including the Orion spacecraft [9].

Super lightweight ablator (SLA) is another TPS material which proved to be an excellent choice for use in the Martian environment. SLA-561V, for example, is a highly-filled, lightweight elastomeric silicone ablator developed by Martin Marietta [10] able to endure moderate levels of heat and pressure. As a result, it was employed in the Aeroshell heat shield for the Viking Lander program to Mars and in the Mars Pathfinder mission [5]. In order to explore the atmospheres of Venus and Jupiter, which presented extreme conditions, the Pioneer mission to Venus and the Galileo mission to Jupiter required the development of advanced ablative materials [11, 12]. Tape-wrapped carbon phenolic (TWCP) carbon resin TPS material was employed in the heat shields for both missions [5]. This material is more dense than normal ablative materials, but is is able to withstand enormous heating and pressure conditions.

The desire to have samples of material returned to Earth from the surface of moons and planets led to the realization that a new type of ablative material was needed that was lightweight, ablative, and insulative. This led to the development of Phenolic Impregnated Carbon Ablator (PICA) [13]. PICA has found application in various recent space missions. For instance, it was utilized in the Stardust sample return mission, which aimed to collect dust and gases from the comet Wild-2 [14]. Additionally, PICA was employed in the Mars Science Laboratory mission, which focused on detailed exploration of the Martian landscape and atmosphere [15–17]. Furthermore, it was chosen for the SpaceX Dragon Capsule, designed for transporting cargo between Earth and space [18]. PICA uses a preformed fibrous carbon substrate, which is then infiltrated with phenolic resin [13]. It is known to undergo pyrolysis, which is a thermo-chemical decomposition process that occurs in-depth within the material while heating that converts solid material into gaseous products and leaves behind a layer of char.

1.2 Material Response of Low-Density, Ablative Thermal Protection Systems

Low-density ablators that pyrolyze are commonly used in space missions where the heat flux is high enough to cause significant material ablation. These materials are attractive for use in thermal protection systems because they are lightweight, produce pyrolysis gas products from decomposition of the resin which consume and advect away thermal energy,

and help cool the surface of the vehicle through the ejection of blowing gases which thickens the boundary layer and reduces the heat flux to the surface [5]. Furthermore, the carbon fibers that form the matrix of the material resist thermal and chemical degradation.

Decomposing or charring ablators are typically composed of a resin matrix and a fiber reinforcement. When subjected to high temperatures, the material undergoes thermal decomposition in the absence of oxygen in a process known as pyrolysis. As a result of pyrolysis, several different chemical species are formed from the reactants in the solid, including gas products and a layer of char. The produced gases are then free to move through the porous material and eventually make their way to the surface of the pyrolyzing body and exit to exchange mass and energy with the boundary layer gases. As the reactions progress, the char layer thickens and a decomposition zone forms between the char layer and virgin material deeper in the body of the material. While the char layer grows, the virgin material is consumed and the total thickness of the material decreases as the surface recedes due to ablation of the char layer. Figure 1.2 shows a schematic of a low-density ablative thermal protection system undergoing pyrolysis in which the char layer, decomposition zone, and virgin material are shown. The direction of flow of the pyrolysis gas products towards the ablating surface is indicated by arrows.

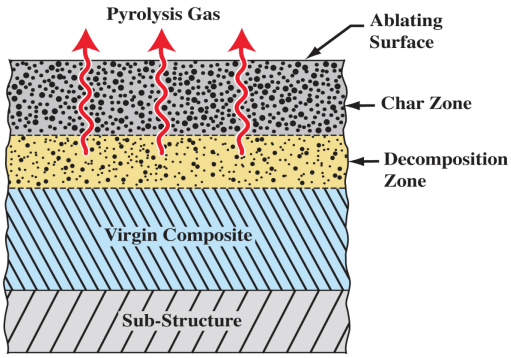

Figure 1.2: Schematic of a low-density, pyrolyzing ablative thermal protection system. Taken from [19].

The reaction mechanisms of pyrolysis are described in great detail in the literature [20–23]. Recent research on lightweight ablative composites has focused primarily on characterizing the pyrolysis [24–27], the thermal response [18, 28], and the porous media transport properties [29–36].

For accurate modeling of material response, it is important to properly characterize not only the thermal, chemical, and transport properties of thermal protection materials, but also their mechanical behavior. Experimental evidence demonstrates that materials exposed to conditions resembling atmospheric reentry can undergo significant and irreversible deformations.

The char exhibits lower strength and stiffness compared to the original material and undergoes additional carbon sublimation, oxidation, or nitridation reactions, which can result in fiber damage. Fig. 1.3 displays a PICA char fiber with evident pits formed on its surface due to chemical attack. Chemical degradation can lead to fiber failure and mechanical erosion

of the char layer, a phenomenon referred to as spallation. Eventually, the char layer's surface recedes as a result of the combined effects of these processes.

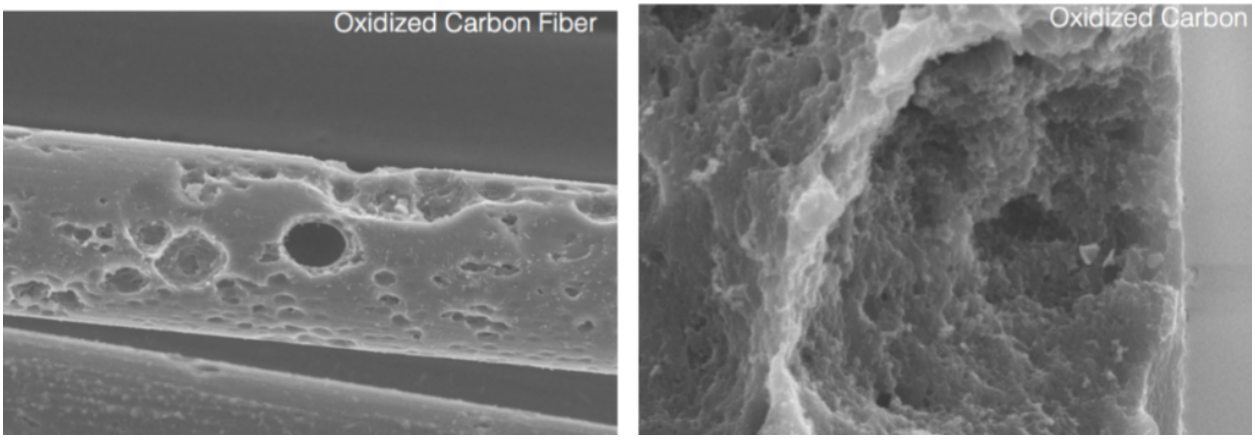

Figure 1.3: Oxidation-induced pitting in PICA fibers [37]

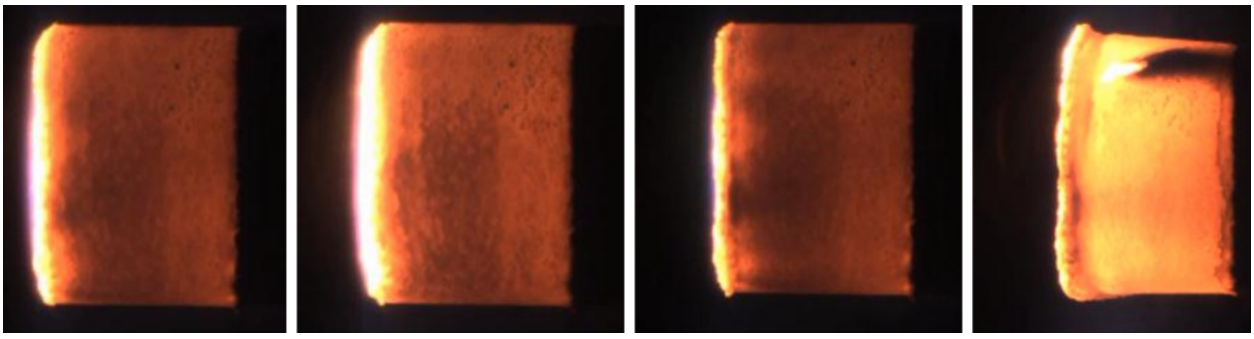

Figure 1.4: Deformation of PICA during arc jet heating [38] as viewed from the side. Images taken at 10, 17, 30 and 59 seconds.

In the case of phenolic impregnated carbon ablator (PICA), macroscopic deformations have been observed in arc jet heating experiments conducted by Butler et al. [38]. These experiments involve exposing cylindrical PICA specimens to a high enthalpy gas jet from one side, resulting in extreme heating, thermo-chemical decomposition, and deformation along the cylindrical face. The observed deformations arise from thermal expansion, mechanical stresses, and thermal softening.

PICA tiles are commonly bonded together and attached to flight vehicles using room temperature vulcanized rubber (RTV), which also exhibits inelastic deformation under heating conditions. For example, when PICA tiles are exposed to a shearing arc jet flow, the rubber initially filling the gaps between the tiles flows to the right due to the intense heating and applied shear stress. The different mechanical and thermophysical properties of the rubber in the gaps and the tiles can lead to nonuniform recession rates, which can impact the external flow and overall heat shield performance.

Low-density thermal protection system (TPS) materials display various mechanical response characteristics, including anisotropic yielding and elastic behavior influenced by fiber

orientation, thermal softening [39], and elastoplasticity with compaction-like behavior at large compressive strains, as commonly observed in highly porous materials [40, 41]. Additionally, the fracture of ablative TPS materials may contribute to the pyrolysis process by providing a pathway for hot gases to penetrate deeper into the material, thereby accelerating pyrolysis around the fracture site [9]. Agrawal et al. [42] have conducted some characterization of the fracture behavior of the fiber form, which serves as the precursor to PICA.

1.3 Previous Modeling of Ablative Thermal Protection Systems

Several modeling approaches have been developed to simulate the complex behavior of ablative thermal protection systems. Typically, these methods require solving a set of partial differential equations encompassing energy, mass, and momentum balance. Specifically, the energy equation is solved for the temperature distribution in the material, considering the effects of heat conduction and advection of thermal energy through gas transport within the material. Often, a material degradation model based on empirical data is employed to describe the phenomenon of solid mass loss at different depths. Additionally, the mass and momentum conservation equations are employed to model the movement of gas within the porous material by solving for the mass flux of the gas within the material. An empirical model such as Darcy's law [43] or a Darcy-Forchheimer [44] relationship is used to model the volume-averaged momentum balance in the continuous regime [5]. Some models, however, approach the gas transport model using additional simplifications, including zero permeation time with a finite mass flow rate [5]. To complete the equations, a series of boundary conditions are necessary, commonly derived from a surface energy or mass balance equation. These models often rely on numerous simplifying assumptions including local thermal equilibrium between the gas and solid phases, negligible kinetic energy in the momentum equation, well-mixed gas composition with an average molar mass, one-dimensional heat and mass transfer, and other related assumptions.

The seminal work by Moyer and Rindal [45] introduced a form of the energy balance equation that remains widely used today. In their formulation, they present a one-dimensional form of the energy equation

$$\rho c_p \frac{\partial \theta}{\partial t} = \frac{\partial}{\partial x_s}\left(\kappa \frac{\partial \theta}{\partial x_s}\right) + \left(h_g - \bar{h}\right)\frac{\partial \rho}{\partial t} + \dot{s}\rho c_p \frac{\partial \theta}{\partial x_s} + \dot{m}_g \frac{\partial h_g}{\partial x_s} \tag{1.1}$$

where θ is the temperature, t is time, x_s is the spatial coordinate in the solid, κ is the thermal conductivity, $\bar{h}$ is a quantity known as the partial heat of charring, $\dot{s}$ is a grid convection velocity needed to correct for the moving grid due to ablation, ρ is the density, c_p is the specific heat capacity, $\dot{m}_g$ is the mass flux of the gas, and h_g is the enthalpy of the gas. This equation uses Fourier's law of heat conduction to model heat conduction within the solid, and includes an advection term to account for heat transfer due to the movement of gas

within the porous material. Also, it includes a grid convection term since the domain is in a moving coordinate system anchored to the receding surface. In order to obtain the mass flux of the gas, a simplified gas transport model is used where zero permeation time is assumed despite a finite gas flow mass rate calculated by

$$\dot{m}_g = \int_{\infty}^{x} \frac{\partial \rho}{\partial t}\, dy \tag{1.2}$$

where y is the spatial coordinate in the gas. This model was implemented in the Charring Material Ablation (CMA) code developed by the Aerotherm Corporation [46]. It solves the internal energy balance using a one-dimensional finite difference numerical scheme. CMA incorporates surface recession due to ablation by dropping nodes at the back face when the nodes become too small, while the remaining nodes are moved by the same velocity based on the surface recession rate. The pyrolysis kinetics are computed using a three-component decomposition model by Goldstein [47], which will be described in more detail in a future section. In order to more accurately compute the solid phase continuity, CMA uses a sub-mesh scheme where the grid for the energy conservation is further subdivided within each cell. This allows the energy conservation equation to be solved more quickly on the coarse mesh, while the decomposition model is solved on the subnodes within each cell since it displays sharp gradients making it more sensitive to the spatial discretization. Despite the limitations of the model, CMA has found extensive use in the industry for ablation modeling, analysis, and design purposes, especially for sizing TPS materials in diverse mission trajectories.

The original model implemented in CMA has been modified and extended in other codes such as the Fully Implicit Ablation and Thermal Analysis (FIAT) code by NASA [48]. FIAT utilizes a finite volume numerical scheme and offers greater numerical stability compared to CMA. Additionally, it incorporates an interface with external fluid flow solvers for surface interactions [48]. In order to model material recession due to ablation, FIAT incorporates a coordinate system that moves with the surface [48]. FIAT also includes the simple decomposition model by Goldstein [47] used in CMA [46]. Since its development, FIAT has emerged as a contemporary alternative to CMA for ablation modeling.

Subsequently, FIAT was expanded to enable analysis in two dimensions [49], then three dimensions [50] and renamed TITAN. These enhancements have allowed for the assessment of multidimensional effects in more complex geometries and have facilitated the coupling of thermal and structural responses with non-TPS structures.

Another numerical approach to modeling ablation problems with a moving grid, called the control volume finite element method (CVFEM), was developed by Blackwell [51]. In this approach, exponential differencing was used to improve accuracy. To overcome the complication of dropping nodes, the CVFEM was subsequently modified to use a grid with a fixed number of cells and moving nodes [52]. This approach was later extended to three dimensions where the mesh deformation is determined by solving a 3D elasticity problem [53].

In an effort to more accurately model ablation, Lachaud introduced a model in the Porous material Analysis Toolbox based on OpenFOAM (PATO) that accounts for all of the phenomena included in CMA, incorporates a momentum balance equations for the evolved gases, and tracks mass and energy conservation for individual species or elements, along with finite-rate or equilibrium chemistry [18]. Additionally, Lachaud devised a classification system for existing ablative material response codes based on the level of modeling complexity [54]. The

classification system organizes codes into three types: Type I which includes heat transfer, pyrolysis, a simplified transport model of the produced gases, equilibrium chemistry, and surface ablation; Type II which includes momentum conservation for a well-mixed gas species; and Type III which incorporates individual component conservation equations, finite-rate chemistry models, and more detailed physical and chemical modeling. FIAT and CMA fall under the Type I model classification. Some examples of Type II solvers include the ITRAC code [55], the finite-element-based ablative and thermal response simulator (FEATS) [56], and ICARUS [57]. PATO is an example of a Type III solver [58]. Another Type III solver is the Coupled Hypersonic Protection System (CHyPS) solver, which utilizes a high-order discontinuous Galerkin formulation for mass, energy, and momentum in both solid and gas phases, employing an Arbitrary Lagrangian Eulerian approach [59].

Commercial general-purpose finite element codes have also been employed to model ablation. Wang et al. [60] utilized a 1D ABAQUS model, which was then verified against FIAT. To overcome limitations in ABAQUS, custom user-specified routines were developed for the decomposition model and surface energy balance. The verified model was then validated against experimental data. The model only achieved partial success in accurately representing the experimental results, potentially due to its reliance on fictitious material properties known as Theoretical Ablative Composite for Open Testing (TACOT) [61], or the simplifying assumption of a 1D analysis. A similar approach was pursued using COMSOL in [62].

A verification procedure for one-dimensional material response codes was outlined by Amar [19] due to the complexity of the different models and the lack of unified verification studies. This strategy has been adopted for various codes and has been expanded to include more comprehensive 3D codes like ITRAC [55], CHAR [63], and ICARUS [57]. Furthermore, in recent years, researchers have conducted code-to-code comparisons using the fictitious TACOT material [61] and test cases from the Kentucky Ablation Workshop [64–66] to evaluate various aspects of material response codes.

The success of these modeling approaches relies on the validation achieved through well-characterized thermo-physical and mechanical material properties. These properties are obtained through carefully designed and executed experiments that accurately depict the behavior of TPS materials under the conditions encountered during flight trajectories. Milos and Chen [67] performed a validation study of TITAN using arc jet experiments. Furthermore, modeling can be utilized to address uncertainties inherent in experimental data. A recent study utilized early-time thermal response data from the same arc jet experiments to develop a dimensionless parameter group model for material response, specifically focusing on characterizing the thermal conductivity of PICA [68, 69].

Overall, the primary focus in the field has predominantly been on modeling thermochemical ablation, with relatively less emphasis on capturing the stress-strain behavior of materials. A notable exception is the Kentucky Aerothermodynamics and Thermal-response System (KATS) code, which utilizes a finite volume framework and integrates linear thermoelasticity within an Eulerian framework [70–72]. Additionally, KATS incorporates a mesh recession routine to account for ablation processes [73, 74]. This code has been extended to describe material failure using a continuum damage model [73]. Another material response code that incorporates mesh recession [75] and linear thermoelasticity [63] is the CHarring Ablator Response (CHAR) developed by NASA, which uses a continuous Galerkin finite

element framework. The development of CHAR was greatly influenced by the finite element approach developed by Dec [76].

In this thesis, a new modeling approach which complements and extends the capabilities of existing codes described in this section is proposed.

1.4 Summary of Proposed Computational Modeling Framework

It is clear that there is a need for a comprehensive computational modeling framework of the coupled thermo-chemo-mechanical response of ablative materials. The modeling framework should be grounded in a continuum theory that contemplates the phenomena discussed in the previous sections: heat conduction in the solid material, chemical kinetics of the pyrolysis reaction, gas transport and advection of thermal energy within the porous material, mechanical response of the solid material due to thermal and chemical effects, and thermochemical ablation phenomena. Starting from basic kinematics, balance laws, and constitutive theory for the multiphase system, a comprehensive theory is developed that encompasses the aforementioned phenomena. The theory is then specialized to the case of ablative thermal protection systems. Finally, a numerical method is adopted to solve the coupled initial boundary value problem.

To this end, a Lagrangian continuum framework to model the coupled thermo-chemo-mechanical response of ablative materials is proposed. Established constitutive models were adopted for the mechanical, thermal, mass transfer, and chemical problems, respectively. A thermoelastic constitutive model was chosen to describe the response of solid material. Fourier's Law of Heat Conduction was chosen to model heat conduction in the solid, while Darcy's Law was used to model the gas mass flux in the porous media. Finally, the chemical reaction is described using a pyrolysis model. A system of equations formed by the solid/gas mixture energy balance equation and gas mass balance are used to solve for the gas pressure and temperature of the continuum. The ablation of the material is modeled by using a surface energy balance equation along with a thermochemical equilibrium model. The governing equations are solved using a high-order finite element method known as the discontinuous Galerkin (DG) method, as developed in [77–79]. The representation of surface ablation is numerically achieved by using a mesh recession algorithm. Finally, the solid mechanics and heat and mass transport equations are coupled using a staggered approach.

In Chapter 2, the comprehensive continuum theory is formulated. The governing equations are derived for the multiphase system. First, a kinematic description of the system is presented, followed by the derivation of the balance laws for mass, linear momentum, angular momentum, and energy. Next, an imbalance of entropy and free energy is introduced, serving as a basis for deriving a constitutive theory for the multiphase system.

In Chapter 3, the theory is specialized to the case of ablative thermal protection systems. First, the governing equations are specialized to the small deformation case. Subsequently, a linear thermoelastic constitutive model is presented, followed by constitutive models for

the heat and mass fluxes. Additionally, a description of the pyrolysis reaction kinetics is provided via the introduction of two different pyrolysis models. Finally, a surface energy balance equation is presented to determine the surface temperature and recession rate for the TPS material.

In Chapter 4, the methods employed within the numerical framework to solve the governing equations are introduced. The Lagrangian/DG weak formulation for the solid mechanics, heat transfer, and mass transport equations are presented. Then the solution procedure for the solid mechanics system is explained. Following this, the procedure for mesh recession/smoothing is examined. Finally, the coupling strategy between the solid mechanics, heat transfer, and mass transport problems is explained.

In Chapter 5, various numerical results are showcased. Each pyrolysis model that was implemented in $\sum$MIT was demonstrated. Subsequently, verification cases of the energy balance equation are presented, including well-known analytical solutions to the heat equation and the Ablation Workshop Test Case series [64, 65]. Following this, a verification of the mesh recession algorithm is demonstrated through a series of patch tests. Finally, a thermo-chemo-mechanical simulation of an arc-jet experiment is presented.

Chapter 6 presents the summary and conclusions.

Chapter 2

Thermo-Chemo-Mechanics Continuum Theory

Conservation laws for momentum and energy transport in a control volume are naturally represented by an Eulerian description. This formulation is widely adopted for material response models of thermal protection systems. There are cases, however, in which the conventional Eulerian approach is unduly cumbersome. Such is the case, for instance, of solids undergoing large deformations, which require the inclusion of grid convection terms and the tracking of solid mechanics boundaries. An alternative approach that eliminates these special treatments is a Lagrangian formulation, which casts the principles of continuum mechanics in so-called material coordinates. Such a description is a natural choice because constitutive models are often expressed in terms of material coordinates, and is extensively adopted in the solid mechanics literature.

The formulation developed in this section includes the following key components: 1) a kinematic description of motion and deformation, 2) a balance of forces and moments, 3) a balance of mass, 4) a balance of energy, and 5) an imbalance principle of entropy and free energy. Much of the notation employed in this segment is adopted from Anand [80]. A substantial portion of the discourse also draws from Gurtin's exposition on continuum mechanics [81].

2.1 Kinematics

A body in space in a certain configuration is denoted by B. At some arbitrarily defined time, the coordinates of a material point in the body B are denoted by $\mathbf{X}$, which are referred to as material coordinates. The corresponding arrangement of the body is referred to as the reference configuration. The configuration of the body at a later time t is denoted by B_t. The coordinates of a material point in B_t are denoted by $\mathbf{x}$ and are referred to as spatial coordinates. A mapping of material to spatial coordinates can be established by a smooth

function $\boldsymbol{\chi}$ which is known as the motion of B:

$$\mathbf{x} = \boldsymbol{\chi}(\mathbf{X}, t) \tag{2.1}$$

$\boldsymbol{\chi}$ is hereafter assumed to be a one-to-one mapping (i.e., invertible).

The motion $\boldsymbol{\chi}$ induces changes in the length of a referential infinitesimal line segment $d\mathbf{X}$ to its deformed image $d\mathbf{x}$. The relationship between these line segments can be expressed by recourse to a Taylor series expansion of $\boldsymbol{\chi}(\mathbf{X}, t)$:

$$d\mathbf{x} = \frac{\partial \boldsymbol{\chi}}{\partial \mathbf{X}} d\mathbf{X} + o(\|d\mathbf{X}\|) \tag{2.2}$$

In the limit as $\|d\mathbf{X}\| \to 0$, the higher order terms can be neglected, exposing a linear mapping between $d\mathbf{X}$ and $d\mathbf{x}$. This resulting second-order tensor is known as the deformation gradient tensor $\mathbf{F}$:

$$\mathbf{F}(\mathbf{X}, t) = \frac{\partial}{\partial \mathbf{X}} \boldsymbol{\chi}(\mathbf{X}, t) = \frac{\partial \mathbf{x}}{\partial \mathbf{X}} \tag{2.3}$$

The deformation gradient tensor is a two-point tensor since it involves two different configurations of the body i.e., it maps material vectors to spatial vectors.

The Jacobian determinant describes changes in volume due to deformation:

$$J(\mathbf{X}, t) = \det \mathbf{F}(\mathbf{X}, t) = \frac{dv}{dv_R}, \tag{2.4}$$

where dv_R and dv are the infinitesimal volume elements in the reference and deformed configurations, respectively.

Standard expositions of finite deformation kinematics introduce the right Cauchy-Green deformation tensor $\mathbf{C}$ [81]:

$$\mathbf{C} = \mathbf{F}^\top \mathbf{F} \tag{2.5}$$

$\mathbf{C}$ is a symmetric, positive-definite tensor that maps material vectors to material vectors. It characterizes the stretch of referential line segments [81].

2.2 Balance of Forces and Moments

An arbitrary subregion $\mathcal{P}_t \subseteq B_t$ has a boundary $\partial\mathcal{P}_t$ with a unit normal vector $\mathbf{n}$. The subregion is subject to a generalized body force $\mathbf{b}$ within $\mathcal{P}_t$ and surface traction $\mathbf{t}(\mathbf{n})$ on $\partial\mathcal{P}_t$. The generalized body force $\mathbf{b}$ is defined by:

$$\mathbf{b} = \mathbf{b}_0 - \rho \dot{\boldsymbol{v}}, \tag{2.6}$$

where $\mathbf{b}_0$ is the body force per unit mass, and $\boldsymbol{v}$ is the velocity of the body. The global conservation of linear momentum balances the net surface and volumetric forces:

$$\int_{\partial\mathcal{P}_t} \mathbf{t}(\mathbf{n})\, da + \int_{\mathcal{P}_t} \mathbf{b}\, dv = \mathbf{0} \tag{2.7}$$

By virtue of Cauchy's tetrahedron argument, there exists a tensor field $\boldsymbol{\sigma}$ that linearly maps $\mathbf{n}$ to $\mathbf{t}(\mathbf{n})$:

$$\mathbf{t}(\mathbf{n}) = \boldsymbol{\sigma}\mathbf{n} \tag{2.8}$$

The tensor $\boldsymbol{\sigma}$ is known as the Cauchy stress tensor. Thus, the global force balance law (2.7) can be rewritten:

$$\int_{\partial\mathcal{P}_t} \boldsymbol{\sigma}\mathbf{n}\, da + \int_{\mathcal{P}_t} \mathbf{b}\, dv = \mathbf{0} \tag{2.9}$$

The divergence theorem can be applied to obtain an equivalent form of (2.9):

$$\int_{\mathcal{P}_t} (\nabla \cdot \boldsymbol{\sigma} + \mathbf{b})\, dv = \mathbf{0}, \tag{2.10}$$

where ∇ is the spatial gradient operator. Recalling that $\mathcal{P}_t$ is an arbitrary subregion, the localization theorem can be used to convert (2.10) into a local force balance law:

$$\nabla \cdot \boldsymbol{\sigma} + \mathbf{b} = \mathbf{0} \tag{2.11}$$

Similarly, the global conservation of angular momentum balances the moments arising from $\mathbf{t}(\mathbf{n})$ and $\mathbf{b}$:

$$\int_{\partial P_t} \boldsymbol{r} \times \mathbf{t}(\mathbf{n}) + \int_{P_t} \boldsymbol{r} \times \mathbf{b}\, dv = \mathbf{0}, \tag{2.12}$$

where $\boldsymbol{r}$ is the position vector. An analogous procedure to the preceding analysis of linear momentum conservation yields the local balance of moments, which states that $\boldsymbol{\sigma}$ is symmetric:

$$\boldsymbol{\sigma} = \boldsymbol{\sigma}^\top \tag{2.13}$$

The Lagrangian formulation of mechanics requires an expression of the balance of forces and moments in material coordinates. For this reason, a different stress measure $\mathbf{P}$, known as the first Piola-Kirchhoff stress tensor, is defined:

$$\mathbf{P} = J\boldsymbol{\sigma}\mathbf{F}^{-T} \tag{2.14}$$

$\mathbf{P}$ represents the force measured in the deformed configuration per unit reference area. The referential generalized body force $\mathbf{b}_R$ is a scaling of $\mathbf{b}$ that accounts for the change in volume due to deformation:

$$\mathbf{b}_R = J\mathbf{b} \tag{2.15}$$

Equations (2.9) and (2.12) expressed in material coordinates for an arbitrary subregion $\mathcal{P} \subseteq B$ are:

$$\int_{\partial\mathcal{P}} \mathbf{P}\mathbf{n}_R\, da_R + \int_{\mathcal{P}} \mathbf{b}_R\, dv_R = \mathbf{0} \tag{2.16}$$

$$\int_{\partial\mathcal{P}} \mathbf{r} \times \mathbf{P}\mathbf{n}_R\, da_R + \int_{\mathcal{P}} \mathbf{r} \times \mathbf{b}_R\, dv_R = \mathbf{0}, \tag{2.17}$$

where $\mathbf{n}_R$ is the unit normal vector in the reference configuration. The referential forms of (2.11) and (2.13) are:

$$\nabla_0 \cdot \mathbf{P} + \mathbf{b}_R = \mathbf{0} \tag{2.18}$$

$$\mathbf{P}\mathbf{F}^\top = \mathbf{F}\mathbf{P}^\top, \tag{2.19}$$

where ∇_0 is the material gradient operator.

Initial and boundary conditions are required to have a well-posed problem statement of (2.18) and (2.19). The boundary ∂B is divided into Neumann and Dirichlet sub-boundaries, denoted as $\partial_N B$ and $\partial_D B$, respectively:

$$\partial B = \partial_N B \cup \partial_D B \tag{2.20}$$

These sub-boundaries are disjoint:

$$\partial_N B \cap \partial_D B = \emptyset \tag{2.21}$$

The specified boundary conditions are:

$$\mathbf{u} = \bar{\mathbf{u}} \quad \text{on } \partial_D B \tag{2.22}$$

$$\mathbf{P}\mathbf{n}_R = \bar{\mathbf{t}}_R \quad \text{on } \partial_N B, \tag{2.23}$$

where $\bar{\mathbf{u}}$ and $\bar{\mathbf{t}}_R$ are the prescribed displacement and referential traction, respectively.

2.3 Balance of Mass

2.3.1 Solid Mass Balance

For a spatial region $\mathcal{P}_t \subseteq B$, the global balance of mass is:

$$\int_{\mathcal{P}_t} \rho \, dv = \int_{\mathcal{P}} \rho_R \, dv_R, \tag{2.24}$$

where ρ_R is the mass density in the reference configuration. Recalling the definition of J as the ratio of the spatial to reference infinitesimal volume elements, the global balance of mass can be expressed as:

$$\int_{\mathcal{P}} (\rho_R - \rho J) \, dv_R \tag{2.25}$$

Thus by localization theorem, the local balance of mass is:

$$\rho = \frac{\rho_R}{J} \tag{2.26}$$

The mass density ρ is a mixture of the solid and gas densities ρ_s and ρ_g, respectively:

$$\rho = \rho_s + \phi \rho_g, \tag{2.27}$$

where ϕ is the porosity of the solid, ρ_s is the solid density, and ρ_g is the gas density.

An important departure from the standard formulation of solid mechanics is the solid mass loss in the reference configuration due to chemical reactions. In particular, solid mass due to pyrolysis is converted into gas. To account for this effect, the solid mass balance equation is modified to include a mass source term $\dot{\omega}_g$:

$$\frac{\partial \rho_s}{\partial t} = -\dot{\omega}_g \tag{2.28}$$

The pyrolysis model used to compute the mass source term $\dot{\omega}_g$ will be described in detail in a later section. Also, the mass source term $\dot{\omega}_g$ is used in the gas mass conservation equation, providing a link between the solid and gas phases.

2.3.2 Gas Mass Balance

The subregion $\mathcal{P}_t \subseteq B$ is subject to a gas mass per unit volume of bulk material $\phi\rho_g$ within $\mathcal{P}_t$, a gas mass source term $\dot{\omega}_g$ within $\mathcal{P}_t$ due to pyrolysis, and a gas mass flux $\mathbf{q}_{\text{mass}}$ on $\partial\mathcal{P}_t$. To represent this phenomenon, a global gas mass conservation equation of $\mathcal{P}_t$ is introduced:

$$\dot{\int_{\mathcal{P}_t} \phi\rho_g \, dv} = \int_{\partial\mathcal{P}_t} \mathbf{q}_{\text{mass}} \cdot \mathbf{n} \, da_R + \int_{\mathcal{P}_t} \dot{\omega}_g \, dv_R, \tag{2.29}$$

where $\mathbf{q}_{\text{mass}}$ is the mass flux vector.

By applying the divergence and localization theorem to (2.29) becomes:

$$\dot{\phi\rho_g} = -\nabla \cdot (\mathbf{q}_{\text{mass}}) + \dot{\omega}_g \tag{2.30}$$

The boundary conditions of (2.30) are:

$$\mathbf{q}_{\text{mass}} \cdot \mathbf{n} = \dot{m}_g \text{ on } \partial_N B \tag{2.31}$$

$$\rho_g = \bar{\rho}_g \text{ on } \partial_D B \tag{2.32}$$

The corresponding initial condition of (2.30) is:

$$\rho_g(\mathbf{X}, 0) = \rho_{g0}(\mathbf{X}) \text{ in } B \tag{2.33}$$

2.4 Balance of Energy

The subregion $\mathcal{P}_t \subseteq B_t$ with density ρ is subject to an internal energy per unit mass ε and a volumetric heat source q within $\mathcal{P}_t$, and a heat flux $\mathbf{q}_{\text{heat}}$ on $\partial\mathcal{P}_t$. In referential form, the quantities ε_R, q_R, and $\mathbf{q}_{\text{heat}}$ are related to their spatial counterparts by:

$$\varepsilon_R = \rho_R \varepsilon \tag{2.34}$$

$$q_R = Jq \tag{2.35}$$

$$\mathbf{q}_R = J\mathbf{F}^{-1}\mathbf{q}_{\text{heat}} \tag{2.36}$$

The global conservation of energy is derived from the first law of thermodynamics, which states that the rate of change of the total internal and kinetic energy of $\mathcal{P}_t$ is equal to the rate at which heat is added to $\mathcal{P}_t$ and the external mechanical power applied to $\mathcal{P}_t$. To arrive at a global balance of energy, a definition of the net internal energy $\mathcal{E}(\mathcal{P}_t)$, the net kinetic energy $\mathcal{K}(\mathcal{P}_t)$, the heat flow $\mathcal{Q}(\mathcal{P}_t)$, and the external mechanical power $\mathcal{W}(\mathcal{P}_t)$ are introduced in spatial and referential forms:

$$\mathcal{E}(\mathcal{P}_t) = \int_{\mathcal{P}_t} \rho\varepsilon \, dv = \int_{\mathcal{P}} \varepsilon_R \, dv_R \tag{2.37}$$

$$\mathcal{K}(\mathcal{P}_t) = \int_{\mathcal{P}_t} \frac{1}{2}\rho \mathbf{v}\cdot\mathbf{v} \, dv = \int_{\mathcal{P}} \frac{1}{2}\rho_R \mathbf{v}\cdot\mathbf{v} \, dv_R \tag{2.38}$$

$$\mathcal{Q}(\mathcal{P}_t) = -\int_{\partial\mathcal{P}_t} \mathbf{q}_{\text{heat}}\cdot\mathbf{n} \, da + \int_{\mathcal{P}_t} q \, dv = -\int_{\partial\mathcal{P}} \mathbf{q}_R\cdot\mathbf{n}_R \, da_R + \int_{\mathcal{P}} q_R \, dv \tag{2.39}$$

$$\mathcal{W}_{\text{ext}} = \int_{\partial\mathcal{P}_t} \boldsymbol{\sigma}\mathbf{n}\cdot\mathbf{v} \, da + \int_{\mathcal{P}_t} \mathbf{b}\cdot\mathbf{v} \, dv = \int_{\partial\mathcal{P}} \mathbf{P}\mathbf{n}_R\cdot\mathbf{v} \, da_R + \int_{\mathcal{P}} \mathbf{b}_{0R}\cdot\mathbf{v} \, dv_R, \tag{2.40}$$

The global energy balance in referential form is:

$$\begin{aligned}\dot{\int_{\mathcal{P}} \left(\varepsilon_R + \frac{1}{2}\rho_R|\mathbf{v}|^2\right) dv_R} = &-\int_{\partial\mathcal{P}} \mathbf{q}_R\cdot\mathbf{n}_R \, da_R + \int_{\mathcal{P}} q_R \, dv_R \\ &+ \int_{\partial\mathcal{P}} \mathbf{P}\mathbf{n}_R\cdot\mathbf{v} \, da_R + \int_{\mathcal{P}} \mathbf{b}_{0R}\cdot\mathbf{v} \, dv_R\end{aligned} \tag{2.41}$$

Using a standard procedure invoking the divergence and localization theorems, (2.41) can be re-expressed as a local balance law:

$$\dot{\varepsilon}_R = -\nabla_0\cdot\mathbf{q}_R + q_R + \mathbf{P}:\dot{\mathbf{F}} \tag{2.42}$$

Alternatively, this can be written as:

$$\dot{\varepsilon}_R = -\nabla\cdot(\mathbf{q}_R) + q_R + \frac{1}{2}\mathbf{S}:\dot{\mathbf{C}}, \tag{2.43}$$

where $\mathbf{S}$ is the second Piola-Kirchhoff stress tensor, which can be derived as the stress-conjugate of $\frac{1}{2}\dot{\mathbf{C}}$.

To have a well-posed statement of (2.42), the boundary conditions are specified as follows:

$$\theta = \bar{\theta} \text{ on } \partial_D B, \tag{2.44}$$

$$\mathbf{q}_R\cdot\mathbf{n}_R = \bar{q} \text{ on } \partial_N B \tag{2.45}$$

where $\bar{\theta}$ and $\bar{q}$ are the prescribed temperature and heat flux on the boundary. Additionally, initial conditions are required:

$$\theta(\mathbf{X}, 0) = \theta_0(\mathbf{X}) \text{ in } B, \tag{2.46}$$

where θ_0 is the initial temperature distribution.

2.5 Free-Energy Imbalance

The subregion $\mathcal{P}_t \subseteq B_t$ has an entropy per unit mass η which is influenced by a volumetric entropy supply j within $\mathcal{P}_t$, and an entropy flux $\mathbf{j}$ across $\partial\mathcal{P}_t$. In the reference configuration, the quantities η_R, j_R, and $\mathbf{j}_R$ are related to their spatial counterparts by:

$$\eta_R = \rho_R \eta, \tag{2.47}$$

$$j_R = Jj \tag{2.48}$$

$$\mathbf{j}_R = J\mathbf{F}^{-1}\mathbf{j} \tag{2.49}$$

The global entropy imbalance equation is derived from the second law of thermodynamics, which states that the entropy of an isolated system never decreases. To arrive at a global imbalance of free energy, a definition of the net entropy $\mathcal{S}(\mathcal{P}_t)$ and the entropy flow $\mathcal{J}(\mathcal{P}_t)$ are introduced in spatial and referential form:

$$\mathcal{S}(\mathcal{P}_t) = \int_{\mathcal{P}_t} \rho\eta \, dv = \int_{\mathcal{P}} \eta_R \, dv_R \tag{2.50}$$

$$\mathcal{J}(\mathcal{P}_t) = -\int_{\partial\mathcal{P}_t} \mathbf{j}\cdot\mathbf{n} \, da + \int_{\mathcal{P}_t} j \, dv = -\int_{\partial\mathcal{P}} \mathbf{j}_R \cdot \mathbf{n}_R \, da_R + \int_{\mathcal{P}} j_R \, dv_R \tag{2.51}$$

Furthermore, the entropy flux and entropy supply are given by:

$$\mathbf{j} = \frac{\mathbf{q}_{\text{heat}}}{\theta} \tag{2.52}$$

$$j = \frac{q}{\theta} \tag{2.53}$$

The global form of the entropy imbalance equation is:

$$\dot{\overline{\int_{\mathcal{P}} \eta_R \, dv_R}} \geq -\int_{\partial\mathcal{P}} \frac{\mathbf{q}_R}{\theta}\cdot\mathbf{n}_R \, da_R + \int_{\mathcal{P}} \frac{q_R}{\theta} \, dv_R \tag{2.54}$$

This expression is also known as the Clausius-Duhem inequality.

The local form of the entropy imbalance equation can be obtained after applying the divergence and localization theorems to (2.54):

$$\dot{\eta}_R \geq -\nabla_0 \cdot \left(\frac{\mathbf{q}_R}{\theta}\right) + \frac{q_R}{\theta} \tag{2.55}$$

By recourse to a Legendre transform, the Helmholtz free energy is defined as:

$$\psi_R = \varepsilon_R - \theta\eta_R \tag{2.56}$$

The local free-energy imbalance can be obtained as:

$$\dot{\psi_R} + \eta_R\dot{\theta} - \frac{1}{2}\mathbf{S} : \dot{\mathbf{C}} + \frac{1}{\theta}\mathbf{q}_R \cdot \nabla\theta \leq 0 \tag{2.57}$$

2.6 Constitutive Theory

While the field equations described in the previous sections apply to any continuum, the behavior of a material depends on its specific constitution. Constitutive theories model the material response in terms of its state under a suitable set of assumptions. Concretely, the state is assumed to depend on $\mathbf{F}$, θ, and $\nabla_0\theta$. Additional restrictions are also imposed on the constitutive model: material-frame indifference and thermodynamic consistency. The principle of material frame-indifference requires that certain quantities are independent of the frame of reference [82]:

$$\hat{\psi}_R\left(\mathbf{F}, \theta, \nabla_0\theta\right) = \hat{\psi}_R\left(\mathbf{Q}\mathbf{F}, \theta, \nabla_0\theta\right), \tag{2.58}$$

where $\mathbf{Q}$ is any rotation tensor. Thermodynamic consistency enforces the second law of thermodynamics (2.55) and its consequence, the free-energy imbalance (2.57), in the constitutive model [83].

To satisfy the first requirement, it can be shown that the constitutive model must be expressable in terms of $\mathbf{C}$ [81]. ψ_R, $\mathbf{P}$, η_R, and $\mathbf{q}_R$ are therefore assumed to have the following functional forms:

$$\psi_R = \hat{\psi}_R\left(\mathbf{C}, \theta, \nabla_0\theta\right) \tag{2.59}$$

$$\mathbf{P} = \hat{\mathbf{P}}\left(\mathbf{C}, \theta, \nabla_0\theta\right) \tag{2.60}$$

$$\eta_R = \hat{\eta}_R\left(\mathbf{C}, \theta, \nabla_0\theta\right) \tag{2.61}$$

$$\mathbf{q}_R = \hat{\mathbf{q}}_R\left(\mathbf{C}, \theta, \nabla_0\theta\right) \tag{2.62}$$

Regarding the second requirement, the constitutive model must satisfy the free-energy imbalance (2.55). This is accomplished by applying the Coleman-Noll procedure to the constitutive assumptions [83]. Differentiating the free-energy density ψ_R with respect to time yields the following:

$$\dot{\psi}_R = \frac{\partial \psi_R}{\partial \mathbf{C}} : \dot{\mathbf{C}} + \frac{\partial \psi_R}{\partial \theta}\dot{\theta} + \frac{\partial \psi_R}{\partial \nabla_0\theta} \cdot \dot{\overline{\nabla_0\theta}} \tag{2.63}$$

Substituting this result into (2.57) gives:

$$\left(\frac{\partial \psi_R}{\partial \mathbf{C}} - \frac{1}{2}\mathbf{S}\right) : \dot{\mathbf{C}} + \left(\frac{\partial \psi_R}{\partial \theta} + \eta_R\right)\dot{\theta} + \frac{\partial \psi_R}{\partial \nabla_0\theta} \cdot \dot{\overline{\nabla_0\theta}} + \frac{1}{\theta}\mathbf{q}_R \cdot \nabla_0\theta \leq 0 \tag{2.64}$$

Since (2.64) must be satisfied for all choices of $\mathbf{C}$, θ, $\nabla_0\theta$, and their time derivatives, the following relationships are obtained:

$$\psi_R = \hat{\psi}_R\left(\mathbf{C}, \theta\right) \tag{2.65}$$

$$\mathbf{S} = 2\frac{\partial \hat{\psi}_R\left(\mathbf{C}, \theta\right)}{\partial \mathbf{C}} \tag{2.66}$$

$$\eta_R = -\frac{\partial \hat{\psi}_R\left(\mathbf{C}, \theta\right)}{\partial \theta} \tag{2.67}$$

Finally, (2.64) reduces to the dissipation inequality:

$$\mathbf{q}_R \cdot \nabla_0 \theta \leq 0 \tag{2.68}$$

The constitutive theory presented models a wide variety of thermoelastic materials. Although not discussed here, the framework can be extended to include inelastic material behavior such as plasticity, viscoelasticity, and fracture by introducing a set of internal variables.

Chapter 3

Specialization of the Thermo-Chemo-Mechanics Formulation to Ablative Thermal Protection Systems

The preceding section introduced the broad conceptual framework of a finite deformation thermo-chemo-mechanical continuum theory. However, specific constitutive models were not described. In this section, a specialized thermo-chemo-mechanical continuum theory is developed for ablative thermal protection systems. In particular, the balance laws are expressed in the case of small deformations. A linear thermoelastic constitutive model is adopted for the solid mechanical response. The heat and mass fluxes are described with nonlinear constitutive models. Also, an internal energy model is introduced for a solid/gas mixture. Following this, two pyrolysis models are described. Finally, the thermochemical surface energy and mass balance boundary conditions are introduced.

3.1 Balance Laws for Small Deformation

The balance laws for a deformable body occupying the region B can be simplified when the deformation is small:

$$\|\nabla \mathbf{u}\| \ll 1 \tag{3.1}$$

In this limit, the changes in area and volume are negligible:

$$da \approx da_R \tag{3.2}$$

$$dv \approx dv_R \tag{3.3}$$

The difference between material and spatial gradients also becomes insignificant:

$$\nabla \approx \nabla_0 \tag{3.4}$$

As a consequence, spatial quantities are approximately equivalent to their referential counterparts:

$$\rho_R \approx \rho \tag{3.5}$$

$$\mathbf{b} \approx \mathbf{b}_R \tag{3.6}$$

$$\mathbf{q}_{\text{heat}} \approx \mathbf{q}_R \tag{3.7}$$

$$\boldsymbol{\sigma} \approx \mathbf{P} \approx \mathbf{S} \tag{3.8}$$

$$q \approx q_R \tag{3.9}$$

$$\psi \approx \psi_R \tag{3.10}$$

$$\eta \approx \eta_R \tag{3.11}$$

The small-deformation internal energy used here is per unit mass:

$$\rho\varepsilon \approx \varepsilon_R \tag{3.12}$$

Instead of $\mathbf{F}$, small-deformation kinematics is described by the infinitesimal strain tensor $\boldsymbol{\epsilon}$:

$$\boldsymbol{\epsilon} = \frac{1}{2}\left(\nabla\mathbf{u} + (\nabla\mathbf{u})^{\top}\right) \tag{3.13}$$

The local principles (2.11), (2.13), (2.42), and (2.57) for small deformations can be expressed as follows:

$$\nabla \cdot \boldsymbol{\sigma} + \mathbf{b} = \rho\ddot{\boldsymbol{u}} \tag{3.14}$$

$$\boldsymbol{\sigma} = \boldsymbol{\sigma}^{T} \tag{3.15}$$

$$\dot{\overline{\rho\varepsilon}} = \boldsymbol{\sigma} : \dot{\boldsymbol{\epsilon}} - \nabla \cdot \mathbf{q}_{\text{heat}} + q \tag{3.16}$$

$$\dot{\psi} + \eta\dot{\theta} - \boldsymbol{\sigma} : \dot{\boldsymbol{\epsilon}} + \frac{1}{\theta}\mathbf{q}_{\text{heat}} \cdot \nabla\theta \leq 0 \tag{3.17}$$

3.2 Solid/Gas Mixture Internal Energy and Specific Heat Capacity

The solid/gas mixture internal energy in the local form of the energy conservation equation (3.16) is defined using a rule of mixtures approach of the char and virgin solid phases, and the evolved gas phase. In the remainder of this thesis, the subscripts b, g, s, c, and v will be used to denote the solid/gas bulk mixture, gas, solid, char solid, and virgin solid phases, respectively. The internal energy per unit mass of the mixture is expressed as follows:

$$\rho\varepsilon = \beta\rho_c\varepsilon_c + (1-\beta)\,\rho_v\varepsilon_v + \phi\rho_g\varepsilon_g, \tag{3.18}$$

where β denotes the degree of char and is defined by:

$$\beta = \frac{\rho_s - \rho_v}{\rho_c - \rho_v} \tag{3.19}$$

The internal energy of the char, virgin, and gas phases are defined by:

$$\varepsilon_c = h_c \tag{3.20}$$

$$\varepsilon_v = h_v \tag{3.21}$$

$$\varepsilon_g = h_g - \frac{p}{\rho_g} \tag{3.22}$$

Substituting (3.20), (3.21), and (3.20) into (3.18) yields:

$$\rho\varepsilon = \beta\rho_c h_c + (1-\beta)\,\rho_v h_v + \phi\rho_g\left(h_g - \frac{p}{\rho_g}\right) \tag{3.23}$$

By taking the time derivative of (3.23), the transient term of (3.16) can be expressed in terms of the individual phases as follows:

$$\begin{aligned}\dot{\overline{\rho\varepsilon}} = {} & (\rho_c h_c - \rho_v h_v)\frac{\partial\beta}{\partial t} \\ & + \left(\beta\rho_c\frac{\partial h_c}{\partial\theta} + (1-\beta)\,\rho_v\frac{\partial h_v}{\partial\theta}\right)\dot{\theta} + \frac{\partial}{\partial t}\left[\phi\rho_g\left(h_g - \frac{p}{\rho_g}\right)\right]\end{aligned} \tag{3.24}$$

Since the degree of char is a function of the solid density, the time derivative of β is given by:

$$\frac{\partial\beta}{\partial t} = \frac{1}{\rho_c - \rho_v}\frac{\partial\rho_s}{\partial t} \tag{3.25}$$

Thus (3.25) can be substituted into (3.24) to obtain:

$$\begin{aligned}\dot{\overline{\rho\varepsilon}} = {} & \frac{\rho_c h_c - \rho_v h_v}{\rho_c - \rho_v}\frac{\partial\rho_s}{\partial t} \\ & + \left(\beta\rho_c\frac{\partial h_c}{\partial\theta} + (1-\beta)\,\rho_v\frac{\partial h_v}{\partial\theta}\right)\dot{\theta} + \frac{\partial}{\partial t}\left[\phi\rho_g\left(h_g - \frac{p}{\rho_g}\right)\right]\end{aligned} \tag{3.26}$$

A further simplification can be made by defining a quantity $\bar{h}$, known as the partial heat of charring, which is a measure of the heat released by the solid phase as it undergoes pyrolysis [46]:

$$\bar{h} = \frac{\rho_c h_c - \rho_v h_v}{\rho_c - \rho_v} \tag{3.27}$$

With this substitution, (3.26) becomes:

$$\begin{aligned}\dot{\overline{\rho\varepsilon}} = {} & \bar{h}\frac{\partial\rho_s}{\partial t} + \left(\beta\rho_c\frac{\partial h_c}{\partial\theta} + (1-\beta)\,\rho_v\frac{\partial h_v}{\partial\theta}\right)\dot{\theta} \\ & + \frac{\partial}{\partial t}\left[\phi\rho_g\left(h_g - \frac{p}{\rho_g}\right)\right]\end{aligned} \tag{3.28}$$

Next, the weighting factors y_c and y_v are introduced:

$$y_c = \beta\frac{\rho_c}{\rho_s} \tag{3.29}$$

$$y_v = (1-\beta)\frac{\rho_v}{\rho_s} \tag{3.30}$$

Using these weighting factors, (3.28) can be written as:

$$\dot{\overline{\rho\varepsilon}} = \bar{h}\frac{\partial \rho_s}{\partial t} + \left(y_c\rho_s\frac{\partial h_c}{\partial \theta} + y_v\rho_s\frac{\partial h_v}{\partial \theta}\right)\dot{\theta} + \frac{\partial}{\partial t}\left[\phi\rho_g\left(h_g - \frac{p}{\rho_g}\right)\right] \tag{3.31}$$

Furthermore, the derivative of the internal energy of the virgin and char phases with respect to temperature yield the specific heat of the char and virgin phases:

$$c_{p,c} = \frac{\partial h_c}{\partial \theta} \tag{3.32}$$

$$c_{p,v} = \frac{\partial h_v}{\partial \theta} \tag{3.33}$$

Substituting (3.32) and (3.33) into (3.31) yields:

$$\dot{\overline{\rho\varepsilon}} = \bar{h}\frac{\partial \rho_s}{\partial t} + \rho_s\left(y_c c_{p,c} + y_v c_{p,v}\right)\dot{\theta} + \frac{\partial}{\partial t}\left[\phi\rho_g\left(h_g - \frac{p}{\rho_g}\right)\right] \tag{3.34}$$

The total specific heat of the solid mixture is defined by a rule of mixtures of the solid and gas phases:

$$c_{p,s} = y_c c_{p,c} + y_v c_{p,v}, \tag{3.35}$$

which simplifies (3.34) to:

$$\dot{\overline{\rho\varepsilon}} = \bar{h}\frac{\partial \rho_s}{\partial t} + \rho_s c_{p,s}\dot{\theta} + \frac{\partial}{\partial t}\left[\left(h_g - \frac{p}{\rho_g}\right)\right] \tag{3.36}$$

The product rule is used to expand the time derivative of the gas phase enthalpy:

$$\dot{\overline{\rho\varepsilon}} = \bar{h}\frac{\partial \rho_s}{\partial t} + \rho_s c_{p,s}\dot{\theta} + \phi\rho_g\frac{\partial}{\partial t}\left(h_g - \frac{p}{\rho_g}\right) + \left(h_g - \frac{p}{\rho_g}\right)\frac{\partial\left(\phi\rho_g\right)}{\partial t} \tag{3.37}$$

Next, then the chain rule is used to expand the time derivative of the gas phase enthalpy:

$$\dot{\overline{\rho\varepsilon}} = \bar{h}\frac{\partial \rho_s}{\partial t} + \left(\rho_s c_{p,s} + \phi\rho_g\frac{\partial h_g}{\partial \theta}\right)\dot{\theta} - \phi\rho_g\frac{\partial}{\partial t}\left(\frac{p}{\rho_g}\right) + \left(h_g - \frac{p}{\rho_g}\right)\frac{\partial\left(\phi\rho_g\right)}{\partial t} \tag{3.38}$$

The gas specific enthalpy can be expressed as:

$$c_{p,g} = \frac{\partial h_g}{\partial \theta} \tag{3.39}$$

With this definition, (3.38) becomes:

$$\dot{\overline{\rho\varepsilon}} = \bar{h}\frac{\partial \rho_s}{\partial t} + \left(\rho_s c_{p,s} + \phi\rho_g c_{p,g}\right)\dot{\theta} - \phi\rho_g\frac{\partial}{\partial t}\left(\frac{p}{\rho_g}\right) + \left(h_g - \frac{p}{\rho_g}\right)\frac{\partial\left(\phi\rho_g\right)}{\partial t} \tag{3.40}$$

To further simplify the transient term, new weighting factors for the gas and solid phases are introduced:

$$y_g = \frac{\phi \rho_g}{\rho} \tag{3.41}$$

$$y_s = \frac{\rho_s}{\rho} \tag{3.42}$$

Thus (3.40) becomes:

$$\dot{\overline{\rho\varepsilon}} = \bar{h}\frac{\partial \rho_s}{\partial t} + \rho \left(y_s c_{p,s} + y_g c_{p,g}\right) \dot{\theta} - \phi \rho_g \frac{\partial}{\partial t}\left(\frac{p}{\rho_g}\right) + \left(h_g - \frac{p}{\rho_g}\right) \frac{\partial \left(\phi \rho_g\right)}{\partial t} \tag{3.43}$$

The total specific energy of the gas/solid mixture can be defined as:

$$c_{p,b} = y_s c_{p,s} + y_g c_{p,g} \tag{3.44}$$

Substituting (3.44) into (3.43), the transient term becomes:

$$\dot{\overline{\rho\varepsilon}} = \bar{h}\frac{\partial \rho_s}{\partial t} + \rho c_{p,b} \dot{\theta} - \phi \rho_g \frac{\partial}{\partial t}\left(\frac{p}{\rho_g}\right) + \left(h_g - \frac{p}{\rho_g}\right) \frac{\partial \left(\phi \rho_g\right)}{\partial t} \tag{3.45}$$

3.3 Linear Thermoelastic Constitutive Model

A specialization of the constitutive response functions (2.59), (2.60), (2.61) in the small deformation limit yields:

$$\psi = \hat{\psi}\left(\boldsymbol{\epsilon}, \theta, \nabla\theta\right) \tag{3.46}$$

$$\boldsymbol{\sigma} = \hat{\boldsymbol{\sigma}}\left(\boldsymbol{\epsilon}, \theta, \nabla\theta\right) \tag{3.47}$$

$$\eta = \hat{\eta}\left(\boldsymbol{\epsilon}, \theta, \nabla\theta\right) \tag{3.48}$$

Following an analogous procedure to that used in the derivation of the finite deformation state relations (2.65), (2.66), and (2.67) the following small-deformation state relations are obtained by applying the Coleman-Noll procedure [83] to (3.17):

$$\psi = \hat{\psi}\left(\boldsymbol{\epsilon}, \theta\right) \tag{3.49}$$

$$\boldsymbol{\sigma} = \frac{\partial \psi}{\partial \boldsymbol{\epsilon}} \tag{3.50}$$

$$\eta = -\frac{\partial \psi}{\partial \theta} \tag{3.51}$$

The corresponding dissipation inequality is:

$$\mathbf{q}_{\text{heat}} \cdot \nabla\theta \leq 0 \tag{3.52}$$

A linear thermoelastic constitutive model can be derived by recourse to a Taylor series expansion of ψ about $\boldsymbol{\epsilon} = \mathbf{0}$ and $\theta = \theta_0$ up to second-order terms:

$$\psi = \frac{1}{2}\boldsymbol{\epsilon} : \mathbb{C}\boldsymbol{\epsilon} + (\theta - \theta_0)\,\mathbf{M} : \boldsymbol{\epsilon} - \frac{c_p}{2\theta_0}\,(\theta - \theta_0)^2\,, \tag{3.53}$$

where c_p is given by:

$$c_p = \frac{\partial \varepsilon}{\partial \theta}, \tag{3.54}$$

the elasticity tensor $\mathbb{C}$ is given by:

$$\mathbb{C} = \frac{\partial \boldsymbol{\sigma}}{\partial \boldsymbol{\epsilon}} = \frac{\partial^2 \psi}{\partial \boldsymbol{\epsilon}^2}, \tag{3.55}$$

and the stress-temperature tensor $\mathbf{M}$ is defined by:

$$\mathbf{M} = \frac{\partial \boldsymbol{\sigma}}{\partial \theta} = \frac{\partial^2 \psi}{\partial \boldsymbol{\epsilon} \partial \theta}. \tag{3.56}$$

Thus, the derivative of ψ with respect to $\boldsymbol{\epsilon}$ gives an expression for $\boldsymbol{\sigma}$:

$$\boldsymbol{\sigma} = \mathbb{C}\boldsymbol{\epsilon} + \mathbf{M}\,(\theta - \theta_0) \tag{3.57}$$

If the material is isotropic, then $\mathbb{C}$ and $\mathbf{M}$ can be expressed as follows:

$$\mathbb{C} = 2\mu \mathbb{I}^{\mathrm{sym}} + \lambda \mathbf{I} \otimes \mathbf{I} \tag{3.58}$$

$$\mathbf{M} = \beta \mathbf{I} \tag{3.59}$$

In the expressions above, μ and λ are the Lamé constants and β is the stress-temperature modulus. An alternate expression for $\boldsymbol{\sigma}$ can be derived using the following relationships:

$$\kappa = \lambda + \frac{2}{3}\mu \tag{3.60}$$

$$\alpha = -\frac{\beta}{2\mu + 3\lambda}, \tag{3.61}$$

where κ is the bulk modulus and α is the coefficient of thermal expansion. These yield the following expression for $\boldsymbol{\sigma}$:

$$\boldsymbol{\sigma} = 2\mu\boldsymbol{\epsilon} + \lambda\,(\mathrm{tr}\boldsymbol{\epsilon})\,\mathbf{I} - 3\kappa\alpha\,(\theta - \theta_0)\,\mathbf{I} \tag{3.62}$$

3.4 Mass Transport Constitutive Model

A constitutive model for $\mathbf{q}_{\mathrm{mass}}$ in the local gas mass conservation law (2.30) is given by:

$$\mathbf{q}_{\mathrm{mass}} = \rho_g \phi \mathbf{u}_g, \tag{3.63}$$

where $\mathbf{u}_g$ is the gas velocity. The gas velocity is obtained using Darcy's Law, a steady-state momentum equation [43]:

$$\mathbf{u}_g = -\frac{\mathbf{k}}{\phi\mu}\nabla p, \tag{3.64}$$

where $\mathbf{k}$ is a second-order tensor known as the permeability, p denotes gas pressure, and μ represents the dynamic gas viscosity. An important assumption is that the permeability tensor is isotropic. For this reason, the permeability is treated as a scalar and denoted as k. The model also assumes that the permeability depends solely on the extent of reaction [46]:

$$k = \hat{k}\left(y_v\right) = y_v k_v + \left(1 - y_v\right) k_c, \tag{3.65}$$

where y_v is the volume fraction of the virgin solid phase as discussed in Section 3.2. Although not considered here, modifications to Darcy's Law can be made to correct for gas slippage effects [84] or high-velocity gas flows [44].

The gas density is modeled by the ideal gas law equation of state:

$$\rho_g = \frac{p\mathcal{M}}{R\theta}, \tag{3.66}$$

where R denotes the universal gas constant and $\mathcal{M}$ represents the molecular weight of the gas. Substituting (3.64) and (3.66) into (3.63) yields a final expression for the mass flux:

$$\mathbf{q}_{\text{mass}} = -\frac{p\mathcal{M}k}{R\theta\mu}\nabla p \tag{3.67}$$

Several assumptions underlie the model's formulation. One assumption is that of a well-mixed gas in the porous medium. Consequently, μ and $\mathcal{M}$ are assumed to depend solely on temperature. However, in reality, these vary with the evolving composition during the pyrolysis process. To address this, the model can be extended to incorporate individual species tracking as they emerge from chemical reactions, then diffuse and advect in the gas phase.

3.5 Heat Flux Constitutive Model

This section introduces a constitutive model for $\mathbf{q}_{\text{heat}}$ in the local energy conservation equation (3.16). The heat flux can be decomposed into diffusive and advective contributions:

$$\mathbf{q}_{\text{heat}} = \mathbf{q}_{\text{diffusive}} + \mathbf{q}_{\text{advection}} \tag{3.68}$$

The diffusive part is described by Fourier's Law of Heat Conduction:

$$\mathbf{q}_{\text{diffusive}} = -\boldsymbol{\kappa}\nabla\theta, \tag{3.69}$$

where $\boldsymbol{\kappa}$ is a second-order tensor known as the thermal conductivity tensor. A significant assumption made is that the thermal conductivity is isotropic. Throughout this work, thermal conductivity will be treated as a scalar and denoted as κ. The thermal conductivity is represented as a function of temperature and the extent of reaction [46]:

$$\kappa = \hat{\kappa}\left(\theta, y_v\right) = y_v \kappa_v\left(\theta\right) + \left(1 - y_v\right)\kappa_c\left(\theta\right) \tag{3.70}$$

The model assumes a weighted average of the virgin and charred material's thermal conductivities based on the extent of reaction. Notably, only the solid phase is considered, since the gas phase's contribution to the overall thermal conductivity is small.

The advective part is given by the following expression:

$$\mathbf{q}_{\text{advection}} = h_g \phi \rho_g \mathbf{u}_g, \tag{3.71}$$

where h_g is the gas enthalpy. $\mathbf{u}_g$ is obtained using Darcy's Law (3.64).

As discussed in Section 3.4, the well-mixed gas assumption has implications for $\mathbf{u}_g$ and ρ_g. Also, this implies that h_g depends solely on temperature.

The final expression for the heat flux is obtained by substituting (3.69) and (3.71) into (3.68):

$$\mathbf{q}_{\text{heat}} = -\boldsymbol{\kappa}\nabla\theta + h_g \phi \rho_g \mathbf{u}_g \tag{3.72}$$

3.6 Final Form of the Energy and Gas Mass Balance Equations of Ablative Thermal Protection Systems

The final form of the energy balance equation is obtained by substituting (3.68) and (3.45) into (3.16):

$$\begin{aligned}\rho c_p \dot{\theta} = &- \nabla \cdot \left(-\kappa \nabla\theta + h_g \rho \phi_g \mathbf{u}_g\right) - \bar{h}\frac{\partial \rho_s}{\partial t} \\ &+ \phi \rho_g \frac{\partial\left(p/\rho_g\right)}{\partial t} + \left(\frac{p}{\rho_g} - h_g\right)\frac{\partial\left(\phi\rho_g\right)}{\partial t} + \boldsymbol{\sigma} : \boldsymbol{D} + q\end{aligned} \tag{3.73}$$

The gas velocity in the expression is given by Darcy's Law and requires the gas pressure and its gradient. Therefore, (3.73) can be expanded in terms of the two primal fields, temperature and pressure, using (3.67):

$$\begin{aligned}\rho c_p \dot{\theta} = &- \nabla \cdot \left(-\kappa \nabla\theta - h_g \frac{p\mathcal{M}k}{R\theta\mu}\nabla p\right) - \bar{h}\frac{\partial \rho_s}{\partial t} \\ &+ \phi \rho_g \frac{\partial\left(p/\rho_g\right)}{\partial t} + \left(\frac{p}{\rho_g} - h_g\right)\frac{\partial\left(\phi\rho_g\right)}{\partial t} + \boldsymbol{\sigma} : \boldsymbol{D} + q\end{aligned} \tag{3.74}$$

The mass balance equation in terms of the primal fields θ and p can be obtained by substituting (3.66) and (3.64) into (2.30):

$$\dot{\overline{\phi\frac{p\mathcal{M}}{R\theta}}} = \nabla \cdot \left(\frac{p\mathcal{M}k}{R\theta\mu}\nabla p\right) + \dot{\omega}_g \tag{3.75}$$

Using the product and chain rule, (3.75) can be expanded:

$$\begin{aligned}\left(\frac{\phi p}{R\theta}\frac{\partial M}{\partial \theta} - \frac{\phi p M}{R\theta^2} + \frac{pM}{R\theta}\frac{\partial \phi}{\partial \theta}\right)\dot{\theta} + \left(\frac{\phi M}{R\theta} + \frac{pM}{R\theta}\frac{\partial \phi}{\partial p}\right)\dot{p} \\ = \nabla \cdot \left(\phi \frac{pM}{R\theta}\frac{k}{\mu}\nabla p\right) - \frac{\partial \rho_s}{\partial t}\end{aligned} \tag{3.76}$$

In conjunction with the energy balance (3.74), the mass balance (3.76) form a system of partial differential equations for θ and p. The boundary conditions for this system of PDES are:

$$p = \bar{p}\,(\mathbf{x}, t) \quad \text{on} \quad \mathcal{P}_t \tag{3.77}$$

$$\mathbf{q}_{\text{mass}} \cdot \mathbf{n} = \bar{q}_{\text{mass}}\,(\mathbf{x}, t) \quad \text{on} \quad \partial\mathcal{P}_t \tag{3.78}$$

$$\theta = \bar{\theta}\,(\mathbf{x}, t) \quad \text{on} \quad \mathcal{P}_t \tag{3.79}$$

$$\mathbf{q}_{\text{heat}} \cdot \mathbf{n} = \bar{q}_{\text{heat}}\,(\mathbf{x}, t) \quad \text{on} \quad \partial\mathcal{P}_t \tag{3.80}$$

The initial conditions for this system of PDEs are:

$$p = p_0\,(\mathbf{x}, 0) \quad \text{on} \quad \mathcal{P}_t \tag{3.81}$$

$$\theta = \theta_0\,(\mathbf{x}, 0) \quad \text{on} \quad \mathcal{P}_t \tag{3.82}$$

3.7 Pyrolysis Models

In the energy balance equation (3.74) and mass conservation equations (3.76) and (2.28), the term $\frac{\partial \rho_s}{\partial t}$ represents the mass conversion from solid to gas due to pyrolysis. An additional chemical equilibrium or kinetic equation is required to describe this process. A description of two separate pyrolysis models is discussed in this section. The first model is based on the work of Goldstein [47], while the second model is based on the work of Torres-Herrador [26]. Both models are Arhenius-type chemical kinetic models. They differ in the number of chemical species and the number of reactions that are considered. Another difference is that the first model evolves each component density directly, while the second model evolves an extent-of-reaction variable that is used to compute the density of each component.

3.7.1 Goldstein Model

The Goldstein model is a general decomposition model for phenolic resin and nylon materials [47]. This model is a simple model that is used by many existing material response codes for ablative thermal protection systems, including FIAT [48] and CMA [46]. This model was developed by analyzing thermogravimetric (TGA) experiments. In a TGA experiment, a

sample of material is heated from an initial temperature at a constant rate. The TGA data from the experiments in [47] was found to have two peaks in a plot of the rate of change of mass versus temperature. It was inferred that the two peaks correspond to two different decomposing materials. It was also observed that the fiber material does not undergo significant decomposition. For this reason, the solid mass density is modeled as the weighted sum of the resin density and the fiber density:

$$\rho_s = \Gamma\left(\rho_A + \rho_B\right) + \left(1 - \Gamma\right)\rho_C \tag{3.83}$$

where ρ_A and ρ_B represent the density of two resin filler components that decompose during pyrolysis, ρ_C represents the density of a non-decomposing fiber, and Γ is the volume fraction of resin. Since the model assumes that only the two resin components decompose, the rate of change of density for each decomposing component evolves as:

$$\frac{\partial \rho_i}{\partial t} = -B_i e^{-E_i/\theta} \rho_{v,i} \left(\frac{\rho_i - \rho_{c,i}}{\rho_{v,i}}\right)^{\psi_i}, \tag{3.84}$$

where the subscript $i \in \{A, B\}$ indexes the components, B_i is a rate coefficient for component i, and ψ_i is the reaction order for component i.

In order to obtain the chemical source term in the solid mass and gas mass conservation equations, the individual solid density rates are summed to obtain the total density rate change:

$$\frac{\partial \rho_s}{\partial t} = \Gamma\left(\frac{\partial \rho_A}{\partial t} + \frac{\partial \rho_B}{\partial t}\right) = -\dot{\omega}_g \tag{3.85}$$

3.7.2 Torres-Herrador Model

The pyrolysis model for PICA adopted in this section was developed by Torres-Herrador [26]. This model is an Arhenius-based chemical kinetic model for the decomposition of solid material. The model parameters are calibrated to the experiments of Bessire and Minton [25]. In these experiments, 14 significant species were identified in the pyrolysis of PICA using mass spectrometry in a specialized TGA apparatus. With this setup, it is possible to achieve heating rates up to 25 K/s, which is not possible in a conventional TGA experiment. From the heating data, Torres-Herrador proposed to use a kinetic model with 14 species and 6 reactions [26]. Since two of the species (dimethylphenol and trimethylphenol) are not in the NASA-7 database, they were grouped to cresol since they are chemically similar.

The model formulation uses a so-called parallel reaction scheme, where each reaction is assumed to occur independently of the other reactions [28]. The solid phase is composed of different phases, which are defined by their chemical composition. The initial density of the solid before it undergoes pyrolysis can be expressed as:

$$\rho_{s,0} = \sum_{i}^{N_p} \epsilon_{i,0} \rho_{i,0}, \tag{3.86}$$

where N_p is the number of phases, $\epsilon_{i,0}$ is the volume fraction of each phase and $\rho_{i,0}$ is the corresponding mass density.

Each reaction has products that are formed from the decomposition of a single phase. To describe the decomposition of each phase, the model uses an advancement of reaction variable $\chi_{i,j}$ for each reaction j and species i. The evolution of $\chi_{i,j}$ is determined by an Arrhenius rate law of the following form:

$$\frac{\partial \chi_{i,j}}{\partial t} = \mathcal{A}_{i,j}(1-\chi_{i,j})^{n_{i,j}} \exp\left(\frac{-E_{i,j}}{R\theta}\right), \tag{3.87}$$

where $E_{i,j}$ is the activation energy, R is the universal gas constant, $\mathcal{A}_{i,j}$ is a pre-exponential factor with units $[s^{-1}]$, $n_{i,j}$ is the order of the reaction, the subscript i is a solid phase index, and the subscript j is a solid sub-phase index. $\chi_{i,j}$ is initially zero and evolves to one as the reaction progresses. To obtain the remaining total solid mass density at time t, the following equation is used:

$$\rho_s(t) = \left(\rho_{s,0} - \sum_{i}^{N_P}\sum_{j}^{N_{P_i}} \epsilon_{i,0}\rho_{i,0}\chi_{i,j}F_{i,j}\right), \tag{3.88}$$

where each advancement of reaction is scaled by $F_{i,j}$ which is the fraction of density loss for each reaction type to get a total solid mass density lost.

To obtain the chemical source term in the solid and gas mass conservation equations, the original phase densities are scaled and then summed as follows:

$$\frac{\partial \rho_s}{\partial t} = -\sum_{i}^{N_P}\sum_{j}^{N_{P_i}} \epsilon_{i,0}\rho_{i,0}\frac{\partial \chi_{i,j}}{\partial t}F_{i,j} = \dot{\omega}_g \tag{3.89}$$

The Arrhenius model proposed can be used to model species production or elemental production [26]. Here, only the species production model is considered. In order to calibrate the coefficients of (3.87) and (3.88), the authors of [26] used a genetic algorithm to minimize the error between the experimental data and the model predictions. The fit parameters are summarized in Table 3.1 and Table 3.2.

Although the Torres-Herrador does model the evolution of multiple gas species, a single-phase gas model was implemented based on the assumption that the gas generated is well-mixed and homogeneous.

Reaction i	$F_{i,j}$	$\log_{10}\mathcal{A}_{i,j}$	$E_{i,j}$	$n_{i,j}$
1	0.060	6.59	77.6	5.65
2	0.009	6.96	61.3	9.96
3	0.203	6.71	95.1	4.23
4	0.187	6.67	103.0	4.38
5	0.026	6.58	113.9	6.68
6	0.059	6.35	175.2	8.85

Table 3.1: Arrhenius Parameters

Reaction	Chemical	Production Percent
1	H_2O	62%
1	CO	38 %
2	CO_2	69%
2	$C_3H_8O_{,1}$	21 %
2	$C_3H_8O_{,2}$	9 %
3	H_2O	42%
3	CO_2	6%
3	C_6H_5OH	15 %
3	C_7H_8O	34 %
3	C_8H_{10}	3 %
4	CO	67%
4	CH_4	27 %
4	C_6H_6	3 %
4	C_7H_8	4 %
5	H_2	100%
6	H_2	19%
6	CO	81%

Table 3.2: Chemicals produced by the Arrhenius model

3.8 Thermochemical Equilibrium Model for Ablation

Ablation refers to the process of removing mass from a vehicle's surface through thermal, chemical, and mechanical means. Among the mechanical ablation processes are spallation and mechanical erosion caused by the impact of gas and/or liquid particles in the atmosphere, which will not be extensively covered in this thesis. Thermochemical ablation involves sublimation, melting, vaporization, and chemical degradation of the surface and/or interior volume when the structure's surface is exposed to heat fluxes and reactants in the boundary layer gases. The specific chemistry of thermochemical ablation depends on the thermal protection system materials and the composition, density, and state of the surrounding atmosphere. For TPS materials that char like PICA, the boundary layer gases chemically react with the char material at the surface while pyrolysis gases from the interior of the material blow out through surface into the boundary layer. Other materials such as silica, alumina, and zirconia undergo oxidation reactions to form oxides. Then the oxides are blown off the surface by the boundary layer gases. This thesis will mainly focus on charring ablators that undergo pyrolysis.

To properly describe the various processes in thermochemical ablation, a surface mass balance and energy balance model is required. Much of the following discussion follows from a standard description of ablation [45, 46, 85]. The surface energy balance at the surface control volume requires boundary conditions supplied from the material response model and the boundary layer fluid mechanics model. The surface energy balance is:

$$q_{\text{conv}} + q_{\text{rad,in}} - q_{\text{rad,out}} - (\rho V)\, h_w - q_{\text{cond}} + \dot{m}_c h_c + \dot{m}_g h_g = 0, \tag{3.90}$$

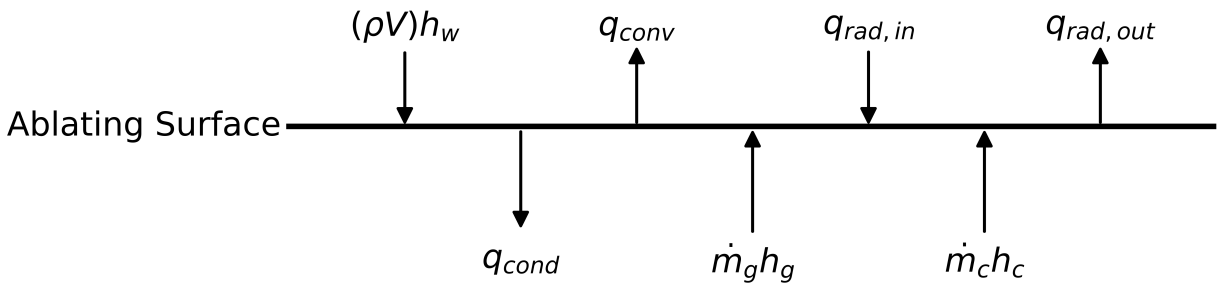

Figure 3.1: Schematic of the terms in the surface energy balance.

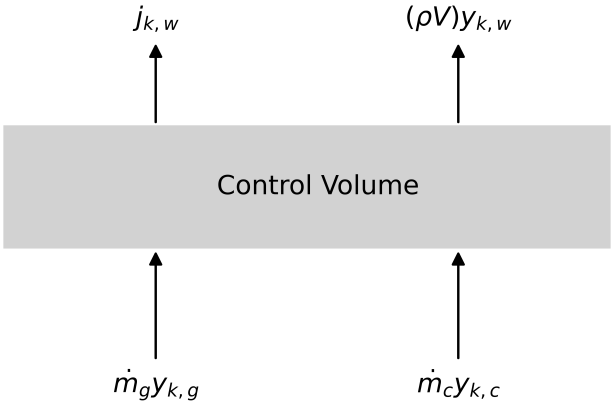

Figure 3.2: Schematic of the terms in the surface mass balance.

where h_w is the wall enthalpy, $\dot{m}_c$ is the char mass flux, $\dot{m}_g$ is the gas mass flux, h_g is the specific gas enthalpy, and h_c is the specific char mass enthalpy.

The convective heat flux in the surface energy balance is:

$$q_{\text{conv}} = (\rho_e u_e C_{H'})\,(h_e - h_w) \tag{3.91}$$

where the boundary layer gas enthalpy h_e, boundary layer gas velocity u_e, and boundary layer gas density ρ_e must be calculated from an external flow solver. The convective heat flux also depends on the h_w which is the wall enthalpy and the modified Stanton number $C_{H'}$ which captures the effect of blowing pyrolysis gases. The modified Stanton number is:

$$C_{H'} = C_H \frac{\ln(1 + 2\lambda B')}{2\lambda B'} \tag{3.92}$$

where B' is a value obtained using the so-called B' table approach in which normalized mass flux rates are tabulated using a thermochemical equilibrium model such as Aerotherm Chemical Equilibrium (ACE) by Aerotherm Corporation [46]. The definition of the B' values

are shown below:

$$B'_g = \frac{\dot{m}_g}{\rho_e u_e C_M}, \quad B'_c = \frac{\dot{m}_c}{\rho_e u_e C_M}, \quad B' = \frac{\dot{m}_{\text{total}}}{\rho_e u_e C_M} \tag{3.93}$$

where $\dot{m}_{\text{total}} = \dot{m}_g + \dot{m}_c$ and C_M is the Stanton mass transfer coefficient. The B' table is utilized to obtain B'_c and h_w as a function of pressure, temperature, and B'_g.

The radiative heat flux away from the surface in the surface energy balance is described by the Stefan-Boltzmann equation below:

$$q_{\text{rad,out}} = \epsilon\sigma\left(\theta_w^4 - \theta_{surr}^4\right) \tag{3.94}$$

where ϵ is the emissivity, σ is the Stefan-Boltzmann parameter, θ_w is the wall temperature, and θ_{surr} is the surrounding temperature.

The mass conservation equation on the surface control volume w of an element k with the relative gas mass fraction y_k depends on the mass transfer flux $j_{k,w}$, the convected mass flux $(\rho V)\, y_{k,w}$, the char mass flux $\dot{m}_c$, and the gas mass flux $\dot{m}_g$:

$$j_{k,w} + (\rho V)\, y_{k,w} = \dot{m}_c y_{k,c} + \dot{m}_g y_{k,g} \tag{3.95}$$

If the Lewis and Prandtl number are one and the diffusion coefficients of all of the reacting species are equal, the equation simplifies to:

$$\rho_e u_e C_H\left(y_{k,w} - y_{k,e}\right) + (\rho V)\, y_{k,w} = \dot{m}_c y_{k,c} + \dot{m}_g y_{k,g} \tag{3.96}$$

where C_H is the Stanton number and $(\rho V) = \dot{m}_c + \dot{m}_g$ [58]. The gas mass flux can be computed from the in-depth governing equations.

To calculate the surface recession rate, the B'_c must be determined by a B prime table lookup for a given temperature, pressure, and gas mass flux. Then the recession rate can be obtained by:

$$\dot{s} = \frac{\dot{m}_c}{\rho_s} = \frac{B'_c \rho_e u_e C_M}{\rho_s} \tag{3.97}$$

The recession rate is integrated in time to obtain the recession amount.

For unity Lewis and Prandtl numbers, the surface energy balance reduces to:

$$\begin{aligned} -\kappa\nabla\theta\cdot\boldsymbol{n} = \rho_e u_e C_H\left(h_r - h_w\right) + \\ \rho_e u_e C_H\left(B'_c h_c + B'_g h_g - B' h_w\right) - \sigma\epsilon\left(\theta_w^4 - \theta_\infty^4\right) \end{aligned} \tag{3.98}$$

A schematic that shows the surface energy balance terms and the surface mass balance terms is shown in Figure 3.1 and Figure 3.2 respectively.

Chapter 4

Computational Modeling Framework

The finite element method is chosen to solve the initial-boundary value problem described by the continuum equations (3.76), (3.74), and (3.14). A variant of the traditional finite element method known as the discontinuous Galerkin (DG) method is adopted. In the context of solid mechanics, this enables the direct and discrete representation of discontinuous phenomena such as fracture in the domain.

This section describes the computational modeling framework including: 1) the resulting Lagrangian/Discontinuous-Galerkin weak formulation of the balance equations, 2) the solution strategy, 3) the mesh recession algorithm employed, and 4) the multi-physics coupling and solution approach.

The computational framework described here is implemented in the finite element research code $\sum$MIT [86]. $\sum$MIT is written in C++, and utilizes Petsc [87] for nonlinear and linear solvers. The code is parallelized using MPI.

4.1 Solid Mechanics Discontinuous-Galerkin Weak Form

The specific discontinuous Galerkin (DG) finite element formulation for non-linear solid mechanics in this thesis is the framework developed by Noels and Radovitzky in [77, 78, 88]. DG methods are a weak formulation that allows discontinuities in the domain interior by restricting the integration by parts to subdomains, which leads to interior boundary integral terms with jump discontinuities. These terms enforce consistency and continuity in a weak manner. Among the advantages of the DG method in the context of solid mechanics is its ability to represent physical discontinuities such as fractures in a natural way [79]. The weak form of the solid mechanics DG problem was derived in detail in the cited references and

can be stated as:

$$\int_{B_{0h}} (\rho_s \ddot{\boldsymbol{\varphi}}_h \cdot \delta\boldsymbol{\varphi}_h + \mathbf{P}_h : \nabla_0 \delta\boldsymbol{\varphi}_h)\, dV + \underbrace{\int_{\partial_I B_{0h}} [\![\delta\boldsymbol{\varphi}_h]\!] \cdot \langle \mathbf{P}_h \rangle \cdot \mathbf{N}^- dS}_{\text{DG consistency term}} + \underbrace{\int_{\partial_I B_{0h}} [\![\boldsymbol{\varphi}_h]\!] : \langle \mathbb{C} \nabla_0 \delta\boldsymbol{\varphi}_h \rangle \cdot \mathbf{N}^- dS}_{\text{DG symmetrization term}} + \underbrace{\int_{\partial_I B_{0h}} [\![\delta\boldsymbol{\varphi}_h]\!] \otimes \mathbf{N}^- : \langle \frac{\beta_s}{h_s} \mathbb{C} \rangle : [\![\boldsymbol{\varphi}_h]\!] \otimes \mathbf{N}^- dS}_{\text{DG stability term}} + = \int_{B_{0h}} \rho_s \mathbf{B} \cdot \delta\boldsymbol{\varphi}_h dV + \int_{\partial_N B_{0h}} \bar{\mathbf{T}} \cdot \delta\boldsymbol{\varphi}_h dS, \quad (4.1)$$

where ρ_0 is the mass density per unit reference volume, $\boldsymbol{\varphi}_h$ is a polynomial approximation of the deformation mapping, $\ddot{\boldsymbol{\varphi}}_h$ is the corresponding approximation of the acceleration field, and $\delta\boldsymbol{\varphi}_h$ is a suitable test function. A constitutive material law relates the discretized deformation gradient tensor $\mathbf{F}_h = \nabla_0 \boldsymbol{\varphi}_h$ to the discretized first Piola-Kirchhoff stress tensor $\mathbf{P}_h$.

In (4.1), the first integral on the left hand side and the two terms on the right hand side are the same classical continuous Galerkin (CG) formulation of the solid mechanics problem. The last two integral terms on the left hand side of (4.1) represent the interior element boundary integrals which result from the weak enforcement of inter-element continuity. These integrals ensure consistency and stability of the solution in the presence of discontinuous displacement fields in the uncracked continuum [77]. In these expressions, $[\![\bullet]\!] = [\bullet^+ - \bullet^-]$ and $\langle \bullet \rangle = \frac{1}{2}[\bullet^+ + \bullet^-]$ are the jump and average operators, $\mathbf{N}^-$ is the outward unit reference normal to the minus side of an interface element (see Figure 4.1), β_s is a stability parameter, h_s is a characteristic element size, and $\mathbb{C} = \frac{\partial \mathbf{P}}{\partial \mathbf{F}}$ are the Lagrangian tangent moduli.

The introduction of interface elements in the DG method is illustrated in Figure 4.1. Two 10 node quadratic tetrahedral elements Ω_0^{e+} and Ω_0^{e-} are shown. The nodes in the figure are located on the vertices of the tetrahedron and also on the midpoint of the edges. Between the two quadratic tetrahedral elements, a 12 node interface element is introduced. This interface element is used to enforce the continuity of the displacement field across the interface when desired through the use of the DG consistency term.

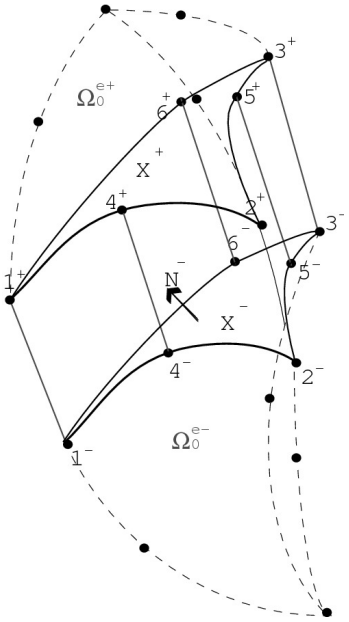

Figure 4.1: Description of a 12-node interface element introduced between two 10-node quadratic tetrahedra Ω_0^{e+} and Ω_0^{e-}.

4.2 Mass and Heat Transfer Discontinuous-Galerkin Weak Form

The DG weak forms corresponding to the heat transfer and mass transport problems are obtained following a standard procedure, i.e. by multiplying the strong-form equations by discontinuous test functions $\delta\theta$ or δp, respectively, integrating over each element in a discontinuous discretization, and integrating by parts:

$$\begin{aligned}\int_B (q - c_p\dot{\theta})\delta\theta + \mathbf{q}_R \cdot \nabla_0\delta\theta dV - \int_{\partial_N} \bar{q}\delta\theta dS_2 \\ = \int_{\partial_I B} \underbrace{\left(\llbracket\delta\theta\rrbracket\langle\mathbf{q}_R\rangle \cdot \mathbf{n}_R^-\right)}_{\text{DG Consistency Term}} dS + \int_{\partial_I B} \underbrace{\llbracket\theta\rrbracket\langle\frac{\partial\mathbf{q}_R}{\partial\nabla_0\theta} \cdot \nabla_0\delta\theta\rangle \cdot \mathbf{n}_R^-}_{\text{DG Symmetrization Term}} dS \\ + \int_{\partial_I B} \underbrace{\left(\llbracket\delta\theta\rrbracket\langle-\frac{\partial\mathbf{q}_R}{\partial\nabla_0\theta}\frac{\beta_{\text{therm}}}{h}\rangle\llbracket\theta\rrbracket\right)}_{\text{DG Stabilization Term}} dS \quad (4.2)\end{aligned}$$

$$\int_B (\dot{\omega_g} - c_{\text{mass}}\dot{p})\delta p + \mathbf{q}_{\text{mass}} \cdot \nabla \delta p \, dV - \int_{\partial_N} \bar{q}_{\text{mass}} \delta p \, dS_2$$
$$= \int_{\partial_I B} \underbrace{\left([\![\delta p]\!] \langle \mathbf{q}_{\text{mass}} \rangle \cdot \mathbf{n}^- \right)}_{\text{DG Consistency Term}} dS + \int_{\partial_I B} \underbrace{[\![p]\!] \langle \frac{\partial \mathbf{q}_{\text{mass}}}{\partial \nabla p} \cdot \nabla \delta p \rangle \cdot \mathbf{n}_R^-}_{\text{DG Symmetrization Term}} dS$$
$$+ \int_{\partial_I B} \underbrace{\left([\![\delta p]\!] \langle - \frac{\partial \mathbf{q}_{\text{mass}}}{\partial \nabla p} \frac{\beta_{\text{mass}}}{h} \rangle [\![p]\!] \right)}_{\text{DG Stabilization Term}} dS, \quad (4.3)$$

where β_{therm} and β_{mass} are the stabilization parameters for the thermal and mass transfer problems, and h is the characteristic length scale of the mesh. The stabilization parameters are chosen independently for each problem. Analogously to the solid mechanics weak form (4.1), the weak forms (4.2) and (4.3) contain the standard finite element integrals along with the DG consistency, symmetrization, and stabilization terms.

4.3 Mesh Recession Algorithm

In Section (4.3), a procedure of obtaining the recession amount from thermochemical ablation is discussed. From the solid mechanics perspective, the ablation process is akin to other surface erosion processes such as wear that constitutes a recession of the material surface in the reference configuration [89]. Numerically, this requires a *mesh recession algorithm* that: 1) moves the nodes on the boundary in the direction normal to the surface and at a rate that is specified by the physics of the problem, 2) ensures satisfaction of mass, momentum and energy balance after mass removal, and 3) maintains the quality of the mesh elements close to the surface as they get eroded away.

Several algorithmic procedures for mesh recession have been proposed, [63, 74–76, 89–91]. They mainly differ in the approach to handle mesh distortion due to surface recession. In general, they utilize a class of mesh optimization algorithms known as *mesh smoothing*, where the position of the interior nodes of the mesh are modified to maximize a global metric of mesh quality [92–94]. In particular, the following specific methods have been used to achieve this objective: 1) solving a linear elasticity equilibrium problem with a fictitious isotropic elasticity tensor where a displacement boundary condition is applied to the original mesh that is equivalent to the mesh recession amount [95]. The solution to this problem returns a displacement field that is used to update the interior node positions in the solid body [63, 75, 76]; 2) using a combination of fictitious linear springs in an equilibrium system of equations to update the interior node positions [90]; 3) using interpolation functions with compact support such as radial basis functions that does not require a solution to a partial differential equation or solving a dense system of linear equations or tracking connectivity of nodes [74, 91].

The mesh smoothing approaches described changes the material coordinates of each node. In an Arbitrary Lagrangian-Eulerian or Eulerian approach, this means that grid fluxes need to be introduced to properly evolve and attribute material properties to each node. In a finite element approach, the shape functions need to be recomputed.

In this work, a different strategy for moving the boundary nodes located at the exposed surface is employed in the adopted approach to mesh recession. Instead of manipulating the boundary nodes in spatial coordinates, they are relocated within the reference configuration. This methodology is akin to the approach used by Molinari for modeling wear in sliding metals due to friction [89]. After relocating the boundary nodes, the surface elements in the reference configuration take on a different shape compared to the original mesh.

To maintain a proper interpolation mapping within the elements in material coordinates, the shape functions are recomputed using the new coordinates in the reference configuration. Additionally, internal variables and primal fields attributed to the original quadrature and nodal points must be interpolated to the new mesh. This ensures that values associated with material points no longer present in the updated reference configuration are naturally eliminated. As an example, consider temperature. The temperature related to the removed material no longer exists in the new domain, resulting in the removal of the associated thermal energy as expected. The same principle applies to stresses, strains, and other important variables, including internal variables such as solid density, extent of reactions, or even damage variables if used in the present framework.

The mesh recession algorithm described above is effective for first-order elements but requires modifications for higher-order elements. To accommodate higher-order elements, the recession is initially applied to the nodes that coincide with the mesh vertices. Subsequently, the positions of the non-vertex nodes are recalculated based on the new simplex geometry.

An additional critical consideration in this mesh recession approach is the alteration in the reference configuration edge or face normals due to the change in vertex node positions. The DG method relies on the reference configuration normals to enforce compatibility. In order to account for this change, the reference configuration normals are recomputed after the mesh recession algorithm is applied using the new vertex node positions.

Internal variables and primal fields attributed to the original quadrature and nodal points must be interpolated to the new mesh. The interpolation is accomplished by using the old mesh finite element shape functions to interpolate the values from the old mesh to the new mesh. This means there is no need to compute grid fluxes related to a moving mesh which simplifies the implementation of the algorithm.

When the mesh has undergone a significant recession, causing the boundary element to deform severely, a mesh smoothing process can be applied by solving a static linear elasticity problem with a fictitious isotropic elasticity tensor. This approach involves partitioning the boundary into three sets: one allowed to recede, one allowed to relax, and one fixed.

For the boundary set permitted to recede, a displacement boundary condition is imposed with the physical recession values. Boundaries adjacent to the receding boundary are allowed to relax by using rollers, enabling surface movement along the boundary without inward motion. Conversely, boundaries not adjacent to receding boundaries are fixed to prevent motion.

Upon solving the static linear elasticity problem, the resulting displacement field is added to the current reference configuration, yielding a new reference configuration. This method

maintains the connectivity table of elements and nodes while preserving mesh quality. Following the mesh smoothing, the shape functions of all elements must be recomputed instead of only the surface elements. This is necessary since the entire mesh undergoes changes due to the mesh smoothing algorithm. Additionally, the entire domain requires interpolation, as the material coordinates of all nodes have changed.

4.4 Quasi-Static Solution Approach for Solid Mechanics

The following analysis is restricted to quasi-static non-linear solid mechanics problems, which enables the dynamic relaxation (DR) numerical method [96–98]. Dynamic relaxation is an iterative method that returns the steady-state solution to the dynamic problem:

$$\rho\ddot{\mathbf{u}} + c\rho\dot{\mathbf{u}} = \mathbf{r}\left(\mathbf{u}\right), \tag{4.4}$$

where $\mathbf{u}$ is the displacement field, c is a damping coefficient that is greater than zero, ρ is an artificial density, and $\mathbf{r}$ is the residual force that is zero when $\mathbf{u}$ is the static solution. The damping coefficient plays the role of adding artificial viscosity to the system to dissipate energy in the system. While the initial and boundary conditions generate stress waves when initially imposed, successive DR iterations drive the acceleration and velocity to zero through this damping.

The dynamic process is solved using explicit time integration with the Explicit Newmark method and mass lumping [99]. The dynamic response for the spatially discretized system of (4.4) is given by:

$$\mathbf{M}\mathbf{a} + c\mathbf{M}\mathbf{v} = \mathbf{r}\left(\mathbf{u}\right), \tag{4.5}$$

where $\mathbf{M}$ is the diagonal mass matrix from mass lumping, $\mathbf{a}$ is the acceleration field, and $\mathbf{v}$ is the velocity field. The explicit Newmark procedure uses a predictor corrector approach. The Newmark predictors are:

$$\mathbf{u}_{n+1}^{(0)} = \mathbf{u}_n + \Delta t\mathbf{v}_n + \Delta t^2\left(\frac{1}{2} - \beta\right)\mathbf{a}_n \tag{4.6}$$

$$\mathbf{v}_{n+1}^{p} = \mathbf{v}_n + \Delta t\left(1 - \gamma\right)\mathbf{a}_n \tag{4.7}$$

The step-by-step procedure for the explicit Newmark method is as follows:

1. Start with values for the displacement field $\mathbf{u}^0$, velocity field $\mathbf{v}^0$, and acceleration field $\mathbf{a}^0$ from the previous time steps.
2. Compute the Newmark predictors.
3. Compute the residual force $\mathbf{r}\left(\mathbf{u}_{n+1}\right) = F_{n+1}^{\text{ext}} - F^{\text{int}}\left(\mathbf{u}_{n+1}\right)$.
4. Compute the acceleration field $\mathbf{a}_{n+1} = \mathbf{M}^{-1}\mathbf{r}\left(\mathbf{u}_{n+1}\right)$.
5. Correct the velocity field $\mathbf{v}_{n+1} = \mathbf{v}_{n+1}^{(p)} + \gamma\Delta t\mathbf{a}_{n+1}^{(0)}$.

The dynamic relaxation method procedure is:

1. Initialize the solver with a damping coefficient, time step, and mass matrix. Set the absolute and relative tolerances for the residual force and the maximum number of iterations.

2. Apply the boundary conditions for the problem.

3. Perform one step of the explicit Newmark method to compute the Newmark predictors.

4. Check for convergence of the residual force using the absolute and relative tolerances. If the residual force is below the tolerance, then the solution has converged and the algorithm terminates. If the number of iterations exceeds the maximum number of iterations, then the algorithm terminates without being converged. Otherwise, continue to the next step.

5. Apply the corrector step to update the solution and go to the next iteration.

4.5 Multi-Physics Coupling and Solution Approach

The primal fields $\mathbf{u}, \theta$ and p are governed by the coupled system of PDEs (3.76), (3.74), and (3.14). A so-called staggered approach is employed to numerically solve this system. Various modules are developed, each tasked with addressing a subset of the governing equations. These components are solved sequentially, and the solution is passed from one module to the next as necessary. In this paradigm, the mechanics BVP (3.14) is solved for the fields $u, \boldsymbol{\sigma}$, and $\boldsymbol{\epsilon}$ with θ and p fixed. The DG finite element method for solid mechanics (Section 4.1) with the dynamic relaxation method (Section 4.4) is used to solve this system. In turn, the mass and heat transfer equations, (3.76) and (3.74), are solved monolithically for θ and p with $\mathbf{u}, \boldsymbol{\sigma}$, and $\boldsymbol{\epsilon}$ held fixed. The DG finite element method for heat and mass transfer (Section 4.2) was solved using a Backward Euler time integration scheme. The revised solid density field (ρ_s) is also returned as an internal variable. Then the temperature obtained is input into a B' table to obtain the recession rate. Finally, the mesh is adjusted according to this rate and the time step is incremented based on the procedure in Section 4.3. A schematic of this coupling procedure is given in (4.2).

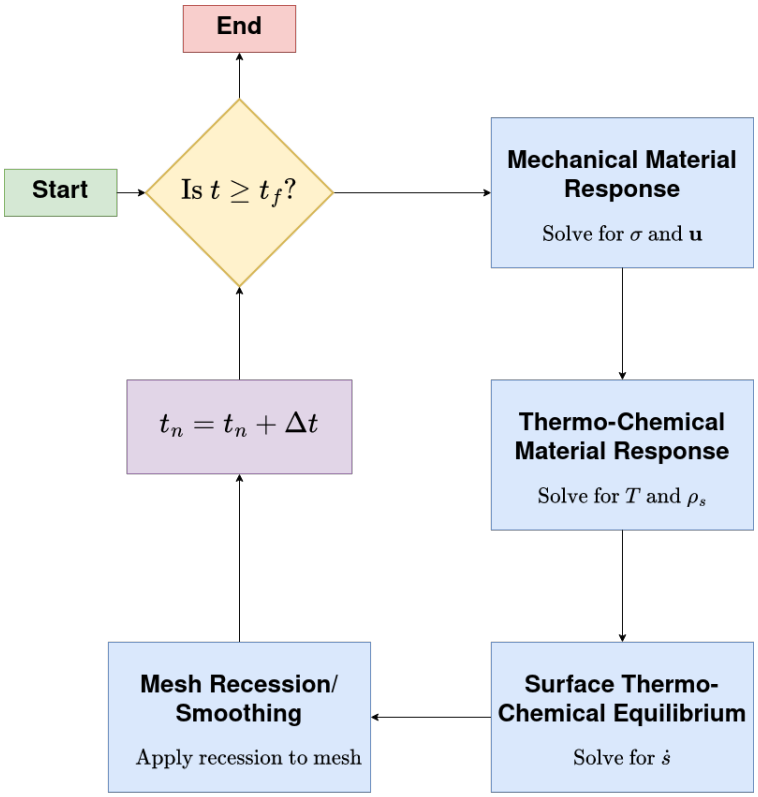

Figure 4.2: Staggered solution strategy for one time step of the multi-physics problem.

Chapter 5

Numerical Examples

In this section, several examples are presented that demonstrate the thermo-chemo-mechanical simulation framework for ablative thermal protection systems. First, the Goldstein decomposition model [47] is demonstrated. Then, the implementation of the Torres-Herrador pyrolysis model for PICA in $\sum$MIT is verified against published a solution [26]. Next, the numerical solution of the energy balance equation (3.16) is verified for different initial and boundary conditions using analytical solutions. Also, $\sum$MIT is compared against other ablative TPS material response codes using two examples based on the Ablation Workshop Test Cases 1 [64] and 2.1 [65]. These test cases contain data based on a fictitious material known as Theoretical Ablative Composite for Open Testing (TACOT) [61]. The properties of TACOT are based on currently-used low-density ablative materials and are summarized in Appendix A. The next examples demonstrate that the temperature and displacement fields are properly preserved by the mesh recession and interpolation procedures. The last example is a simulation of an arc-jet test of PICA to demonstrate the ability of the framework to model experiments. In particular, it can resolve the time-dependent thermal and mechanical response of the PICA sample subject to ablation, pyrolysis, mechanical deformation, heat transfer, and their couplings.

5.1 Example of the Goldstein Decomposition Model

The Goldstein pyrolysis model [47] was implemented in $\sum$MIT to demonstrate a 0-D simulation of a TGA experiment. Recall that the material is modeled as a resin composed of two decomposing components and a non-decomposing fiber. Material decomposition begins when the activation temperature of one of the components is reached (Section 3.7.1). The total decomposition rate is the sum of the decomposition rates of all components (3.85). The Goldstein pyrolysis model returns the decomposition rate and solid mass density of each component.

In this example, the specimen was heated at a rate of 10 K/min from an initial temperature of 300 K. The TACOT material decomposition properties were used as shown in

Table 5.1. Figure 5.1 shows the decomposition rate as a function of the temperature. Each reaction mechanism is activated then peaks at, a different temperature. The decomposition curve changes with the heating rate. The corresponding solid mass density as a function of the temperature is shown in Figure 5.2. The solid mass density does not change until the temperature reaches the activation temperature of the first reaction. Then the density decreases corresponding to the decomposition rate.

Reaction	$\rho_{i,v}$	$\rho_{i,c}$	B_i	E_i/R	ψ	T_{reac}
	(kg/m^3)	(kg/m^3)	(1/s)	(K)	(—)	(K)
A	300	0	8556	1.20×10^4	3	333.3
B	900	600	20440	4.48×10^9	3	555.6
C	1600	1600	0	0.00	0	555.6

Table 5.1: Parameters used in the TACOT pyrolysis model.

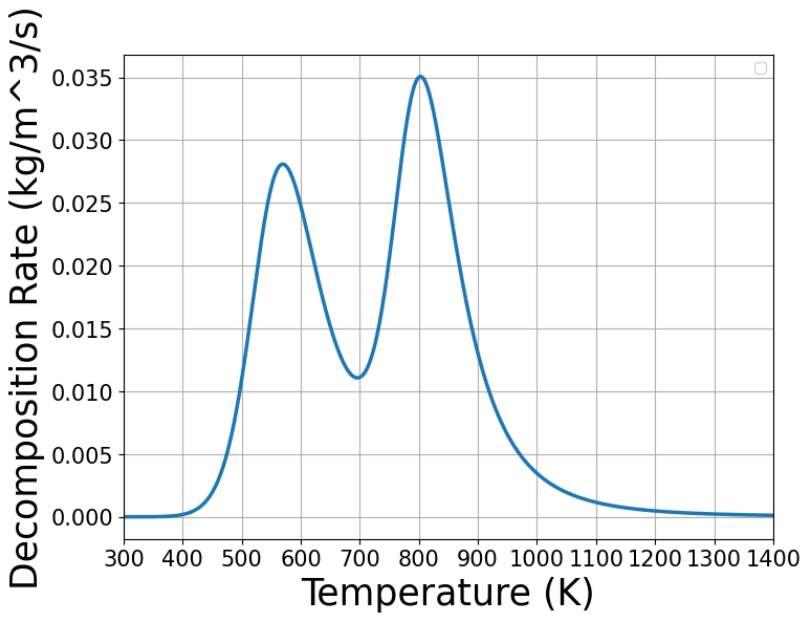

Figure 5.1: Decomposition rate vs temperature for TACOT at a heating rate of 10 K/min.

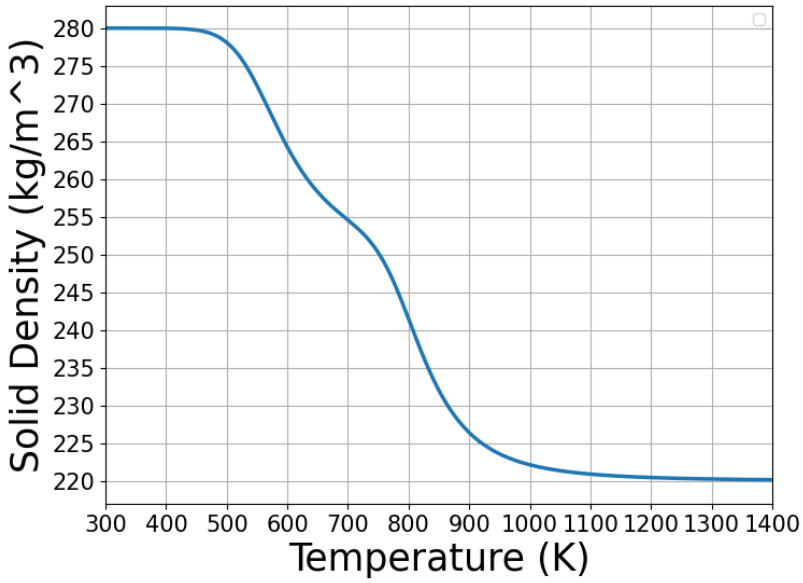

Figure 5.2: Solid mass density vs temperature for TACOT at a heating rate of 10 K/min.

5.2 Verification of the Torres-Herrador Pyrolysis Model

The Torres-Herrador model was implemented in ∑MIT. To verify it, a 0-D simulation of a TGA experiment in ∑MIT using this model was compared to results from PATO with its own implementation of the model [26]. Specifically, the species-based (rather than the elemental-based) model was used. The fractional mass loss rate for each chemical species is shown in Figures 5.3, 5.4, and 5.5. The individual species are grouped into three categories: alcohols, aromatics, and permanent. The solid lines represent the results from ∑MIT, whereas the dashed lines represent the results from PATO. There are some discrepancies around the peak decomposition rate of some of the species due to the different numerical methods used in each code. In particular, the largest differences are seen in the decomposition of the aromatics, where ∑MIT tends to overpredict the decomposition rate slightly. Overall, there seems to be good agreement, however, between the two codes, which verifies the implementation of the Torres-Herrador model in ∑MIT.

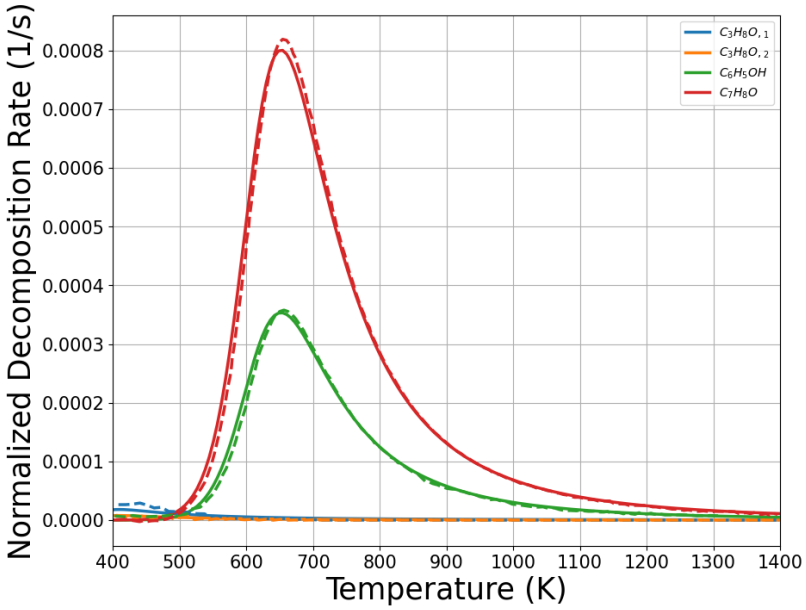

Figure 5.3: Fractional mass loss vs temperature for alcohols using the Torres-Herrador at a heating rate of 6.1 K/s.

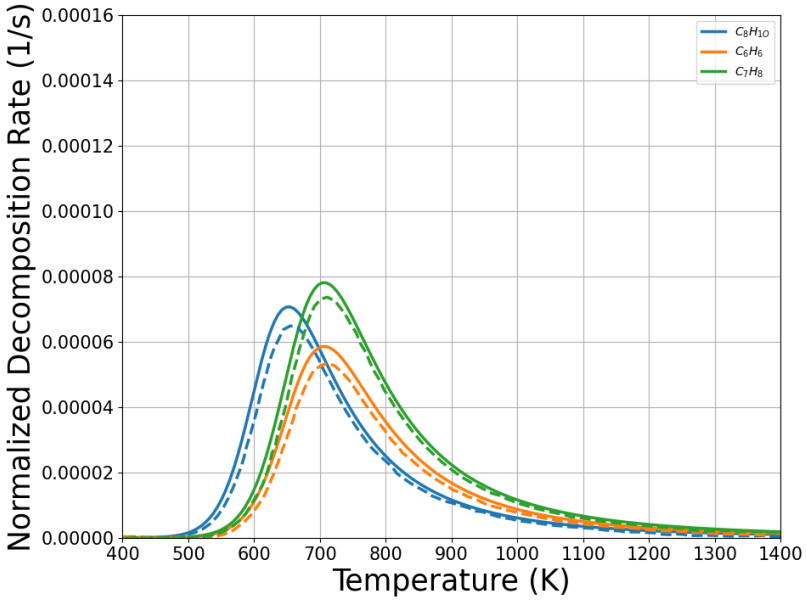

Figure 5.4: Fractional mass loss vs temperature for aromatics using the Torres-Herrador at a heating rate of 6.1 K/s.

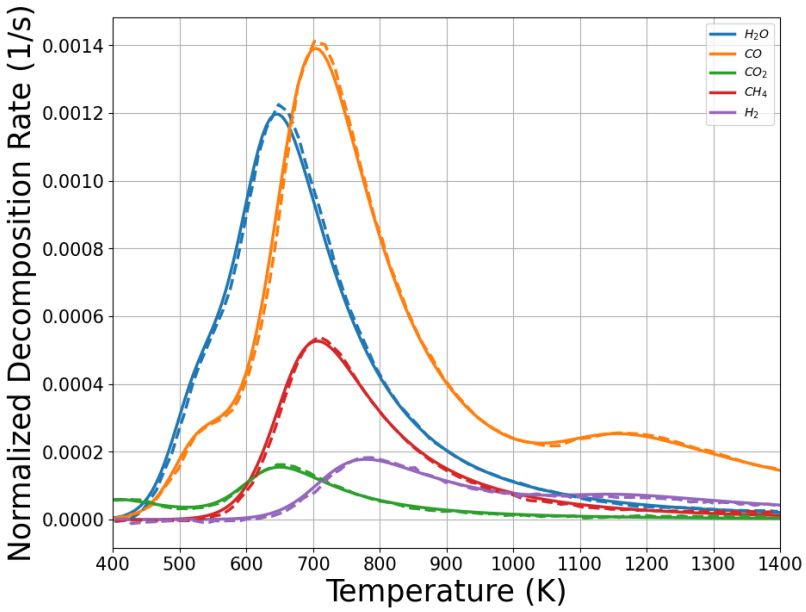

Figure 5.5: Fractional mass loss vs temperature for permanent using the Torres-Herrador at a heating rate of 6.1 K/s.

5.3 Semi-infinite solid with a constant initial temperature, zero surface temperature, and constant thermophysical properties

This verification case is a comparison of the solution of the energy equation for a semi-infinite solid domain with constant mass density, specific heat capacity, and thermal conductivity. The domain has an initial temperature of θ_0 and prescribed a surface temperature of zero. Mathematically, the initial boundary value problem is:

$$\frac{1}{\alpha}\frac{\partial \theta}{\partial t} = \frac{\partial^2 \theta}{\partial x^2} \tag{5.1}$$

$$\theta\left(x, 0\right) = \theta_0 \tag{5.2}$$

$$\theta\left(0, t\right) = 0 \tag{5.3}$$

The analytical solution, found in [100], is given by:

$$\theta\left(x, t\right) = \theta_0 \operatorname{erf}\left(\frac{x}{2\sqrt{\alpha t}}\right), \tag{5.4}$$

where α is the thermal diffusivity:

$$\alpha = \frac{\kappa}{\rho C_p} \tag{5.5}$$

The analytical solution was evaluated using the material properties shown in Table 5.2 to compare to the solution from $\sum$MIT.

To run the verification case in $\sum$MIT, a 5-cm by 1-cm 2D domain was created with an initial temperature of 298 K. A boundary condition of a fixed temperature of 0 K was assigned to one side of the rectangle. The analytical solution was imposed on the remaining boundaries.

The simulation was run for a duration of 1000 seconds. A comparison of $\sum$MIT to the analytical solution is shown in Figure 5.6. The temperatures display good agreement at various depths within the material between $\sum$MIT and the analytical solution. This verifies that the current implementation of $\sum$MIT correctly solves the energy equation for a linear heat conduction problem.

Parameter	Value	Units
α	10	m^2/s
κ	1000	W/m^2
C_p	100	J/kg/K
ρ	1000	kg/m^3

Table 5.2: Semi-infinite Solid Verification Case Parameters

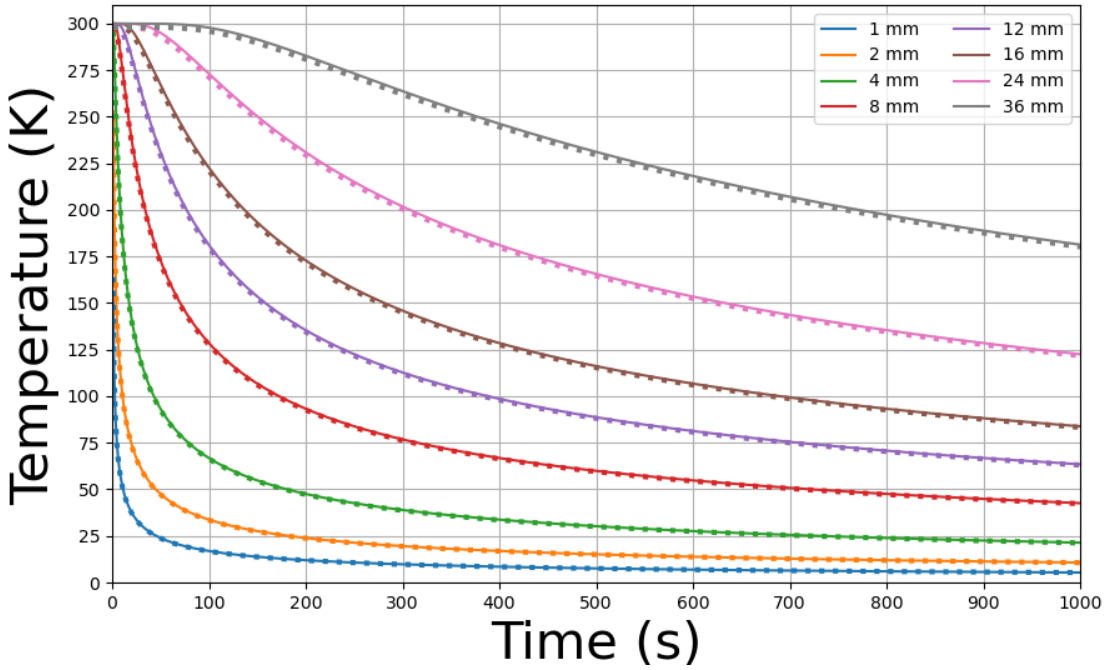

Figure 5.6: Comparison of solution from ∑MIT (in dots) vs the analytical solution (in solid lines) for a semi-infinite solid with constant properties, an initial temperature of 300 K, and a surface temperature of 0 K.

5.4 Convection Boundary Condition for a Slab

The next verification case is a comparison of the solution of the energy equation for a slab of length l with a surface subjected to a convective boundary condition. The initial boundary value problem is:

$$\rho C_p \frac{\partial \theta}{\partial t} = \kappa \frac{\partial^2 \theta}{\partial x^2} \tag{5.6}$$

with the initial condition:

$$\theta\left(x, 0\right) = \theta_0 \tag{5.7}$$

and the convective boundary condition:

$$-\kappa \frac{\partial \theta}{\partial x}\left(0, t\right) = C_h\left(\theta\left(0, t\right) - \theta_\infty\right), \tag{5.8}$$

where C_h is the convective heat transfer coefficient, and θ_∞ is the temperature of the fluid. The analytical solution to the temperature on the surface of the slab is given by:

$$\theta\left(x, t\right) = \theta_\infty + \left(\theta_0 - \theta_\infty\right) \sum_{N=1}^{\infty} \frac{2L}{L\left(L+1\right) + \alpha_n^2} e^{-\alpha_n^2 \Theta}, \tag{5.9}$$

where $\Theta = \frac{\kappa t}{\rho C_p l^2}$, $L = \frac{C_h l}{\kappa}$, and α_n is the nth root of $\alpha \tan \alpha = L$.

The parameters in Table 5.3 were used for the comparison between ∑MIT and the analytical solution. Figure 5.7 shows good agreement between the analytical solution and the ∑MIT solution for the temperature field. This verifies that the solution to the energy equation with a convective boundary condition is properly solved in ∑MIT.

Table 5.3: Parameters for Convective Boundary Condition Verification Case

Parameter	Value	Units
κ	0.623	W/m^2
C_p	419	J/kg/K
ρ	160.18434	kg/m^3
l	0.0508	m
T_0	556	K
T_∞	278	K
C_h	20.4417	J/K

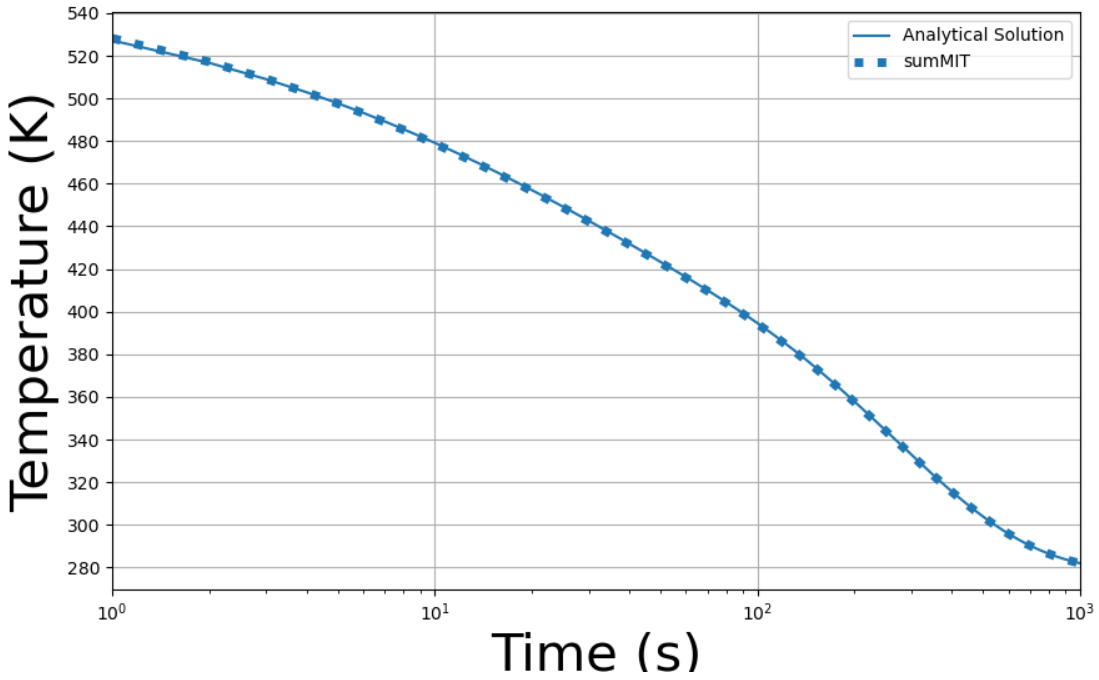

Figure 5.7: Temperature at the surface of a slab exposed to a convective boundary condition from the analytical solution and ∑MIT.

5.5 Radiation Boundary Condition

This verification case is a comparison of the solution to the energy equation for a slab with constant properties where one side is assigned a radiative cooling boundary condition described by the Stefan Boltzmann Law:

$$-\kappa \frac{\partial \theta}{\partial t} = \sigma \epsilon \left(\theta_w^4 - \theta_\infty^4 \right), \tag{5.10}$$

where σ is the Stefan-Boltzmann constant, ϵ is the emissivity, θ_w is the temperature of the wall, and θ_∞ is the environment temperature. The solution from $\sum$MIT is compared to the numerical solution from FIAT and shown in Fig. 5.8 at different depths within the slab. There is good agreement between the two codes, which verifies that $\sum$MIT can properly model the radiation boundary condition.

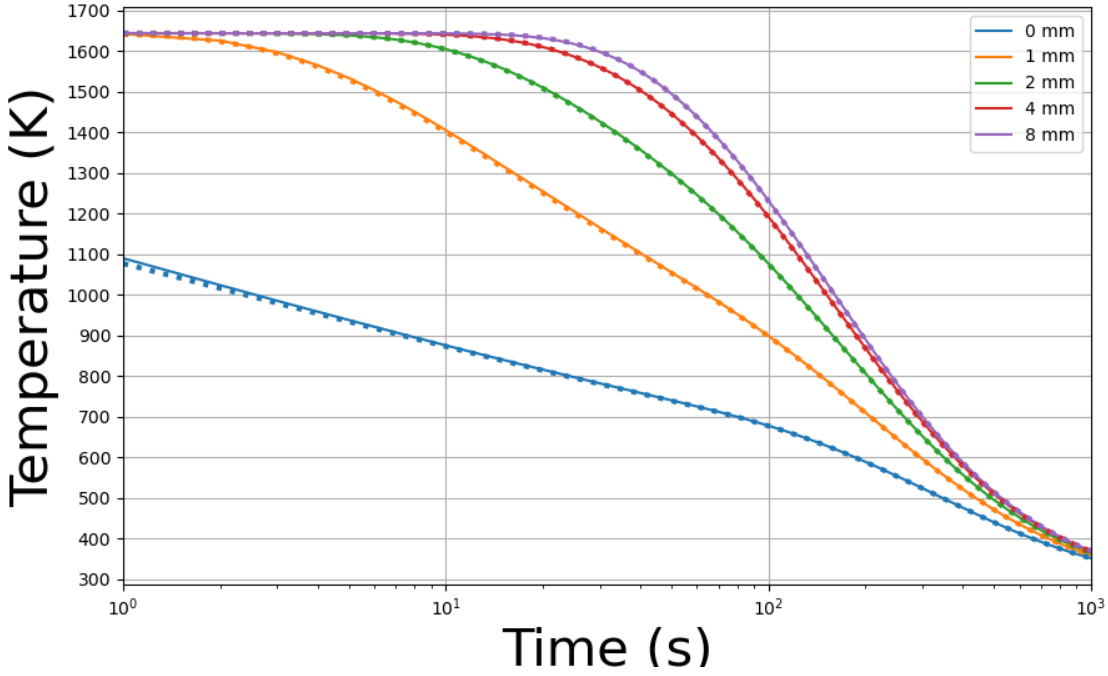

Figure 5.8: Comparison of FIAT (in dots) vs $\sum$MIT (in solid lines) temperature solution at various depths in the material for the radiation boundary condition.

5.6 Ablation Workshop Test Case 1

In this section, the Ablation Workshop Test Case 1 [64] is used to compare $\sum$MIT to FIAT [48] for a simple heat transfer problem with in-depth decomposition. The domain is

Table 5.4: Ablation Workshop Temperature Boundary Condition

Time	Temperature	Pressure
(sec)	(K)	(atm)
0	300	1
0.1	1644	1
60	1644	1
60.1	300	1
120	300	1

a 5-cm long 1D sample of TACOT. In FIAT, a Dirichlet temperature boundary condition is assigned at one end of the sample as shown in Figure 5.9 with values from Table 5.4. The table values are utilized to perform linear interpolation of the temperature over time. A fixed pressure boundary value of 101,325 Pa is also applied on the same side. The temperature and mass density are monitored over time at the surface, as well as at specific points situated 1 mm, 2 mm, 4 mm, 8 mm, 16 mm, and 24 mm away from the applied Dirichlet boundary conditions, respectively, as shown in colors in Figure 5.9. Adiabatic and impermeable boundary conditions are imposed on the other end.

In $\sum$MIT, a 5-cm by 1-cm rectangle was modeled. Dirichlet boundary conditions were applied along the width at the right edge of the rectangle. Meanwhile, the remaining edges were assigned impermeable and adiabatic boundary conditions. Notably, ablation and mechanical effects were excluded from this simulation, as the primary focus was to verify the temperature and chemical material response.

Figures 5.10 and 5.11 show a comparison of the temperature and and solid mass density, respectively, between the two codes. The lines represent the results from FIAT, while the dots represent our simulation results. The different colors represent different locations in the domain, which correspond to the locations shown in Figure 5.9.

The temperature and density show good agreement between the two codes. Some small disparities are noticeable near the sample's surface, likely stemming from density interpolation in $\sum$MIT using values from quadrature points. Indeed, FIAT and $\sum$MIT differ in how they handle mass flux; $\sum$MIT applies Darcy's law, whereas FIAT employs a simplified transport model (1.2) described in Section 1.3. Another notable difference is that FIAT is a 1D code, whereas $\sum$MIT is a 2D/3D code. Furthermore, FIAT utilizes a finite volume scheme, while $\sum$MIT utilizes a finite element scheme.

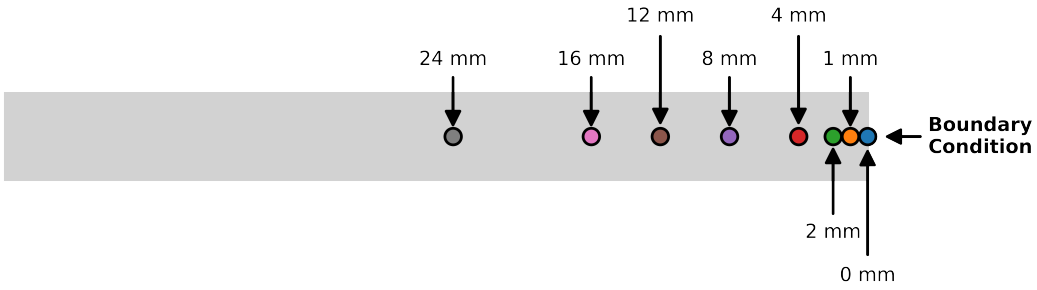

Figure 5.9: Locations in the domain of the Ablation Workshop 1 where temperature and density are tracked as a function of time.

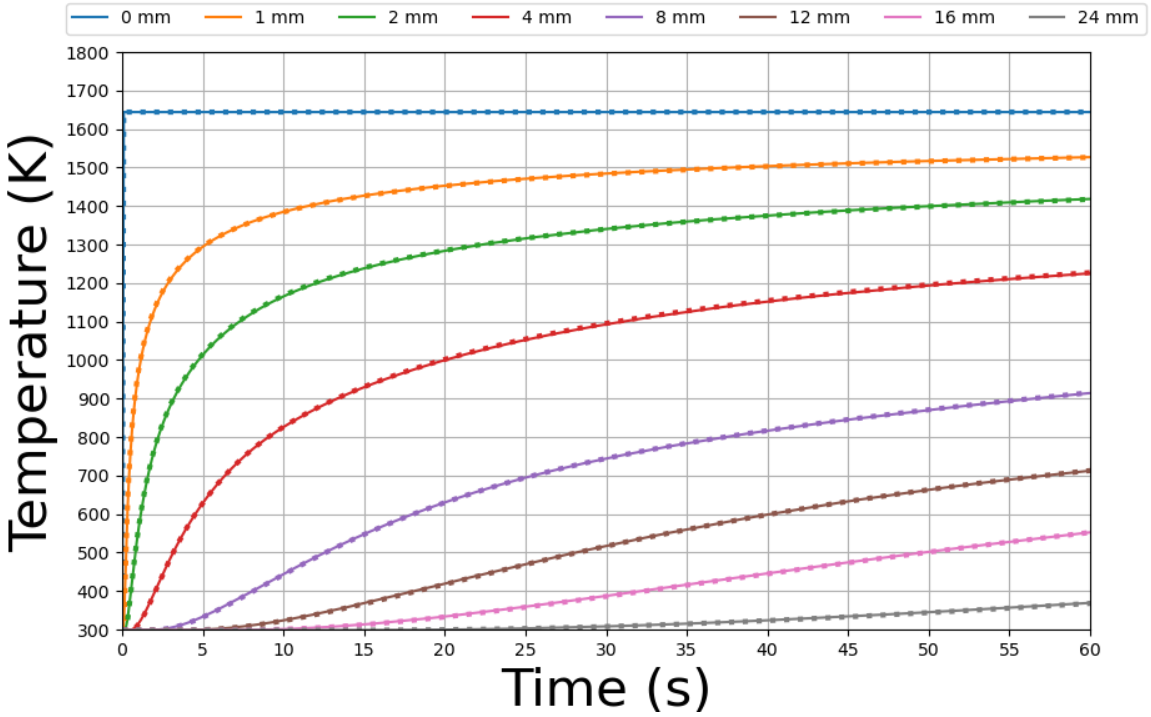

Figure 5.10: Comparison of our result (dotted lines) versus FIAT (solid lines) for temperature as a function of time for the Ablation Workshop test case 1.

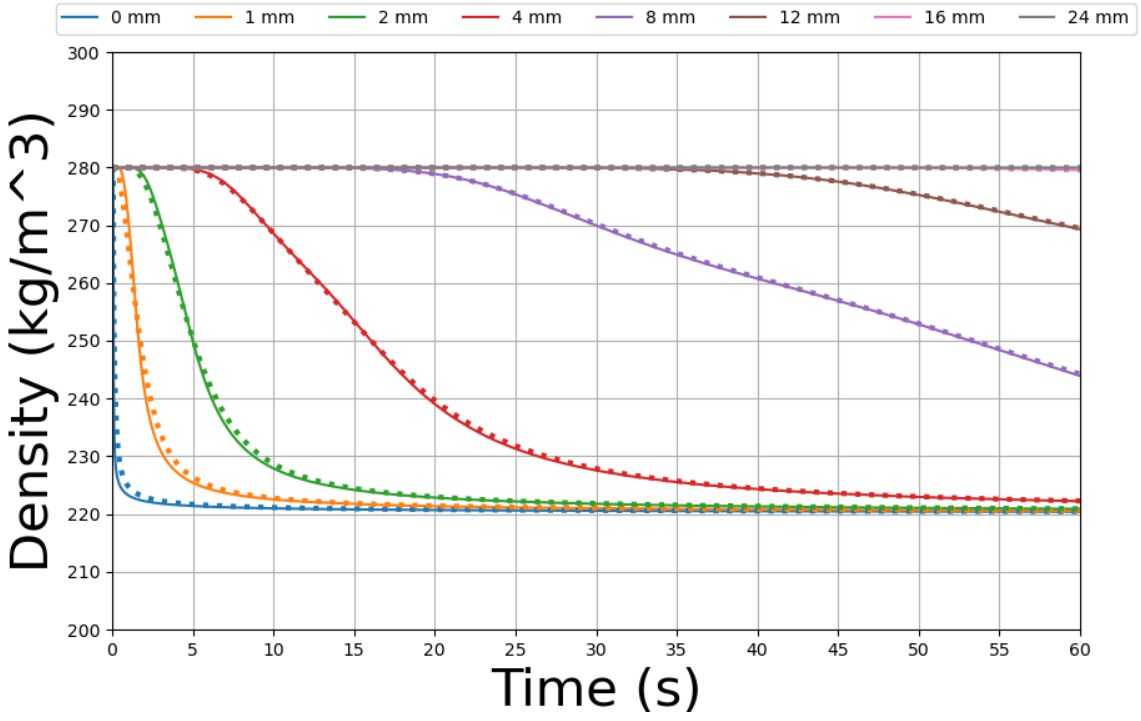

Figure 5.11: Comparison of our result (dotted lines) versus FIAT (solid lines) for solid mass density as a function of time for the Ablation Workshop test case 1.

5.7 Ablation Workshop Test Case 2.1

For this verification example, the Ablation Workshop Test Case 2.1 [64] is used to test the implementation of the surface energy balance (3.98) without recession by comparing $\sum$MIT to PATO [28]. This test case is similar to the Ablation Workshop Test Case 1, but it introduces a convective boundary condition on the surface of the sample instead of a fixed surface temperature boundary condition. The domain for this test case is the same as for the Ablation Workshop Test Case 1, which is a 5-cm long specimen of the TACOT material. In addition to testing the thermal response of convective heating, this test case also tests pure radiative cooling. The values of the convection coefficient and recovery enthalpy are provided in Table 5.5. Blowing correction correlations are also used with the convection coefficient to account for the effect of the boundary layer, with a blowing factor of 0.5. For re-radiation effects, $\theta_\infty = 300$K is used. Also, unity Prandtl and Lewis numbers are assumed for the boundary layer (see Section 3.8).

An important addition is the B' table thermochemical equilibrium model at the surface. All B'_c values were set to zero since recession was not included in this test case. This was done to isolate the surface energy balance boundary condition from mesh motion issues due to recession. Since the boundary was kept at atmospheric pressure, only B' values corresponding to atmospheric pressure were used. The wall enthalpy, h_w, was obtained using the surface temperature, pressure, and mass flux out of the surface. The mass flux was obtained at the surface from Darcy's Law using the solution to the conservation equations.

The same 2D domain as the $\sum$MIT case for the Ablation Workshop Test Case 1 was used. The difference was that a convective boundary condition was assigned on the right edge of the domain instead of a fixed temperature. This convective boundary condition was applied by prescribing a heat flux that was calculated explicitly using the energy balance model (3.98). It includes the contributions from the diffusive, convective, and radiative heat fluxes. The remaining edges were assigned adiabatic and impermeable boundary conditions, as in the first test case. Heating was applied for 60 seconds, followed by 60 seconds of radiation cooling. The temperature was monitored over time at the surface, as well as at specific points according to Figure 5.9.

The results from $\sum$MIT were compared to the results from PATO and shown in Figure 5.12. The two codes show excellent agreement in the in-depth and surface temperature response. Both PATO and $\sum$MIT share similarities in the physics and chemistry models, utilizing the same energy balance, mass balance, and decomposition model. Differences arise due to the numerical methods employed in the two codes. PATO uses a finite volume method.

Table 5.5: Ablation Workshop 2.1 Boundary Condition Values

Time	$\rho_e u_e C_H$	h_r	Pressure
(sec)	(kg/m^2/s)	(J/kg)	(atm)
0	0	0	1
0.1	0.3	1.5e6	1
60	0.3	1.5e6	1
60.1	0	0	1
120	0	0	1

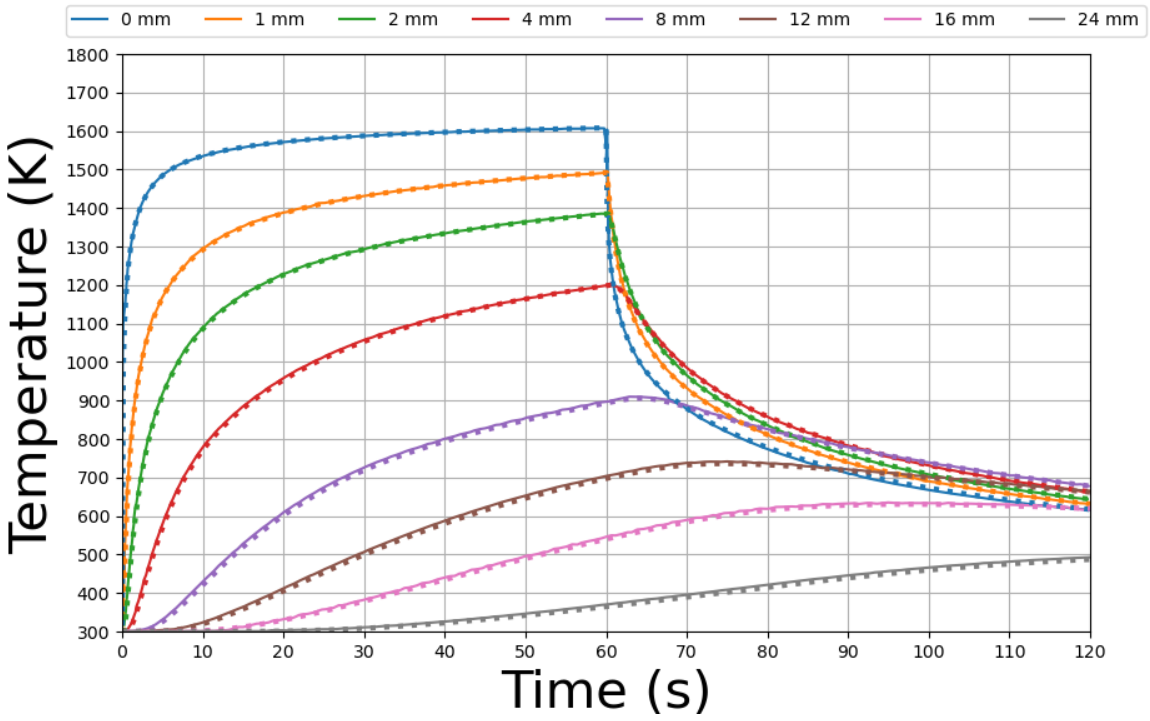

Figure 5.12: Comparison of our result (dotted lines) versus PATO (solid lines) for temperature as a function of time for the Ablation Workshop test case 2.1.

5.8 Mesh Recession Patch Tests

In this section, a verification of the mesh recession algorithm is demonstrated by conducting three simple 2D patch tests. In the finite element literature, a patch test is a verification procedure aimed at ensuring the proper functioning of a finite element code [101]. Generally, it involves solving a partial differential equation on a simple mesh with multiple elements and comparing the results to a known analytical solution. For an exact match, the analytical solution must belong to the same polynomial space as the shape functions employed.

5.8.1 Thermal Patch Test

The first patch test example involves a 1-m by 1-m 2D domain with an initial temperature field and a constant density, as depicted in Figure 5.13a. A constant recession rate is applied to the right edge of the square, causing a decrease in the rectangle's length along the negative x-direction. Figure 5.13b shows the resulting reference configuration with the deformed mesh and the updated temperature field. The temperature associated with the ablated material is no longer considered within the model's domain.

To obtain the correct temperature field for the new reference configuration, the boundary nodes on the right edge are moved to the left by an amount equivalent to the ablation amount. Following node adjustments, the shape functions are recalculated, and the temperature field is interpolated from the original reference configuration mesh to the updated one. This example illustrates two critical aspects: 1) conservation of mass, where the total mass of the original material equals the sum of the mass lost through ablation and the remaining material, and 2) proper attribution of the new temperature field to the updated reference configuration mesh, thereby excluding temperature values related to the lost mass.

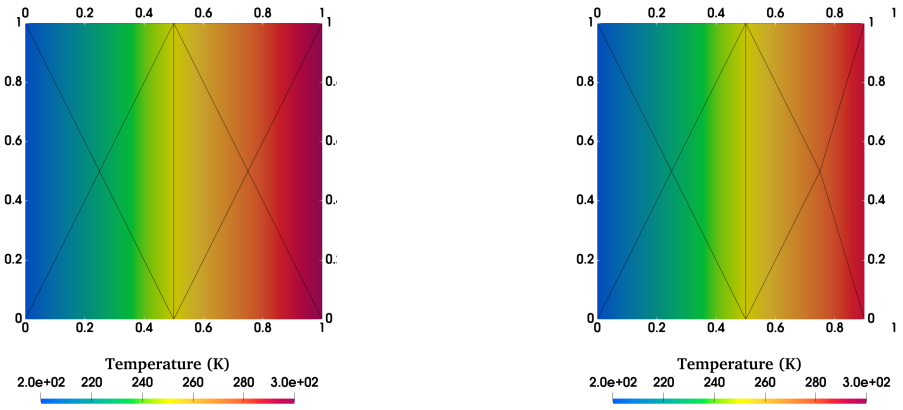

(a) Temperature field prior to mesh recession. (b) Temperature field after mesh recession.

Figure 5.13: Temperature field for the first mesh recession example.

5.8.2 Mechanical Patch Test

To verify that the mesh recession algorithm correctly preserves mass and energy in the context of mechanical loading, two additional finite element patch tests were conducted. In each patch test, a 1-m by 1-m 2D domain with a zero displacement field and a constant density was used. Both tests followed this step-by-step procedure: 1) a load is applied to one edge of the square and the resulting displacement field is computed, 2) a constant recession amount is applied to either the same edge or a different one, and the stress and displacement fields are interpolated from the previous reference configuration to the updated reference

configuration, and 3) a final round of loading is performed, and the computed displacement field is compared to the analytical displacement field. A linear elastic constitutive model was used for both tests. All rounds of loading used a static equilibrium solution procedure to obtain the displacement field. The difference between the two patch tests is the edge to which the load is applied. In the first mechanics patch test, the load is applied to the right edge of the rectangle, while in the second mechanics patch test, the load is applied to the top edge of the rectangle. The purpose was to test the mesh recession algorithm's ability to recede the mesh in the same direction as the applied load in the first patch test, as well as test recession on an edge and in a direction different than the applied load in the second patch test.

Figure 5.14a shows the displacement field after applying the load to the first mechanics patch test. Subsequently, a constant recession amount was applied to the same edge, and the stress and displacement fields were interpolated from the previous reference configuration to the updated reference configuration, as depicted in Figure 5.14b. To confirm the proper application of loading after the recession, a final round of loading was performed, as illustrated in Figure 5.14c. The computed displacement field was compared to the analytical displacement field, and an exact match was observed for all rounds of loading. This example verifies the mesh recession algorithm's ability to properly resolve the displacement field when loading and recession occur on the same edge and in the same direction.

In the second mechanics patch test, the load was applied to the top rather than the right edge of the rectangle. Figure 5.15a shows the displacement field after the load was applied. Then, the mesh recession algorithm was applied to the right edge of the rectangle, as shown in Figure 5.15b. Finally, a final round of loading was applied, as depicted in Figure 5.15c. This example verifies the mesh recession algorithm's ability to properly resolve the displacement field when loading and recession occur on different edges and in different directions.

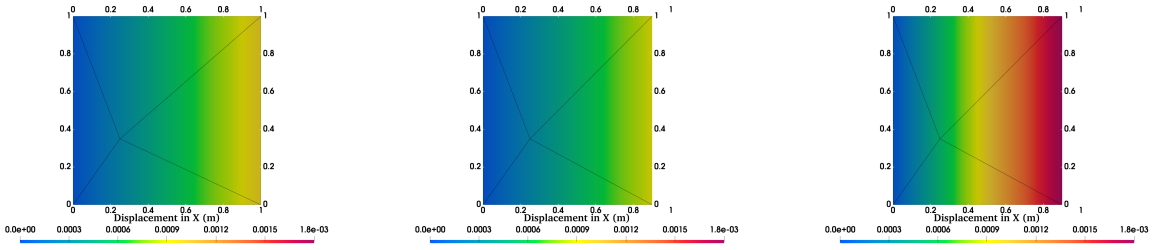

(a) Step 1 - First round of loading. (b) Step 2 - Mesh recession after first round of loading. (c) Step 3 - Loading after step 2.

Figure 5.14: Displacement fields after each step of loading and mesh recession in the first mechanics patch test.

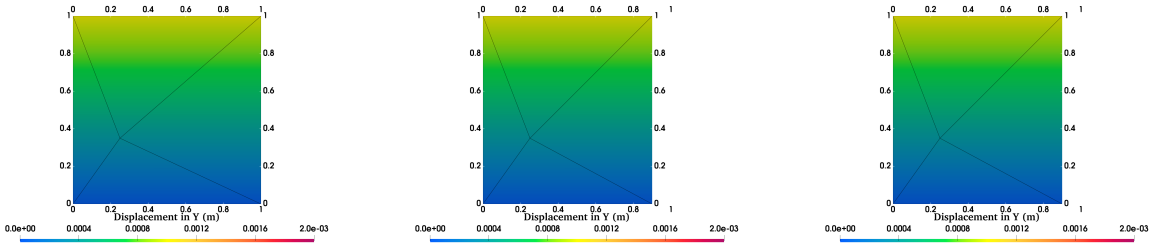

(a) Step 1 - First round of loading.

(b) Step 2 - Mesh recession after first round of loading.

(c) Step 3 - Loading after step 2.

Figure 5.15: Displacement fields after each step of loading and mesh recession in the second mechanics patch test.

5.9 Simulation of an Arc-Jet Ablative Experiment

In this section, a fully-coupled thermo-chemo-mechanical simulation of a PICA sample in a high-enthalpy hypersonic wind tunnel, known as an arc-jet facility, is presented. Such facilities are used to perform experiments where samples of ablative material are subjected to high heat fluxes, representative of the extreme conditions encountered in atmospheric reentry. Typically a sample with a small cylinder with a spherical cap and rounded corners, known as an iso-q sample, is used. The name iso-q comes from the fact that the heat flux is approximately constant on its surface during experiments. Figure 5.16, taken from [102], shows an iso-q specimen in an arc-jet experiment.

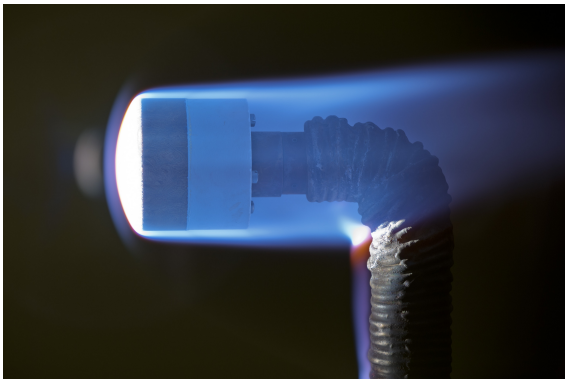

Figure 5.16: Arc-jet test of an iso-q sample. Taken from [102].

To simulate this type of experiment in $\sum$MIT, a 2D half cross-section of an iso-q geometry was modeled in plane strain. Figure 5.17 shows the meshed geometry, with colors on the edges corresponding to the boundary conditions summarized in Table 5.6. An initial temperature of 300 K, pressure of 1 atm, density of 280 kg/m^3, displacement of 0 m, and velocity of 0 m/s were applied. The temperature on the face of the iso-q was raised from 300 K to 3300 K in 10 seconds. The linear thermoelastic constitutive model in Section 3.3 was used to model the mechanical response of the material with the charred PICA properties from [71], summarized in Table 5.7. Conversely, heat and mass transfer were modeled using

the TACOT thermophysical properties [28] summarized in the appendix (see Sections A.1 and A.2). Pyrolysis was modeled using the Torres-Herrador model described in Section 3.7.2. Finally, ablation was modeled using recession rate calculations from the B' table of TACOT (see Section A.3) by using the temperature, pressure, and gas mass flux at the iso-q surface to lookup B'_c. The simulation time was 10 seconds, with a time step of 0.001 seconds.

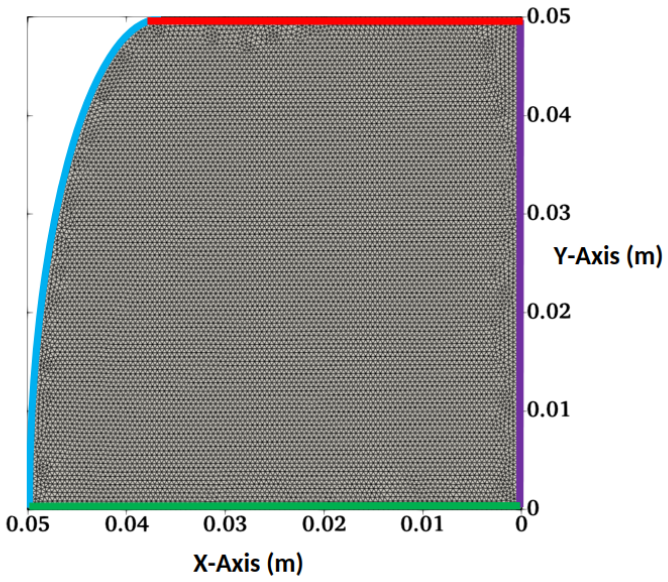

Figure 5.17: Mesh of the iso-q geometry used in ∑MIT. Colors on the boundaries correspond to the boundary conditions listed in Table 5.6.

Boundary	Mechanics BC Type	Thermal BC Type	Mass Transport BC Type
Face	Atmospheric pressure	Fixed temperature	Atmospheric pressure
Top	Zero traction	Adiabatic	Impermeable
Bottom	Symmetry	Adiabatic	Impermeable
Right	Zero displacement	Adiabatic	Impermeable

Table 5.6: Table of iso-q boundary conditions.

After 10 seconds, the temperature reached 3300 K on the curved edge of the iso-q specimen, as shown in Figure 5.18a. The resulting thermal gradients lead to thermal expansion and corresponding thermal stresses in the material. Figure 5.18b shows the von Mises stress reaches a maximum value of approximately 3.5 MPa. This stress is similar to the strength of PICA measured by Parmenter et al. [40], who found that the compressive strength of PICA ranges from 1 to 6 MPa. In particular, they measured the strength of virgin and charred PICA, as well as FiberForm in compression experiments and hardness tests. They found that its mean strength is 3.54 MPa with a standard deviation of 0.65 MPa for the transverse-compression experiments they performed. This suggests that thermally-induced stresses may be sufficient to cause damage to the material during an arc-jet experiment. The

current framework does not model damage or plasticity, but these models could be added in the future to investigate the effect of these phenomena on the response of the material. However, the thermoelastic effect, critical in the material's response, is effectively modeled in this simulation.

Another consequence of temperature changes in the material is the initiation of pyrolysis chemical reactions. This phenomenon leads to mass loss of the solid material by converting it to gas and leaving behind a charred residue. The model represents this by tracking the solid mass density field. The effect of pyrolysis on the solid mass density is shown after 10 seconds in Figure 5.18c. Inside the material, where the temperature has not yet increased, the mass density is that of the virgin material, 280 kg/m^3. Near the curved edge of the iso-q specimen, where the temperature has increased substantially, the material is fully charred with a mass density of 220 kg/m^3. These two regions are separated by another region where the material is partially charred, where the solid mass density is between 220 and 280 kg/m^3. This resembles the diagram shown in Figure 1.2, where the virgin, charred, and decomposition zones are clearly visible.

The degree of char, β, is calculated using the current solid mass density and the virgin and charred solid mass densities (3.19). This variable is used to determine the thermophysical properties and the porosity of the material, as explained in Section 3. The porosity field after 10 seconds is shown in Figure 5.18d, which is interpolated between the virgin porosity of 0.8 and the char porosity of 0.85 using the degree of char.

Mechanical deformation of PICA depends not only on thermoelastic effects, but also on the extent of pyrolysis. As the material chars, it becomes less stiff and weaker. Although the framework supports modifying mechanical properties based on the degree of char, this simulation shown does not use this feature, and instead uses the char mechanical properties in Table 5.7 for the entire simulation. The effect of pyrolysis on the mechanical response of the material is left for future work.

The results shown in all of the figures (5.18a, 5.18d, 5.18b, and 5.18c) show the effect of ablation on the shape of the iso-q specimen. The original reference domain is plotted in black behind each figure to compare against the receded mesh. The maximum recession amount at 10 seconds was approximately 1.2 mm. Recall that recession rates were obtained by using a lookup of B_c' values using the pressure, temperature, and mass flux at the boundary.

The results in Figure 5.18 demonstrate the ability of the framework adopted in this work to simulate the thermo-chemo-mechanical response of PICA during an arc-jet experiment. It solves the internal energy balance equation to resolve the temperature distribution inside the iso-q sample and successfully captures thermal expansion and stress generation due to the temperature field, thanks to its coupling of thermal and mechanical effects. The stresses quantified by this simulation are comparable to PICA's strength, implying that a more comprehensive model incorporating damage and plasticity may be necessary for a more accurate representation of the material's behavior. Moreover, the simulation comprehensively accounts for the chemical effects of pyrolysis, which lead to changes in material properties, including porosity increase and mass loss. It further captures the phenomenon of ablation, a critical aspect of TPS material behavior in arc-jet experiments, by orchestrating surface recession and mesh updates based on the recession rates obtained from a B' table.

Parameter	Value	Units
ρ	280	kg/m^3
E	1.73	GPa
ν	0.3	
α	2.6×10^{-3}	K^{-1}

Table 5.7: Linear elastic mechanical properties of PICA [71].

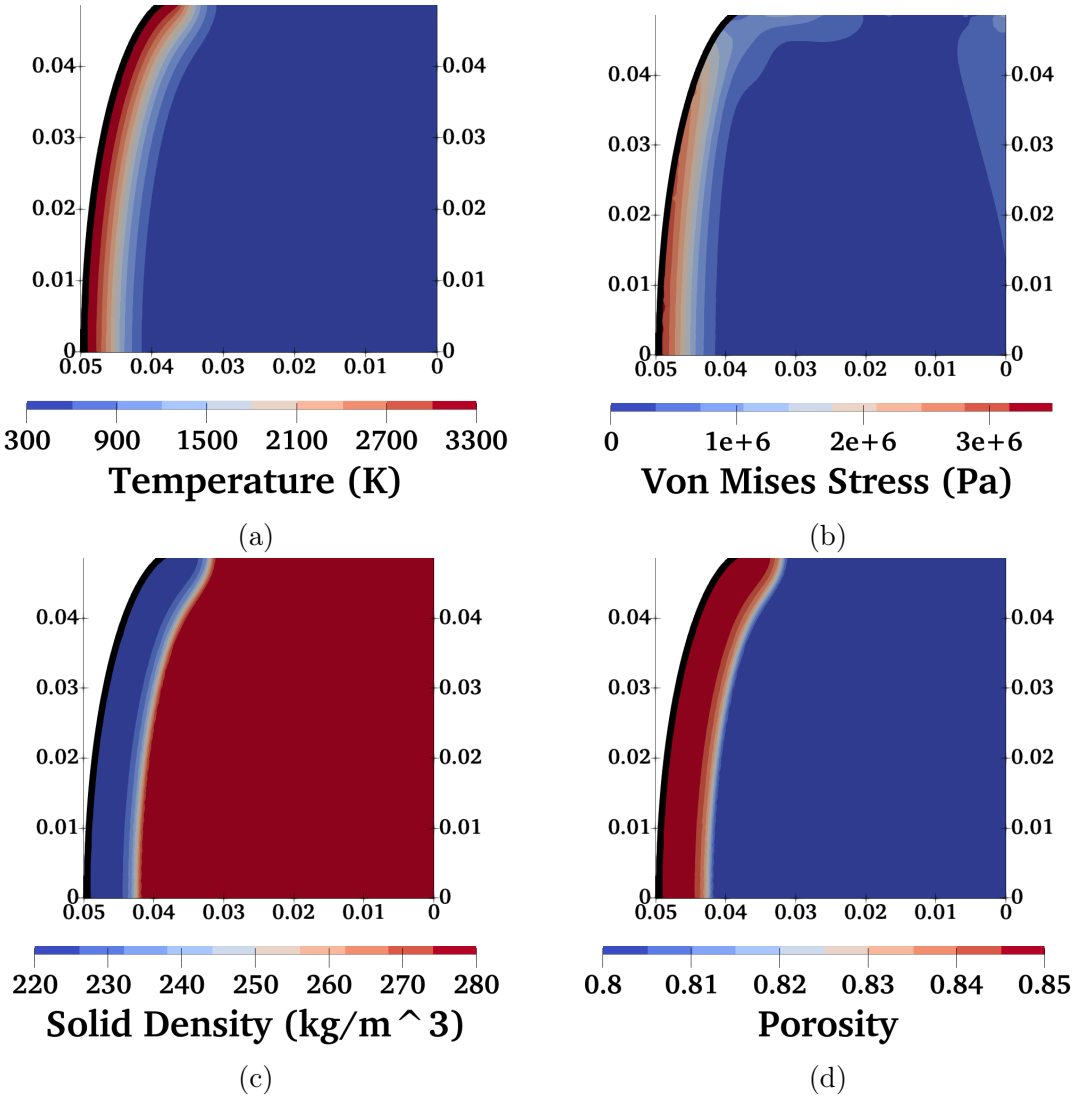

Figure 5.18: Results from the iso-q simulation at $t = 10$ seconds.

Chapter 6

Summary and Conclusions

The main objectives of this thesis were to 1) develop a thermo-chemo-mechanical continuum theory specialized for ablative thermal protection systems, 2) develop a computational framework for solving the governing equations of the theory, and 3) verify the computational framework and demonstrate its capabilities. The computational framework was developed in $\sum$MIT, a finite element simulation code developed by the Radovitzky Research Group at MIT.

The modeling framework proposed is grounded in a continuum theory that contemplates heat conduction in the solid material, chemical kinetics of the pyrolysis reaction, gas transport and advection of thermal energy within the porous material, mechanical response of the solid material due to thermal and chemical effects, and thermochemical ablation. The theory is derived from basic kinematics, balance laws, and constitutive theory for the multiphase system, and then specialized to the case of ablative thermal protection systems to obtain a specific set of governing equations whose solution gives the state of the material in terms of temperature, pressure, and displacement. To this end, a Lagrangian continuum framework is proposed with established constitutive models for the mechanical, thermal, mass transfer, and chemical problems. A system of equations is derived that includes a solid/gas mixture energy balance equation, a gas mass balance, and a force balance of the solid body.

To solve the governing equations, a computational framework was developed. The ablation of the material is modeled by using a surface energy balance equation along with a thermochemical equilibrium model. The governing equations are solved using a high-order finite element method known as the discontinuous Galerkin (DG) method, as developed in [77–79]. The representation of surface ablation is numerically achieved by using a mesh recession algorithm. Finally, the solid mechanics and heat and mass transport equations are coupled using a staggered approach.

The computational framework was verified against several analytical solutions to the heat equation, and benchmark numerical solutions. Each pyrolysis model that was implemented in $\sum$MIT was demonstrated. Subsequently, verification cases of the energy balance equation are presented, including well-known analytical solutions to the heat equation and benchmark test case examples. Following this, a verification of the mesh recession algorithm was demonstrated through a series of patch tests. Finally, a thermo-chemo-mechanical simulation of an arc-jet experiment was presented, which illustrates the computational framework's ability to

model thermo-chemically induced deformation, stresses, and surface recession in pyrolyzing TPS materials.

Appendix A

Theoretical Ablative Composite for Open Testing (TACOT) Material Properties

The Theoretical Ablative Composite for Open Testing (TACOT) material model [61] is used throughout this thesis. TACOT is a fictitious material commonly used in code-to-code comparisons, such as the Ablation Workshop Test Case series [64–66]. Its properties are based on commonly-used low-density ablators, such as PICA. In this section, the TACOT properties are presented for reference. The first section provides the thermophysical properties of the solid, while the second section provides the thermophysical properties of the gas. The third and final section of this appendix provides the B' table values for TACOT.

A.1 Thermophysical Properties of Solids

In this section, the thermophysical properties of the TACOT solid are presented. The isotropic thermal conductivities are shown in Figure A.1. The solid mass specific enthalpies are illustrated in Figure A.2. Furthermore, Figure A.3 shows the specific heat capacities. Each plot includes both virgin and char properties. For a partially-charred material, the thermal conductivity is calculated using (3.70), while the solid mass specific heat capacity is derived from (3.35). The partial heat of charring, shown in Figure A.4, is calculated using the solid specific enthalpy of the char and virgin mass in (3.27).

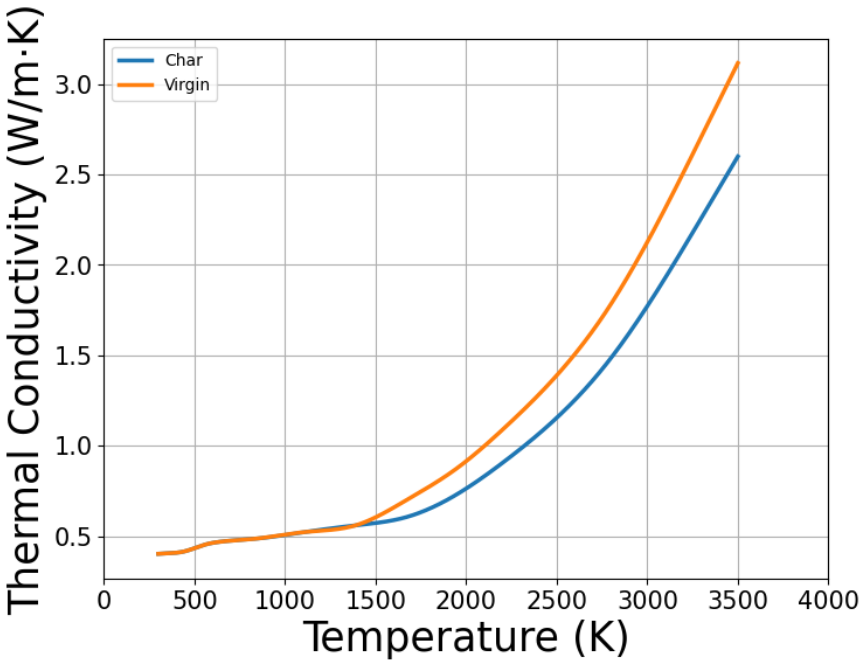

Figure A.1: Thermal conductivity.

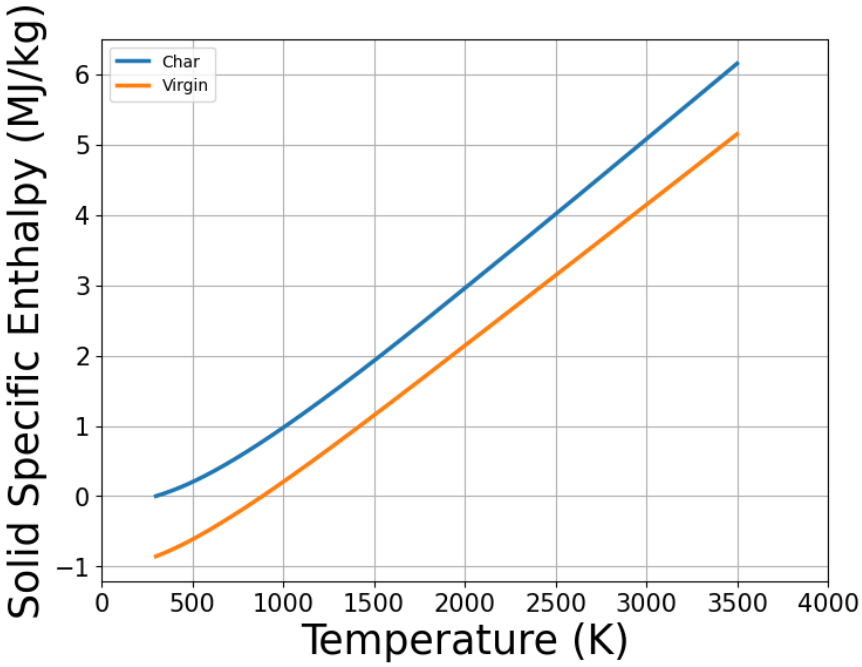

Figure A.2: Solid mass enthalpy.

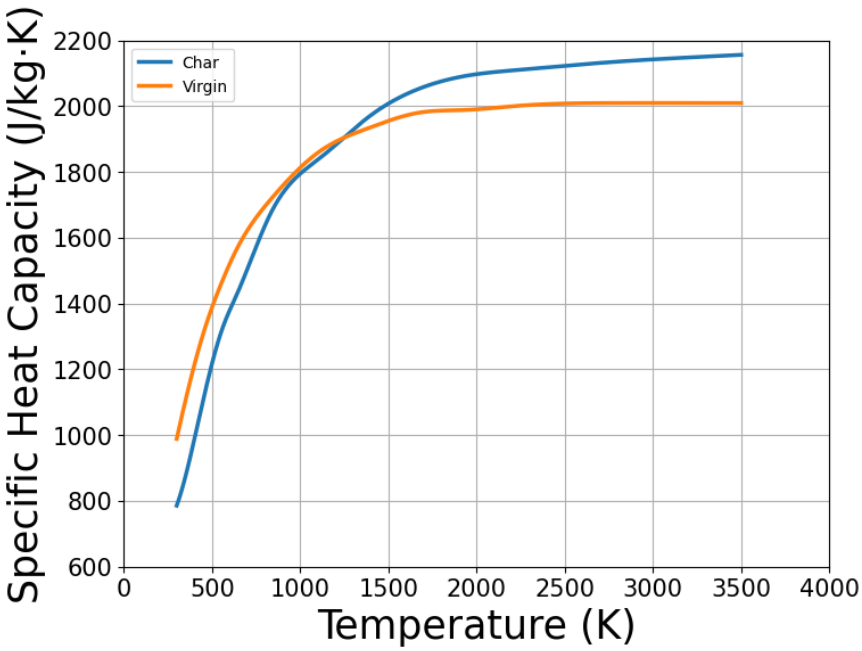

Figure A.3: Specific heat capacity.

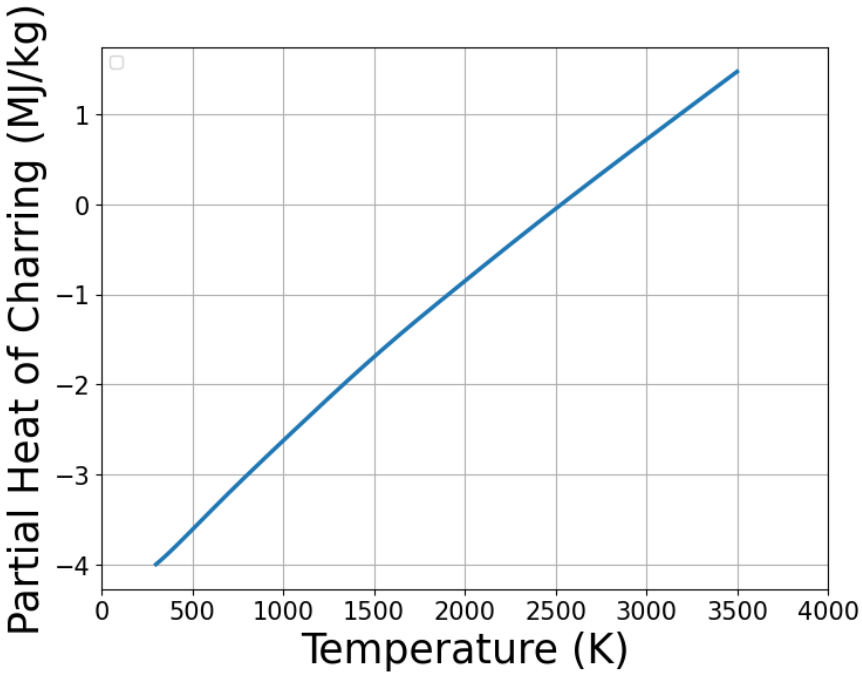

Figure A.4: Partial heat of charring.

A.2 Thermophysical Properties of Gases

In this section, the thermophysical properties of the TACOT gas are presented. Figure A.5 shows the gas specific enthalpy as a function of temperature at a pressure of 1 atm. The gas viscosity as a function of temperature at 1 atm is shown in Figure A.6. Finally, Figure A.7 shows the gas molecular weight as a function of temperature at a pressure of 1 atm.

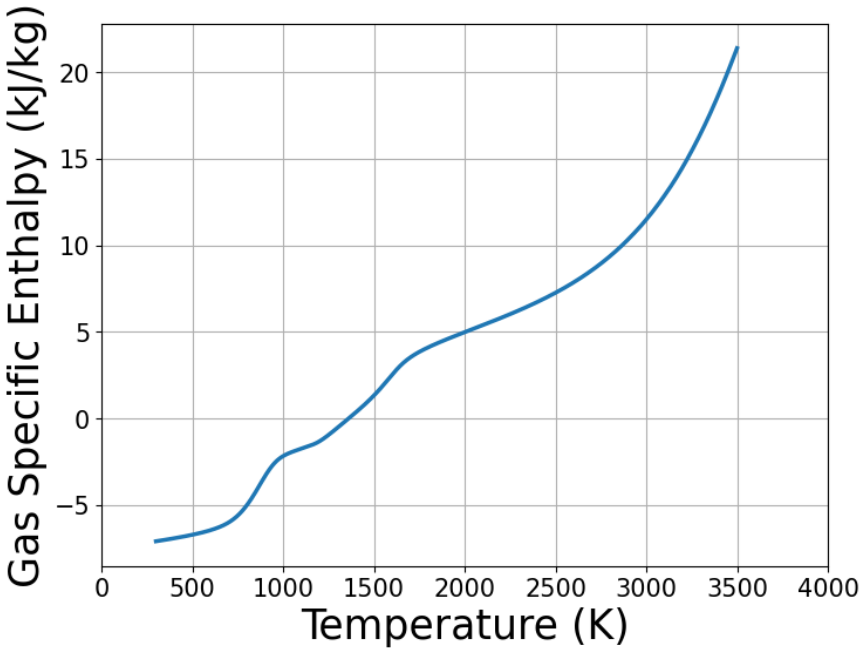

Figure A.5: Gas enthalpy of TACOT as a function of temperature at a pressure of 1 atm.

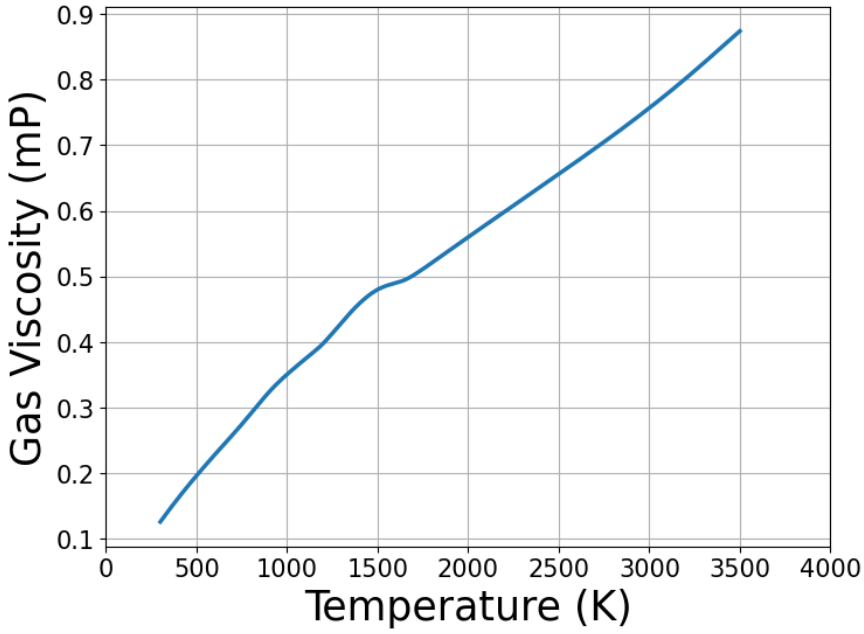

Figure A.6: Gas viscosity of TACOT as a function of temperature at a pressure of 1 atm.

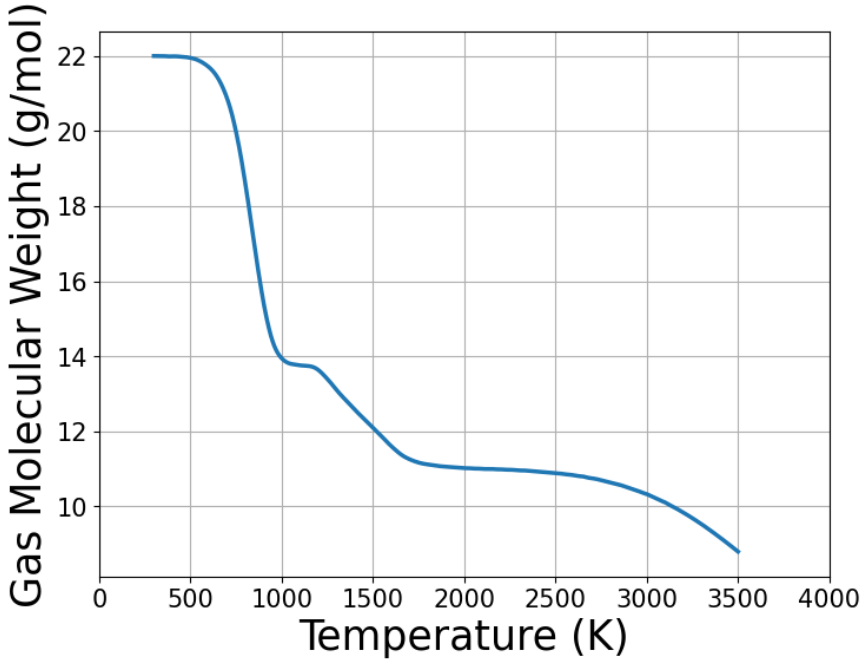

Figure A.7: Gas molecular weight of TACOT as a function of temperature at a pressure of 1 atm.

A.3 B′ Table

In this section, the B' table values are presented for a pressure of 1 atm. Recall the definition of B'_g and B'_c from (3.93). Figure A.8 shows the B'_c values as a function of temperature for different B'_g values. Figure A.9 shows h_w as a function of temperature for different B'_g values. The B' table lookup is usually an iterative procedure that involves calculating B'_g, correcting it using the blowing corrections, and then looking up the B'_c and h_w values from the table. This process is done consistently with the surface energy balance model, described in Section 3.8.

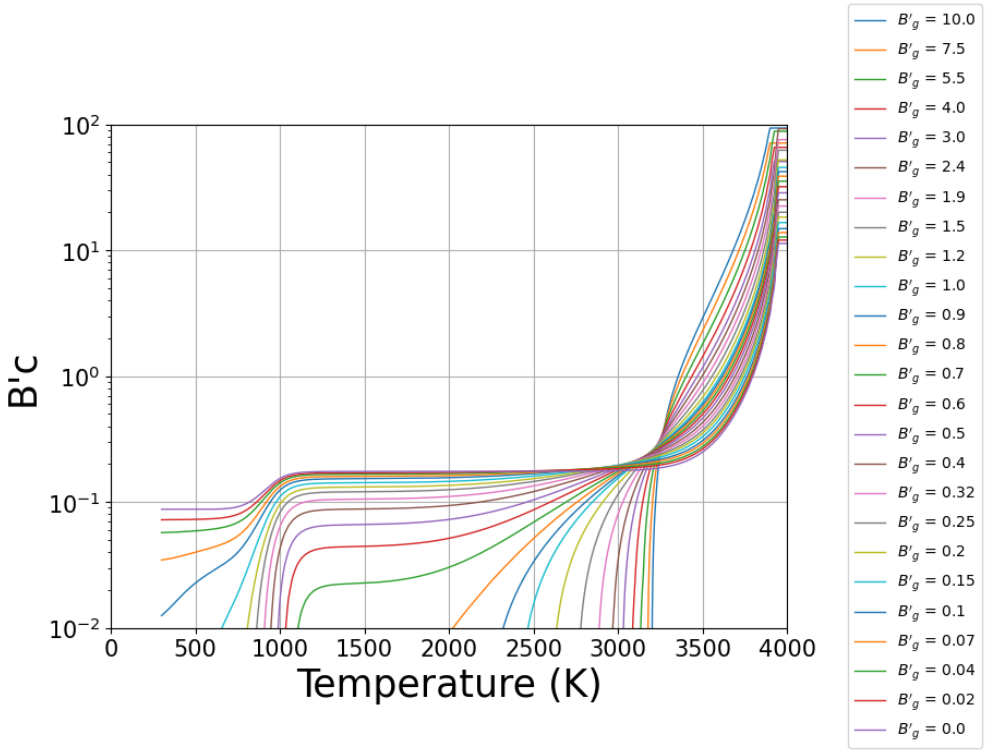

Figure A.8: B'c values from B prime table at a pressure of 1 atm.

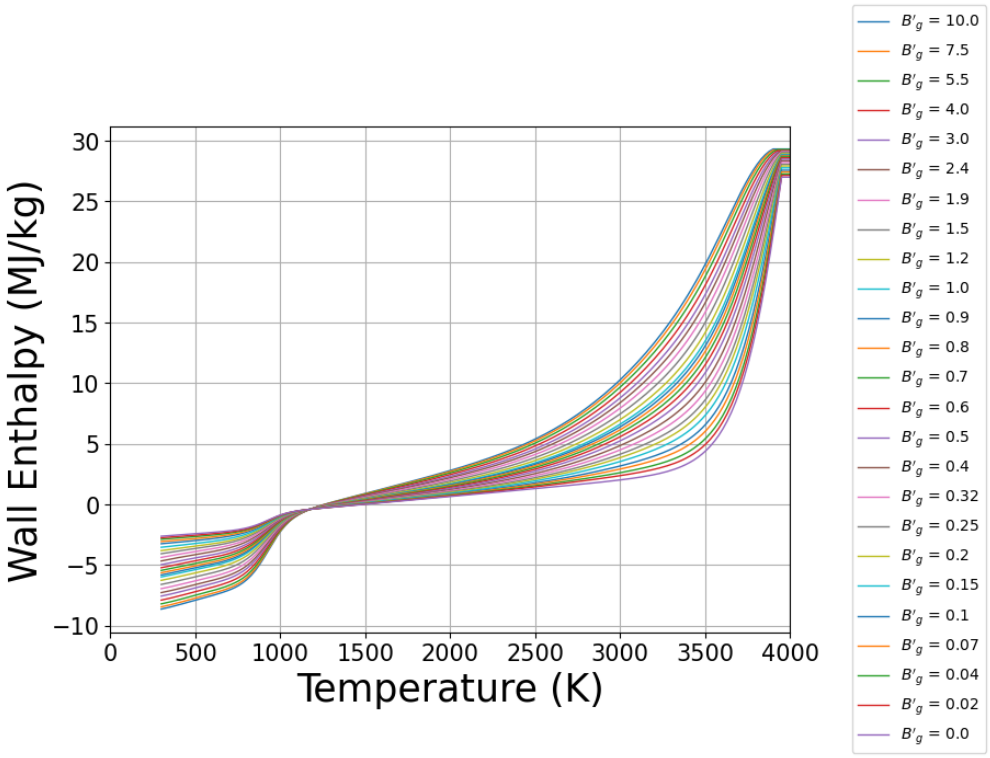

Figure A.9: hw values from B prime table at a pressure of 1 atm.

Bibliography

[1] R.D. Launius and D.R. Jenkins. *Coming Home: Reentry and Recovery from Space*. NASA/SP. National Aeronautics and Space Administration, Aeronautics Research Mission Directorate, 2012. URL: https://books.google.com/books?id=d3-gwAEACAAJ.

[2] Mostafa Barzegar Gerdroodbary. "1 - Introduction". In: *Aerodynamic Heating in Supersonic and Hypersonic Flows*. Ed. by Mostafa Barzegar Gerdroodbary. Elsevier, 2023, pp. 1–16. ISBN: 978-0-323-91770-4. DOI: https://doi.org/10.1016/B978-0-323-91770-4.00001-X. URL: https://www.sciencedirect.com/science/article/pii/B978032391770400001X.

[3] John J. Bertin. *Hypersonic aerothermodynamics*. eng. AIAA education series. Washington, DC: American Institute of Aeronautics and Astronautics, 1994. ISBN: 1563470365.

[4] Scott A. Berry Thomas J. Horvath and N. R. Merski. *Hypersonic Boundary/Shear Layer Transition for Blunt to Slender Configurations - A NASA Langley Experimental Perspective*. Report. National Aeronautics and Space Administration Hampton VA Langley Research Center, 2004.

[5] Georges Duffa. *Ablative Thermal Protection Systems Modeling*. American Institute of Aeronautics and Astronautics, 2013.

[6] H J Allen and A J Eggers Jr. "A Study of the Motion and Aerodynamic Heating of Missiles Entering the Earth's Atmosphere at High Supersonic Speeds". In: (Oct. 1957). URL: https://www.osti.gov/biblio/4349875.

[7] R. B. Erb and S. Jacobs. *Entry Performance of the Mercury Spacecraft Heat Shield*. Technical Report 19660006061. NASA, 1964.

[8] Jr. Graves R. A. and W. G. Witte. *Flight test analysis of Apollo heat shield material using the Pacemaker vehicle system*. Technical Report 19680021275. NASA, 1968.

[9] Jeremy C. Vander Kam and Peter Gage. "Estimating Orion Heat Shield Failure due to Ablator Cracking". In: *Journal of Spacecraft and Rockets* 58.5 (2021), pp. 1263–1270. DOI: 10.2514/1.A35003. URL: https://doi.org/10.2514/1.A35003.

[10] Eric L. Strauss. "Superlight ablative systems for Mars lander thermal protection." In: *Journal of Spacecraft and Rockets* 4.10 (1967), pp. 1304–1309. DOI: 10.2514/3.29076. eprint: https://doi.org/10.2514/3.29076. URL: https://doi.org/10.2514/3.29076.

[11] L. Nolte and S. Sommer. "Probing a planetary atmosphere - Pioneer Venus spacecraft description". In: *Conference on the Exploration of the Outer Planets*. DOI: 10.2514/6.1975-1160. eprint: https://arc.aiaa.org/doi/pdf/10.2514/6.1975-1160. URL: https://arc.aiaa.org/doi/abs/10.2514/6.1975-1160.

[12] J. Givens, L. Nolte, and L. Pochettino. "Galileo Atmospheric Entry Probe System - Design, development, and test". In: *21st Aerospace Sciences Meeting*. DOI: 10.2514/6.1983-98. eprint: https://arc.aiaa.org/doi/pdf/10.2514/6.1983-98. URL: https://arc.aiaa.org/doi/abs/10.2514/6.1983-98.

[13] Huy Tran et al. "Phenolic Impregnated Carbon Ablators (PICA) for Discovery class missions". In: *31st Thermophysics Conference*. 1996. DOI: 10.2514/6.1996-1911. eprint: https://arc.aiaa.org/doi/pdf/10.2514/6.1996-1911. URL: https://arc.aiaa.org/doi/abs/10.2514/6.1996-1911.

[14] Mairead Stackpoole et al. "Post-Flight Evaluation of Stardust Sample Return Capsule Forebody Heatshield Material". In: Jan. 2008. ISBN: 978-1-62410-128-1. DOI: 10.2514/6.2008-1202.

[15] Todd R. White et al. "Post-flight Analysis of Mars Science Laboratory's Entry Aerothermal Environment and Thermal Protection System Response". In: *44th AIAA Thermophysics Conference*. 2013. DOI: 10.2514/6.2013-2779.

[16] Michael J. Wright et al. "Sizing and Margins Assessment of Mars Science Laboratory Aeroshell Thermal Protection System". In: *Journal of Spacecraft and Rockets* 51.4 (2014), pp. 1125–1138. DOI: 10.2514/1.A32579. eprint: https://doi.org/10.2514/1.A32579. URL: https://doi.org/10.2514/1.A32579.

[17] Karl T. Edquist et al. "Mars Science Laboratory Heat Shield Aerothermodynamics: Design and Reconstruction". In: *Journal of Spacecraft and Rockets* 51.4 (2014), pp. 1106–1124. DOI: 10.2514/1.A32749. eprint: https://doi.org/10.2514/1.A32749. URL: https://doi.org/10.2514/1.A32749.

[18] Jean Lachaud et al. "Detailed chemical equilibrium model for porous ablative materials". In: *International Journal of Heat and Mass Transfer* 90 (2015), pp. 1034–1045. ISSN: 0017-9310. DOI: https://doi.org/10.1016/j.ijheatmasstransfer.2015.05.106. URL: https://www.sciencedirect.com/science/article/pii/S0017931015006006.

[19] Adam J. Amar. "Modeling of One-Dimensional Ablation with Porous Flow Using Finite Control Volume Procedure". PhD thesis. North Carolina State University, Nov. 2006.

[20] K. Kratsch, L. Hearne, and H. McChesney. "Thermal Performance of Heat Shield Composites During Planetary Entry". In: *Engineering Problems of Manned Interplanetary Exploration*. 1963. DOI: 10.2514/6.1963-1515. eprint: https://arc.aiaa.org/doi/pdf/10.2514/6.1963-1515. URL: https://arc.aiaa.org/doi/abs/10.2514/6.1963-1515.

[21] K. Kratsch, W. Loomis, and P. Randles. "Jupiter Probe Heatshield design". In: *18th Structural Dynamics and Materials Conference*. 1977. DOI: 10.2514/6.1977-427. eprint: https://arc.aiaa.org/doi/pdf/10.2514/6.1977-427. URL: https://arc.aiaa.org/doi/abs/10.2514/6.1977-427.

[22] E. Bartlett and R. Kendall. "Thermochemical ablation". In: *Thermophysics Specialist Conference*. 1965. DOI: 10.2514/6.1965-642. eprint: https://arc.aiaa.org/doi/pdf/10.2514/6.1965-642. URL: https://arc.aiaa.org/doi/abs/10.2514/6.1965-642.

[23] Marvin B. Dow, Robert T. Swann, and Stephen S. Tompkins. "Analysis of the effects of environmental conditions on the performance of charring ablators." In: *Journal of Spacecraft and Rockets* 3.1 (1966), pp. 61–67. DOI: 10.2514/3.28386. eprint: https://doi.org/10.2514/3.28386. URL: https://doi.org/10.2514/3.28386.

[24] Brody Bessire, Sridhar Lahankar, and Timothy Minton. "Pyrolysis of Phenolic Impregnated Carbon Ablator (PICA)". In: *ACS applied materials and interfaces* 7 (Dec. 2014). DOI: 10.1021/am507816f.

[25] Brody K. Bessire and Timothy K. Minton. "Decomposition of Phenolic Impregnated Carbon Ablator (PICA) as a Function of Temperature and Heating Rate". In: *ACS Applied Materials and Interfaces* 9.25 (2017). PMID: 28544848, pp. 21422–21437. DOI: 10.1021/acsami.7b03919. eprint: https://doi.org/10.1021/acsami.7b03919. URL: https://doi.org/10.1021/acsami.7b03919.

[26] Francisco Torres-Herrador et al. "A high heating rate pyrolysis model for the Phenolic Impregnated Carbon Ablator (PICA) based on mass spectroscopy experiments". In: *Journal of Analytical and Applied Pyrolysis* 141 (2019), p. 104625. ISSN: 0165-2370. DOI: https://doi.org/10.1016/j.jaap.2019.05.014. URL: https://www.sciencedirect.com/science/article/pii/S0165237019301603.

[27] Jason Rabinovitch, Vanessa M. Marx, and Guillaume Blanquart. "Pyrolysis Gas Composition for a Phenolic Impregnated Carbon Ablator Heatshield". In: *11th AIAA/ASME Joint Thermophysics and Heat Transfer Conference*. 2014. DOI: 10.2514/6.2014-2246. eprint: https://arc.aiaa.org/doi/pdf/10.2514/6.2014-2246. URL: https://arc.aiaa.org/doi/abs/10.2514/6.2014-2246.

[28] J. Lachaud et al. "A generic local thermal equilibrium model for porous reactive materials submitted to high temperatures". In: *International Journal of Heat and Mass Transfer* 108 (2017), pp. 1406–1417. ISSN: 0017-9310. DOI: https://doi.org/10.1016/j.ijheatmasstransfer.2016.11.067. URL: https://www.sciencedirect.com/science/article/pii/S0017931016312480.

[29] Joseph C. Ferguson et al. "Modeling the oxidation of low-density carbon fiber material based on micro-tomography". In: *Carbon* 96 (2016), pp. 57–65. ISSN: 0008-6223. DOI: https://doi.org/10.1016/j.carbon.2015.08.113. URL: https://www.sciencedirect.com/science/article/pii/S0008622315302153.

[30] Joseph C. Ferguson et al. "Theoretical study on the micro-scale oxidation of resin-infused carbon ablators". In: *Carbon* 121 (2017), pp. 552–562. ISSN: 0008-6223. DOI: https://doi.org/10.1016/j.carbon.2017.06.013. URL: https://www.sciencedirect.com/science/article/pii/S0008622317305808.

[31] Francesco Panerai et al. "Micro-tomography based analysis of thermal conductivity, diffusivity and oxidation behavior of rigid and flexible fibrous insulators". In: *International Journal of Heat and Mass Transfer* 108 (2017), pp. 801–811. ISSN: 0017-9310. DOI: https://doi.org/10.1016/j.ijheatmasstransfer.2016.12.048. URL: https://www.sciencedirect.com/science/article/pii/S0017931016327235.

[32] Joseph C. Ferguson et al. "PuMA: the Porous Microstructure Analysis software". In: *SoftwareX* 7 (2018), pp. 81–87. ISSN: 2352-7110. DOI: https://doi.org/10.1016/j.softx.2018.03.001. URL: https://www.sciencedirect.com/science/article/pii/S2352711018300281.

[33] Federico Semeraro et al. "Anisotropic analysis of fibrous and woven materials part 1: Estimation of local orientation". In: *Computational Materials Science* 178 (2020), p. 109631. ISSN: 0927-0256. DOI: https://doi.org/10.1016/j.commatsci.2020.109631. URL: https://www.sciencedirect.com/science/article/pii/S0927025620301221.

[34] Federico Semeraro et al. "Anisotropic analysis of fibrous and woven materials part 2: Computation of effective conductivity". In: *Computational Materials Science* 186 (2021), p. 109956. ISSN: 0927-0256. DOI: https://doi.org/10.1016/j.commatsci.2020.109956. URL: https://www.sciencedirect.com/science/article/pii/S092702562030447X.

[35] Sergio Fraile Izquierdo, Federico Semeraro, and Marcos Acín. "Multi-Scale Analysis of Effective Mechanical Properties of Porous 3D Woven Composite Materials". In: *AIAA SCITECH 2022 Forum*. DOI: 10.2514/6.2022-2281. eprint: https://arc.aiaa.org/doi/pdf/10.2514/6.2022-2281. URL: https://arc.aiaa.org/doi/abs/10.2514/6.2022-2281.

[36] Pedro C.F. Lopes et al. "Simulation toolkit for digital material characterization of large image-based microstructures". In: *Computational Materials Science* 219 (2023), p. 112021. ISSN: 0927-0256. DOI: https://doi.org/10.1016/j.commatsci.2023.112021. URL: https://www.sciencedirect.com/science/article/pii/S0927025623000150.

[37] Rui Fu, Simon Schmitt, and Alexandre Martin. "Thermo-Chemical-Structural Modeling of Carbon Fiber Pitting and Failure Mechanism". In: *AIAA SCITECH 2022 Forum*. American Institute for Aeronauics an dAstronautics. 2022. DOI: 10.2514/6.2022-1282. eprint: https://arc.aiaa.org/doi/pdf/10.2514/6.2022-1282. URL: https://arc.aiaa.org/doi/abs/10.2514/6.2022-1282.

[38] Bradley D. Butler et al. "Characterization of Candidate Materials for Remote Recession Measurements of Ablative Heat Shield Materials". In: *54th AIAA Aerospace Sciences Meeting*. 2016. DOI: 10.2514/6.2016-1516. URL: https://arc.aiaa.org/doi/abs/10.2514/6.2016-1516.

[39] Jun Zhang et al. "Comparison of ablative and compressive mechanical behavior of several PICA-like ablative materials". In: *Science China Technological Sciences* (2020). DOI: 10.1007/s11431-020-1618-2.

[40] Kelly E. Parmenter et al. "Compressive Response of Lightweight Ceramic Ablators: Phenolic Impregnated Carbon Ablator". In: *Journal of Spacecraft and Rockets* 38.2 (2001), pp. 231–236. DOI: 10.2514/2.3675. eprint: https://doi.org/10.2514/2.3675. URL: https://doi.org/10.2514/2.3675.

[41] Robert N. Quammen and Paul F. Rottmann. "Quantification of Directionally Dependent Mechanical Properties and Damage Tolerance of FiberForm". In: *AIAA SCITECH 2023 Forum*. 2023. DOI: 10.2514/6.2023-2597. eprint: https://arc.aiaa.org/doi/pdf/10.2514/6.2023-2597. URL: https://arc.aiaa.org/doi/abs/10.2514/6.2023-2597.

[42] Parul Agrawal and Jose F. Chavez-Garcia. "Fracture in Phenolic Impregnated Carbon Ablator". In: *Journal of Spacecraft and Rockets* 50 (2011), pp. 735–741.

[43] Henry Philibert Gaspard Darcy. "Appendice - Note D: détermination des lois d'écoulement de l'eau à travers le sable". In: *Les fontaines publiques de la ville de Dijon: exposition et application des principes à suivre et des formules à employer dans les questions de distribution d'eau*. Paris: Victor Dalmont, 1856, pp. 590–594.

[44] Alexandre Martin and Iain D. Boyd. "Non-Darcian Behavior of Pyrolysis Gas in a Thermal Protection System". In: *Journal of Thermophysics and Heat Transfer* 24.1 (2010), pp. 60–68. DOI: 10.2514/1.44103. eprint: https://doi.org/10.2514/1.44103. URL: https://doi.org/10.2514/1.44103.

[45] R. A Rindal and C. B Moyer. *An analysis of the coupled chemically reacting boundary layer and charring ablator. Part 2 - Finite difference solution for the in-depth response of charring materials considering surface chemical and energy balances*. eng. Tech. rep. Aerotherm, Mar. 1967.

[46] M. R. Wool and C. B. Moyer. *Aerotherm Charring Material Thermal Response and Ablation Program, Version 3. Volume I - Program Description and Sample Problems*. Mountain View, CA: Aerotherm Corp., Apr. 1970. URL: https://apps.dtic.mil/docs/citations/AD0875062.

[47] H. Goldstein. *Kinetics of Nylon and Phenolic Pyrolysis*. Tech. rep. Lockheed Missiles and Space Co, Oct. 1965, p. 50.

[48] Y.-K. Chen and Frank S. Milos. "Ablation and Thermal Response Program for Spacecraft Heatshield Analysis". In: *Journal of Spacecraft and Rockets* 36.3 (1999), pp. 475–483. DOI: 10.2514/2.3469. eprint: https://doi.org/10.2514/2.3469. URL: https://doi.org/10.2514/2.3469.

[49] Y.-K. Chen and F. S. Milos. "Two-Dimensional Implicit Thermal Response and Ablation Program for Charring Materials". In: *Journal of Spacecraft and Rockets* 38.4 (2001), pp. 473–481. DOI: 10.2514/2.3724. eprint: https://doi.org/10.2514/2.3724. URL: https://doi.org/10.2514/2.3724.

[50] Yih-Kanq Chen and Frank Milos. "Three-Dimensional Ablation and Thermal Response Simulation System". In: *38th AIAA Thermophysics Conference*. DOI: 10.2514/6.2005-5064. eprint: https://arc.aiaa.org/doi/pdf/10.2514/6.2005-5064. URL: https://arc.aiaa.org/doi/abs/10.2514/6.2005-5064.

[51] B F Blackwell. "Numerical prediction of 1-D ablation using a finite control volume procedure with exponential differencing". In: (Apr. 1987). URL: https://www.osti.gov/biblio/6917717.

[52] B. F. Blackwell and R. E. Hogan. "One-dimensional ablation using Landau transformation and finite control volume procedure". In: *Journal of Thermophysics and Heat Transfer* 8.2 (1994), pp. 282–287. DOI: 10.2514/3.535. eprint: https://doi.org/10.2514/3.535. URL: https://doi.org/10.2514/3.535.

[53] R. E. Hogan, B. F. Blackwell, and R. J. Cochran. "Application of moving grid control volume finite element method to ablation problems". In: *Journal of Thermophysics and Heat Transfer* 10.2 (1996), pp. 312–319. DOI: 10.2514/3.789. eprint: https://doi.org/10.2514/3.789. URL: https://doi.org/10.2514/3.789.

[54] Jean Lachaud et al. "A Short Review of Ablative-Material Response Models and Simulation Tools". In: *7th European Symposium on Aerothermodynamics*. Aug. 2011, p. 8.

[55] Mark E. Ewing, Travis S. Laker, and David T. Walker. "Numerical Modeling of Ablation Heat Transfer". In: *Journal of Thermophysics and Heat Transfer* 27.4 (2013), pp. 615–632. DOI: 10.2514/1.T4164. eprint: https://doi.org/10.2514/1.T4164. URL: https://doi.org/10.2514/1.T4164.

[56] Abhishek S. Bhesania, Rakesh Kumar, and Vaibhav K. Arghode. "Ablative Thermal Response for Two-Dimensional Axisymmetric Problems". In: *Journal of Thermophysics and Heat Transfer* 36.2 (2022), pp. 377–388. DOI: 10.2514/1.T6364. eprint: https://doi.org/10.2514/1.T6364. URL: https://doi.org/10.2514/1.T6364.

[57] Joseph C. Schulz et al. "Development of a three-dimensional, unstructured material response design tool". In: *55th AIAA Aerospace Sciences Meeting*. 2017, pp. 1–18. DOI: 10.2514/6.2017-0667. eprint: https://arc.aiaa.org/doi/pdf/10.2514/6.2017-0667. URL: https://arc.aiaa.org/doi/abs/10.2514/6.2017-0667.

[58] Jean Lachaud and Nagi N. Mansour. "Porous-Material Analysis Toolbox Based on OpenFOAM and Applications". In: *Journal of Thermophysics and Heat Transfer* 28.2 (2014), pp. 191–202. DOI: 10.2514/1.T4262. eprint: https://doi.org/10.2514/1.T4262. URL: https://doi.org/10.2514/1.T4262.

[59] Robert M. Chiodi et al. "CHyPS: A High-Order Material Response Solver for Ablative Thermal Protection Systems". In: *AIAA SCITECH 2022 Forum*. Jan. 2022, pp. 1–15. DOI: 10.2514/6.2022-1501. eprint: https://arc.aiaa.org/doi/pdf/10.2514/6.2022-1501. URL: https://arc.aiaa.org/doi/abs/10.2514/6.2022-1501.

[60] Yeqing Wang, Timothy K. Risch, and Joseph H. Koo. "Assessment of a one-dimensional finite element charring ablation material response model for phenolic-impregnated carbon ablator". In: *Aerospace Science and Technology* 91 (2019), pp. 301–309. ISSN: 1270-9638. DOI: https://doi.org/10.1016/j.ast.2019.05.039. URL: https://www.sciencedirect.com/science/article/pii/S1270963819305486.

[61] Jean Lachaud et al. *Properties of the Theoretical Ablative Composite for Open Testing (TACOT)*. 2018. URL: http://jeanlachaud.com/research/TACOT_3.0.xls.

[62] Timothy K. Risch. "Verification of a Finite-Element Model for Pyrolyzing Ablative Materials". In: *47th AIAA Thermophysics Conference*. 2017, pp. 1–35. DOI: 10.2514/6.2017-3354. eprint: https://arc.aiaa.org/doi/pdf/10.2514/6.2017-3354. URL: https://arc.aiaa.org/doi/abs/10.2514/6.2017-3354.

[63] Adam J. Amar et al. "Overview of the CHarring Ablator Response (CHAR) Code". In: *46th AIAA Thermophysics Conference*. 2016, pp. 1–37. DOI: 10.2514/6.2016-3385. eprint: https://arc.aiaa.org/doi/pdf/10.2514/6.2016-3385. URL: https://arc.aiaa.org/doi/abs/10.2514/6.2016-3385.

[64] Jean Lachaud et al. *Test Case Series 1*. Mar. 2011. URL: https://uknowledge.uky.edu/ablation_code/4.

[65] Jean Lachaud, Tom van Eekelen, and Ioana Cozmuta. *Test Case Series 2*. Feb. 2012. URL: https://uknowledge.uky.edu/ablation_code/4.

[66] Jean Lachaud et al. *Test Case Series 3*. Feb. 2014. URL: https://uknowledge.uky.edu/ablation_code/4.

[67] F. S. Milos and Y.-K. Chen. "Ablation and Thermal Response Property Model Validation for Phenolic Impregnated Carbon Ablator". In: *Journal of Spacecraft and Rockets* 47.5 (2010), pp. 786–805. DOI: 10.2514/1.42949. eprint: https://doi.org/10.2514/1.42949. URL: https://doi.org/10.2514/1.42949.

[68] Stewart Victor McDougall. "Early Response of Ablative Materials to Arcjet Testing". PhD thesis. University of Texas at Austin, May 2022.

[69] Stewart V. McDougall, Aditya Vinod, and Fabrizio Bisetti. "Early Response of Ablative Materials to Arcjet Testing". In: *AIAA SCITECH 2023 Forum*. 2023, pp. 1–22. DOI: 10.2514/6.2023-1914. eprint: https://arc.aiaa.org/doi/pdf/10.2514/6.2023-1914. URL: https://arc.aiaa.org/doi/abs/10.2514/6.2023-1914.

[70] Rui Fu et al. "Thermal Expansion for Charring Ablative Materials". In: *Journal of Thermophysics and Heat Transfer* 34.1 (2020), pp. 57–65. DOI: 10.2514/1.T5718. eprint: https://doi.org/10.2514/1.T5718. URL: https://doi.org/10.2514/1.T5718.

[71] Rui Fu et al. "Thermomechanical Coupling for Charring Ablators". In: *Journal of Thermophysics and Heat Transfer* 32.2 (2018), pp. 369–379. DOI: 10.2514/1.T5194. eprint: https://doi.org/10.2514/1.T5194. URL: https://doi.org/10.2514/1.T5194.

[72] Rui Fu et al. "Two-way strongly coupled thermo-mechanical solver for ablation problems". In: *55th AIAA Aerospace Sciences Meeting*. Jan. 2017. DOI: 10.2514/6.2017-0439. eprint: https://arc.aiaa.org/doi/pdf/10.2514/6.2017-0439. URL: https://arc.aiaa.org/doi/abs/10.2514/6.2017-0439.

[73] Rui Fu et al. "Crack Modeling in Charring Ablation Materials". In: *AIAA SCITECH 2021 Forum*. 2021, pp. 1–15. DOI: 10.2514/6.2021-1050. URL: https://arc.aiaa.org/doi/abs/10.2514/6.2021-1050.

[74] Aleksander L. Zibitsker et al. "Development and Verification of a Mesh Deformation Scheme for a Three Dimensional Ablative Material Solver". In: *AIAA SCITECH 2022 Forum*. Dec. 2022, pp. 1–15. DOI: 10.2514/6.2022-1285. eprint: https://arc.aiaa.org/doi/pdf/10.2514/6.2022-1285. URL: https://arc.aiaa.org/doi/abs/10.2514/6.2022-1285.

[75] Justin Droba. "Tangle-free Finite Element Mesh Motion for Ablation Problems". In: *46th AIAA Thermophysics Conference*. 2016, pp. 1–64. DOI: 10.2514/6.2016-3386. eprint: https://arc.aiaa.org/doi/pdf/10.2514/6.2016-3386. URL: https://arc.aiaa.org/doi/abs/10.2514/6.2016-3386.

[76] John Dec. "Three dimensional finite element ablative thermal response analysis applied to heatshield penetration design". PhD thesis. Georgia Institute of Technology, Jan. 2010.

[77] L. Noels and R. Radovitzky. "A general discontinuous Galerkin method for finite hyperelasticity. Formulation and numerical applications". In: *International Journal for Numerical Methods in Engineering* 68.1 (2006), pp. 64–97. DOI: 10.1002/nme.1699.

[78] L. Noels and R. Radovitzky. "An explicit discontinuous Galerkin method for nonlinear solid dynamics. Formulation, parallel implementation and scalability properties." In: *International Journal for Numerical Methods in Engineering* 74.9 (2007), pp. 1393–1420. DOI: 10.1002/nme.2213.

[79] R. Radovitzky et al. "A scalable 3D fracture and fragmentation algorithm based on a hybrid, discontinuous Galerkin, Cohesive Element Method". In: *Computer Methods in Applied Mechanics and Engineering* 200 (2011), pp. 326–344. DOI: 10.1016/j.cma.2010.08.014.

[80] L. Anand and S. Govindjee. *Continuum Mechanics of Solids*. Oxford Graduate Texts. Oxford University Press, 2020. ISBN: 9780198864721. URL: https://books.google.com/books?id=w4RuzQEACAAJ.

[81] M. E. Gurtin, E. Fried, and L. Anand. *The Mechanics and Thermodynamics of Continua*. Cambridge University Press, 2010.

[82] Clifford Truesdell and Walter Noll. *The Non-Linear Field Theories of Mechanics*. Springer, 1965.

[83] Bernard D. Coleman and W Noll. "On the thermostatics of continuous media". In: *Archive for Rational Mechanics and Analysis* 4.1 (1959). DOI: 10.1007/BF00281381. URL: https://doi.org/10.1007/BF00281381.

[84] Lutz Klinkenberg. "The Permeability Of Porous Media To Liquids And Gases". In: *Drilling and Production Practice* (1941), pp. 200–213. URL: https://api.semanticscholar.org/CorpusID:54042399.

[85] Carl B. Moyer and Roald A. Rindal. *An analysis of the coupled chemically reacting boundary layer and charring ablator. Part 2 - Finite difference solution for the in-depth response of charring materials considering surface chemical and energy balances*. Tech. rep. NASA, 1968.

[86] The $\sum$MIT Development Group. *$\sum$MIT, A scalable computational framework for large-scale simulation of complex mechanical response of materials*. 2021. URL: http://summit.mit.edu.

[87] Satish Balay et al. *PETSc Users Manual*. Tech. rep. ANL-95/11 - Revision 3.1. Argonne National Laboratory, 2010.

[88] L. Noels and R. Radovitzky. "Alternative approaches for the derivation of discontinuous Galerkin methods for nonlinear mechanics". In: *Journal of Applied Mechanics* 74 (2007), pp. 1031–1045. DOI: 10.1115/1.2712228. URL: file:///tmp/publications/journal/jam-06-1232.pdf.

[89] J. F. Molinari et al. "Finite-element modeling of dry sliding wear in metals". In: *Engineering Computations* 18 (2001), pp. 592–609. DOI: http://dx.doi.org/10.1108/00368790110407257. URL: file:///home/rapa/publications/archive/journal/ec-2001.pdf.

[90] Justin M. Cooper et al. "Implementation and Verification of a Surface Recession Module in a Finite Volume Ablation Solver". In: *2018 Joint Thermophysics and Heat Transfer Conference*. 2018, pp. 1–18. DOI: 10.2514/6.2018-3272. eprint: https://arc.aiaa.org/doi/pdf/10.2514/6.2018-3272. URL: https://arc.aiaa.org/doi/abs/10.2514/6.2018-3272.

[91] Olivia M. Schroeder et al. "A coupled ablation approach using Icarus and US3D". In: *AIAA SCITECH 2021 Forum*. 2021, pp. 1–14. DOI: 10.2514/6.2021-0924. eprint: https://arc.aiaa.org/doi/pdf/10.2514/6.2021-0924. URL: https://arc.aiaa.org/doi/abs/10.2514/6.2021-0924.

[92] Mark S. Shephard and Marcel K. Georges. "Automatic three-dimensional mesh generation by the finite octree technique". In: *International Journal for Numerical Methods in Engineering* 32.4 (1991), pp. 709–749. DOI: https://doi.org/10.1002/nme.1620320406. eprint: https://onlinelibrary.wiley.com/doi/pdf/10.1002/nme.1620320406. URL: https://onlinelibrary.wiley.com/doi/abs/10.1002/nme.1620320406.

[93] Lori Freitag, Mark Jones, and Paul Plassmann. "A Parallel Algorithm for Mesh Smoothing". In: *SIAM Journal on Scientific Computing* 20.6 (1999), pp. 2023–2040. DOI: 10.1137/S1064827597323208. eprint: https://doi.org/10.1137/S1064827597323208. URL: https://doi.org/10.1137/S1064827597323208.

[94] J.M. Escobar et al. "Simultaneous untangling and smoothing of tetrahedral meshes". In: *Computer Methods in Applied Mechanics and Engineering* 192.25 (2003), pp. 2775–2787. ISSN: 0045-7825. DOI: https://doi.org/10.1016/S0045-7825(03)00299-8. URL: https://www.sciencedirect.com/science/article/pii/S0045782503002998.

[95] D. Lynch and K. O'Neill. "Elastic Grid Deformation for Moving Boundary Problems in Two Space Dimensions". In: *Finite Elements in Water Resources*. June 1980, 2:7.111–7.120.

[96] P. Underwood. "Dynamic Relaxation". In: *Computational Methods for Transient Analysis* (1983), pp. 245–265. URL: file:///tmp/literature/1983-underwood.pdf.

[97] M. Papadrakakis. "A method for the automatic evaluation of the dynamic relaxation parameters". In: *Computer Methods in Applied Mechanics and Engineering* 25.1 (1981), pp. 35–48. DOI: 10.1016/0045-7825(81)90066-9.

[98] Joseph R.H. Otter, Alfred C. Cassell, and Roger E. Hobbs. "Dynamic relaxation". In: *ICE Proceeding* 35.4 (1966), pp. 633–656. DOI: 10.1680/iicep.1966.8604.

[99] Thomas J.R. Hughes. *The finite element method: Linear static and dynamic finite element analysis*. New York: Dover Publications, Inc, 2000.

[100] H. S. Carslaw and J. C. Jaeger. *Conduction of Heat in Solids*. Oxford University Press, 1959.

[101] Klaus-Jürgen Bathe. *Finite Element Procedures*. New Jersey: Prentice Hall, 1996.

[102] *Arc Test of IsoQ Model*. 2014. URL: https://www.nasa.gov/centers/amesthermophysics-facilities/arc-test-of-isoq-model.